Exploring Lithium and Sodium Anti-Perovskite Solid Electrolytes for Energy Storage Applications

Ana Carolina Coutinho Dutra

Chemistry – School of Natural and Environmental Sciences

Newcastle University

This dissertation is submitted for the degree of

Doctor of Philosophy

Newcastle University August 2024

“Search for a necessity. Try to find a problem.

Contribute in a way that is meaningful to you.

Be the turning point towards something better.”

Kobi Yamada

Abstract

In the face of the current climate emergency, solid-state batteries have been attracting significant attention due to a plethora of potential advantages, such as energy density gains and safety enhancements. Solid electrolytes are the heart of this technology, and the success of future implementations relies on the discovery, design, and development of new solid electrolytes. Computational modelling stands as a vital tool to assist future experimental directions and provide key insights that cannot easily be obtained experimentally. In recent years, anti-perovskites have stood out as promising solid electrolyte candidates as they combine high ionic conductivity, stability against lithium metal anodes, and structural versatility. This Thesis uses computational techniques to explore the pertinent defect chemistry, properties, and ionic transport mechanisms in a range of lithium- and sodium-based anti-perovskite materials, providing fundamental information regarding their potential for future solid electrolyte applications. Lattice statics and classical molecular dynamics calculations are used to investigate a range of Li_xOX_y (X = Cl or Br; x = 3–6; y = 1–4) anti-perovskites with zero- to three-dimensional structures. The simulations reveal the strong connection between lithium-ion dynamics and dimensionality in these anti-perovskite materials, where increased lithium-ion diffusion and decreased activation energy can be seen as dimensionality is reduced. Additionally, density functional theory calculations are utilised to explore the bulk and surfaces of a range of M_3OX (M = Li or Na; X = Cl or Br) anti-perovskites. The simulations predict that the formation of any defect type at any site is more energetically favourable in systems containing Na instead of Li, regardless of their halide content. The analysis of the electronic properties reveals that Na-based systems could

potentially present lower electrochemical stabilities. The calculated migration barriers indicate a complex trade-off between maximising atomic polarisability and bottleneck size in the lattice for enhancing ion migration.

Declaration

I hereby declare that except where specific reference is made to the work of others, the contents of this dissertation are original and have not been submitted in whole or in part for consideration for any other degree or qualification in this, or any other University. This dissertation is the result of my own work and includes nothing which is the outcome of work done by others, except where specifically indicated in the text.

Ana Carolina Coutinho Dutra

August 2024

Acknowledgements

Formal Acknowledgements

I would like to deeply thank Newcastle University for the financial support awarded to me through the Newcastle University Overseas Research Scholarship (NUORS) from the School of Natural and Environmental Sciences that made my PhD work possible. I would also like to express my gratitude to my supervisor Dr James Dawson for all your priceless guidance, training, and support throughout the entirety of my PhD programme, for always supporting and encouraging my ideas and plans, and for always being patient and enthusiastic when discussing new methods and results. I would also like to extend my gratitude to Dr James Quirk and Dr Ying Zhou, members of the Dawson Group, for your guidance on density functional theory simulations. I would also like to thank all the members of the Dawson Group, past and present. I am also deeply grateful to Professor Thomas Penfold and Dr Hanno Kossen for all the invaluable guidance and support provided to me as members of my Annual Progression Panel; your advice was very important to my growth as a PhD student. The computational work presented in this Thesis made use of ARCHER2, the United Kingdom's national high-performance computing service, via the UK HPC Materials Chemistry Consortium, and the Rocket High Performance Computing service of Newcastle University.

I am also truly grateful to the Newcastle University Doctoral College for the financial support awarded to me through the travel bursaries I received. I learned and grew so much in the events that I could attend. I am also deeply grateful for all the information and training provided by the workshops that constituted the Postgraduate Research (PGR) Development

Programme developed by the Faculty of Science, Agriculture and Engineering and for all the support and guidance received from the staff of the PGR support and School of Natural and Environmental Sciences (SNES) Operations team and community.

Informal Acknowledgements

I would like to thank my parents, Pérola and Silvio, for simply being the best people I ever met. Your unending support and love given throughout my life has made me strong enough to start, develop and finish this PhD work and I could not be more grateful for the life you have given me. It is the honour of a lifetime to be your daughter.

I would also like to express my sincere gratitude to Ron, for all your support, love, teasing, Superstore sessions, and for making me laugh and dance like you do. Thank you for always listening to my solid-state battery speeches, for helping me train for several presentations, for caring and for always being there for me. You are such a gift and I am so grateful for you.

I am also so deeply grateful to the wonderful friends I was lucky to make during my PhD. Your jokes, chats, lunch invitations, birthday celebrations and overall beautiful and supportive companionship were so important to me. In Newcastle, huge thank you to Clelia for being the best supportive friend I found during my PhD time at Newcastle University; thank you being so thoughtful, kind and fun. Outside Newcastle, millions of thank you to the best group of friends: Palwinder, Xiaoyue, Jaida, Dani, Prashant, and Aisha. I am so grateful for having met you during the CCP5 Summer School; you all have sprinkled my life with so much fun and laughter there and since then. I cannot wait to be able to visit you all, thank you in person, and create lots of new memories together. A big thank you also to my colleagues I shared the office with, especially Julien, Miriam, and Connor; the days we decorated the office for Christmas are some of my favourite PhD memories!

I would also like to thank you, reader, for reading this Thesis! This is the culmination of years of hard work and learning that would not have been possible without all the amazing aforementioned people. Thank you for taking the time to read this work and this section. I hope you enjoy this dive into batteries, anti-perovskites and scientific research.

List of Publications and Presentations

Publications

1. Dutra ACC, Rudman GER, Johnston KE, and Dawson JA, Defect Chemistry and Ion Transport in Low-Dimensional-Networked Li-Rich Anti-Perovskites as Solid Electrolytes for Solid-State Batteries, *Energy Advances*, 2023, **2**, 653–666.
2. Dutra ACC and Dawson JA, Computational Design of Antiperovskite Solid Electrolytes, *Journal of Physical Chemistry C*, 2023, **127**, 18256–18270.
3. Dutra ACC, Quirk JA, Zhou Y, and Dawson JA, Influence of Surfaces on Ion Transport and Stability in Anti-Perovskite Solid Electrolytes at the Atomic Scale, *ACS Materials Letters* (In Revision).
4. Dutra ACC, Goldmann BA, Islam MS, and Dawson JA, Materials Modelling and Machine Learning for Solid-State Battery Electrolytes, *Nature Reviews Materials* (In Preparation).

Oral Presentations

1. Solid State Ionics 2024, London, UK – **June 2024**
2. Faraday Institution Early Career Researcher Conference, Coventry, UK – **March 2024**
3. Royal Society of Chemistry Solid-State Chemistry Group Christmas Meeting, Edinburgh, UK – **December 2023**

4. School of Natural and Environmental Sciences Fest 23 Symposium, Newcastle upon Tyne, UK – **June 2023**
5. Open Science with the Atomic Simulation Environment Workshop, Halton, UK – **April 2023**
6. Faculty of Science, Agriculture and Engineering PGR Conference, Newcastle upon Tyne, UK – **January 2023**

Poster Presentations

1. Faraday Institution Conference, Birmingham, UK – **September 2023**
2. 4th World Conference on Solid Electrolytes for Advanced Applications: Garnets and Competitors, Tromsø, Norway – **September 2023**
3. Oxford Battery Modelling Symposium, Oxford, UK – **March 2023**
4. Data Science Perspectives: Multi Disciplinary PhD Conference, Newcastle upon Tyne, UK – **February 2023**
5. Royal Society of Chemistry RSC Poster Conference, Global Twitter Conference – **February 2023**
6. 41st Royal Society of Chemistry Solid State Chemistry Group Christmas Meeting, Cambridge, UK – **December 2022**
7. International Bunsen Discussion Meeting Solid-state Batteries V, Frankfurt, Germany – **November 2022**
8. Psi-k Conference, Lausanne, Switzerland – **August 2022**
9. CCP5 Summer School, Durham, UK – **July 2022**
10. International Meeting on Lithium Batteries, Sydney, Australia – **June 2022**
11. Royal Society of Chemistry RSC Poster Conference, Global Twitter Conference – **March 2022 (Prize Winner)**
12. Royal Society of Chemistry RSC Batteries Poster Conference, Global Twitter Conference – **December 2021 (Prize Winner)**

13. 40th Royal Society of Chemistry Solid State Chemistry Christmas Meeting, Global Online Meeting – **December 2021**

Table of Contents

List of Figures

List of Tables

Chapter 1 Introduction

1.1 Energy Storage

The establishment of improved energy storage technologies is currently one of the most critical challenges for scientists and governments all around the globe. Due to their limited and diminishing reserves and the damaging impact that their usage has on the climate, the once omnipresent fossil fuels have been subject to intense global disfavour and criticism in recent decades. In this context, their replacement by clean and efficient technologies has been ruled vital for the future of a healthy environment.

Although the entirety of modern society could be considered responsible for the climate emergency, some sectors rise to prominence in terms of their associated greenhouse gases emissions (e.g., transport, energy supply, and industrial sectors). As an example, in the latest official statistics for transport and environment published by the UK's Department for Transport in 2023[1], an analysis of the proportion of domestic greenhouse gases emissions by sector in 2021 (Figure 1.1) shows the dominant contribution for which the transport and energy supply sectors are responsible, with such sectors accounting for a total of 26% and 20% of the emissions, respectively.

As a result, advances in the field of energy storage have become vital within global research, as, by driving the electrification of transport and the efficient large-scale storage of intermittently generated renewable energy, such innovations are key for achieving net-zero emissions.

Considering the necessary shift in the power source for the transport sector, hybrid electric vehicles (HEVs), plug-in hybrid electric vehicles (PHEVs), and electric vehicles (EVs) have been proposed as promising alternatives to fossil fuel-powered means of transport, as the total or, in the case of hybrid technologies, partial replacement of petrol by batteries significantly lowers their emission of greenhouse gases. In the context of phasing out petrol-powered vehicles, the UK government has recently set the target that 80% of new cars and 70% of new vans sold in Great Britain are to be zero emission by 2030, increasing to 100% by 2035[2].

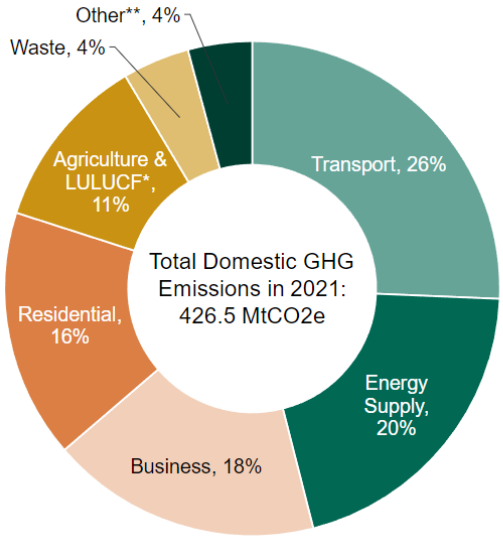

Figure 1.1. Proportion of domestic greenhouse gas (GHG) emissions by sector in 2021 in the UK. Sectors considered include transport, energy supply, business, residential, agriculture & land use, land use change and forestry (LULUCF), waste and others, with the last including emissions from public and industrial processes. Total domestic GHG emissions in 2021 are expressed in million tonnes of carbon dioxide equivalent (MtCO2e).[1]

In recent years, the employment of batteries as a source of power has also been discussed for short-haul aviation, which is significantly relevant for geographies such as the

Nordic countries (e.g., Denmark, Norway, Sweden, Finland, and Iceland), where short-haul flights constitute the great majority of both their domestic and international flights to neighbouring countries. As the replacement of ordinary aviation fuels by batteries would greatly decrease the contribution of the aviation sector to environmental pollution, significant governmental shifts could be seen in this context in recent years. For example, the Norwegian government set the target of having all short-haul flights fully electric by 2040, with the governments of Denmark, Sweden and Finland expecting to have all domestic flights fossil free by 2030, 2045 and 2045, respectively.[3–5]

Although significant advances have been made to accelerate the electrification of transport in recent decades, current commercial battery technologies are still insufficient to provide what future applications will demand, especially regarding their safety profiles, heavy weight, and energy and power densities.[6–10]

Increasing the use of renewable energy sources has been considered paramount to decrease the high levels of environmental pollution associated with the energy supply sector. However, shifting the entire foundation of energy generation methods leads to significant challenges such as, concomitantly, modulating resources over time, balancing electricity generation and demand and, most importantly, establishing a safe and efficient grid integration and large-scale energy storage of energy that is generated intermittently. The use of battery technologies for energy storage in this field has been considering very promising to tackle such challenges due to their high energy conversion capacity and flexibility.[11,12] However, similarly to the current state-of-the-art for batteries designed for electric vehicles, the development of safer, more efficient and lighter batteries is also critical for the success of large-scale storage of intermittently generated energy.

In this context, studies on new high performance battery materials have emerged as powerful tools, as they enable the acquisition of a greater understanding regarding their properties and mechanisms, on which the performance, efficiency and effectiveness of their devices crucially depend.

The next sections of this introductory chapter provide details on a promising next-generation battery technology that has been attracting significant attention from both industry and the scientific community: solid-state batteries (SSBs). The following sections will cover the advantages and challenges pertinent to SSBs, as well as the importance of the discovery of novel solid electrolytes (SEs) for the success of SSB implementations. Moreover, the following sections will focus on the promising anti-perovskite SE material family and the critical role computational modelling plays in advancing the development of novel SEs.

1.2 Li-Ion Batteries

Lithium-ion batteries (LIBs) have taken central stage in the revolution of portable electronics in recent decades and are now omnipresent in modern society. Such large-scale employment is justified by the excellent lifespan and energy density of LIBs, with the latter deriving from lithium being the most electropositive and lightest metal of all.[13]

The development of LIBs started in the 1950s, with fundamental works and remarkable progress having place in the 1970s and 1980s.[14] During these decades, groundbreaking studies were developed by John B. Goodenough, M. Stanley Whittingham, and Akira Yoshino, whose investigations made it possible to create a workable battery. While M. Stanley Whittingham developed the first functional lithium battery in the early 1970s, John B. Goodenough was the responsible for doubling the battery's potential and establishing a more powerful battery in 1980. Five years later, Akira Yoshino's research successfully eliminated pure lithium from the battery, which greatly ameliorated the device's safety profile. This trio of researchers were awarded the Nobel Prize in Chemistry in 2019 for their contributions to the development of the LIB technology.[15–18] A schematic illustration of the functioning of a typical LIB is shown in Figure 1.2.

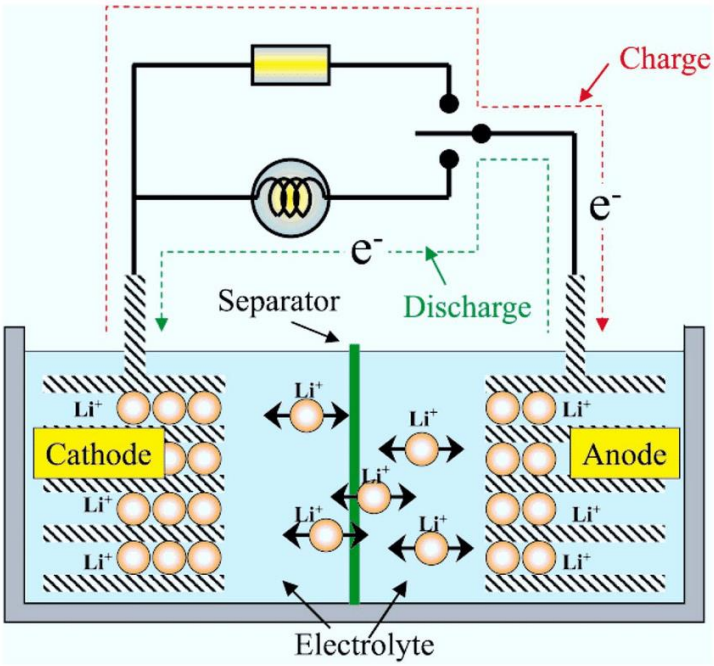

Figure 1.2. Schematic illustration of a typical LIB, including its main components: cathode, anode, separator and electrolyte. Lithium ions are represented by yellow circles and black arrows are used around them to represent the possible directions for their paths during charge (from cathode to anode) and discharge (from anode to cathode). Red and green dashed lines represent the direction of the electrons flow within the circuit during charge and discharge, repectively.[19]

The most pertinent components of the architecture of a common LIB are the anode, cathode, and electrolyte. During the discharging process, lithium cations are released by the anode and diffuse through the electrolyte to the cathode, generating a flow of electrons that power its device. Analogously, during the charging process, lithium ions are released by the cathode and return to the anode via the electrolyte. The importance of the electrolyte for the efficient functioning of the battery cannot be overstated: the electrolyte allows the flow of electrical charge between the cathode and the anode which is the foundation of the battery technology.

Although excellent progress had been made by 1985, the first commercial LIB was not issued until 1991[14], the SONY cell, whose architecture combined a carbon-based anode, a $LiCoO_2$ cathode, and an $LiPF_6$ electrolyte dissolved in organic solvents.[13]

Despite the success this technology had in the last decades and its dominance in modern society, the current state-of-the-art is limited and cannot meet the performance, safety, energy density, and cost requirements that future energy storage devices will demand and improvements in the existing technologies will not be sufficient to satisfy next-generation applications either.[6–10]

Therefore, it is necessary to explore beyond the field of conventional LIB technology to find new battery architectures endowed with the potential to supply the transformative changes that will be required by future leading-edge applications. Concomitantly, due to the ever-increasing nature of society's energy needs, it is also critical to find alternative, cleaner, and cheaper battery chemistries to be used alongside lithium-based next-generation technologies. The employment of new chemistries in less power-hungry applications could be a useful strategy for optimising the usage of higher energy density battery technologies. The following sections provide details on two promising technologies in this field, namely, Na-ion batteries and SSBs.

1.3 Beyond Li-Ion: Na-Ion Batteries

Sodium-ion batteries (SIBs) are a promising alternative battery technology that contrasts to LIBs by its choice of charge carrier, i.e., whereas LIBs use lithium ions, SIBs utilise sodium ions. A schematic representation of a SIB architecture, which is very similar to that of a LIB, is displayed in Figure 1.3.[20]

Similarly to LIBs, SIBs captured attention and were the focus of research studies in the 1970s and 1980s.[21–27] However, explorations of SIB technologies decreased dramatically after the commercial success LIBs obtained in the early 1990s.[11,28,29] In recent decades,

however, interest around SIBs was revived in the battery research community due to growing concerns over the limited nature of lithium resources and the ever-increasing demand for battery-powered applications. Indeed, the global battery demand is predicted to drastically soar and exceed 3,200 GWh by 2030[30,31], which is over three times higher than it was in 2020 (i.e., ~960 GWh).[30,31] Such great demand cannot be satisfied by exclusively using LIBs, with the lithium supply predicted to be insufficient to satisfy the demands for new electric vehicles from 2050 onwards[32] and with the depletion of global lithium reserves expected within a century.[31,33]

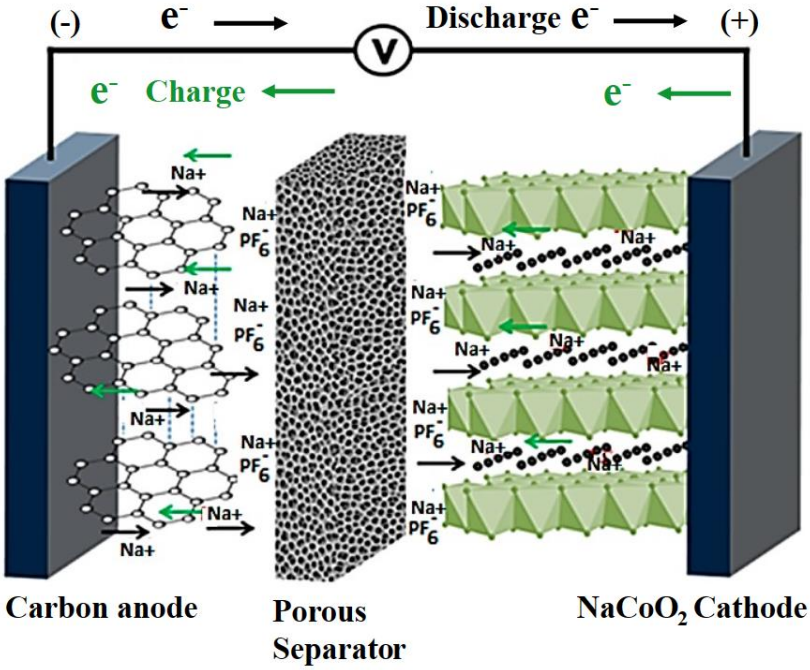

Figure 1.3. Schematic representation of a SIB.[20]

Although recycling technologies can contribute to the sustainability of LIBs and will indeed be crucial to the future of LIBs in the modern world, a recycling rate of 50–100% is predicted to be necessary[34–36] and a plethora of challenges still hinder the establishment of

LIB recycling processes at such large scales, such as significant economic returns, safety concerns, process efficiencies, and environmental impacts.[37,38]

Such a scenario, paired with the consequential continued increase of the cost of lithium, has created an urgency for battery architectures based on abundant metals. Candidates such as sodium, potassium, zinc, calcium, magnesium, and aluminium have attracted significant attention from the battery community, as their use in batteries could secure long-term global energy security.[30]

In this context, SIBs are considered as leading candidates for a promising and efficient alternative battery technology that could be used complementary to LIBs and thus contribute greatly to the future of the electrification of transport and energy storage systems.[30] Although the commercialisation of SIBs is still in its infancy, several companies in different geographies have already started commercialising their production, including Faradion (UK), Natron Energy (USA), HiNa (China), Amperex Technology (China) and Tiamat (France).[30]

The prominence SIB technologies display is a consequence of the important advantages SIBs possess. The most pertinent benefits of SIBs arise from the sodium natural abundance and lower cost compared with lithium. Sodium is over a thousand times more abundant than lithium, with the abundance of sodium and lithium in the crust of the Earth being 23600 ppm and 20 ppm, respectively.[20,30] Such a discrepancy in the sodium and lithium natural abundances not only affects the sustainability associated with the technologies based on these elements but also, naturally, has a great impact on their associated costs.

Out of all the components in a battery architecture, the cathode is widely considered the costliest, with its contribution to the total cost of a LIB being ~25%.[30] As the nature of the cathode material stands as the main contrast between the LIB and SIB technologies and the cathode preparation cost is similar for both LIBs and SIBs, the most drastic cost reduction for SIBs arises indeed from the raw materials themselves. Additionally, aluminium current collectors can be used in SIBs, instead of the ordinary cooper current collectors that are

needed in LIBs, which also contributes to further reduce the costs of SIB technologies.[29] Current projections estimate the cost of SIBs to be around 10–20% lower compared to that of their Li-based analogues.[30] Furthermore, sodium-based metal oxide and polyanion cathode materials can be made from naturally abundant metals such as titanium, manganese, vanadium, and iron and following a process that is cobalt-free[30], which contributes not only to lower the production costs but also removes the necessity of an element (i.e., cobalt) whose mining is highly associated with human-rights issues. Other important benefits associated with SIB technologies are good safety profiles and the fact that the mass-production of SIBs can be conducted in existing LIB manufacturing infrastructures, making them attractive complementary technologies.[30]

It is important to note, however, that although SIBs are considered an important battery technology to be used complementary to LIBs, to this date, they are not viewed as a technology that will be able to completely replace LIBs and fulfil all future global demands. This is mainly due to SIBs presenting lower energy densities and power compared to LIBs, which can be attributed to their contrasts in ionic size and standard potential (e.g., 1.02 Å and approximately 2.71 V vs. Na/Na^+ for sodium and 0.76 Å and 3.04 V vs. Li/Li^+ for lithium, respectively).

The energy densities recorded for SIBs usually range from 100 to 160 $Wh\,kg^{-1}$, being comparable to Li-ion batteries that use $LiFePO_4$ cathodes.[30] The expectation is that SIBs, when fully developed, could replace the use of $LiFePO_4$-based batteries, and be used in applications where the energy density requirements are less demanding than the energy densities provided by powerful LIB technologies but still significantly higher than the energy densities displayed in traditional low power LIBs such as lead-acid, Ni/Cd, and Ni/MH batteries.[20,30] Such applications include short-range and low-speed EVs, energy storage systems supporting solar and wind energy conversion facilities, home grids and power backup in electric utilities.[20,30] Therefore, the SIB market is forecasted to display a rapid growth over the next decade as it will replace a considerable portion of the market currently ruled by LIBs.

The demand for LIBs is expected to rise from 12 GWh in 2023 to 400–500 GWh by 2030, securing more than 20% of the battery market.[30]

There are, however, significant challenges that are yet to be overcome in terms of SIB technologies. Apart from improving SIBs energy densities, the principal disadvantages of SIBs, similarly to LIBs, are their relatively short lifespans (i.e., an average service life of 2–5 years) and environmental and efficiency challenges related to their recycling processes.[30]

Promoting SIB recycling and resource recovery, however, will be significantly more difficult as SIBs generally do not possess high-value metals (e.g., lithium and cobalt) as LIBs, which lowers profitability and imposes a significant extra economic barrier to their recycling.[30] Considering the predicted high demands and large-scale utilisation of SIBs in the next decade, failure in establishing an efficient circular economy for the SIB industry would lead to the accumulation of millions of tonnes of spent SIBs annually in landfills[30], posing critical environmental threats (e.g., releasing of fluorine-based chemicals and leaching of heavy metals intoxicating the local ecosystem, contamination of water sources) and potential fire and explosion risks. Although the raw materials in SIBs are less valuable than those in LIBs, they remain rich in extractable F, Ni, V, Cu, Mn and P and recycling SIBs remains theoretically profitable.[30] Therefore, the design of SIBs that can be efficiently and profitably recycled has become critical for the long-term future of the SIB industry.

In this context, it is clear that the discovery and development of novel materials for SIBs will play a central role in the success of future SIB implementations. For example, research focused on advanced electrode materials with higher specific capacities and voltages will be crucial to obtain SIBs with specific energies reaching 200 Wh kg^{-1} and novel electrolytes will be needed to allow SIBs to display high charge-discharge rates and longer lifespans.[20] Similarly, efforts focused on designing SIBs with facile recyclability will be vital for the future of this industry. Therefore, future research focused on understanding the chemistry of novel SIB materials and architectures is critical for the future of this industry as they will potentially provide solutions to the challenges currently hindering the full potential

of SIBs to heavily contribute to a net-zero economy. The following section provides details on SSBs as another promising technology in the battery field that could largely benefit from the use of sodium-based electrolytes.

1.4 Solid-State Batteries

One next-generation technology that has been capturing significant attention due to its potential to transform the energy storage field is the SSB, which is schematically depicted in Figure 1.4. SSBs have their name derived from their architecture, where a SE is employed to provide fast ionic conduction between the battery electrodes, contrasting with the ensemble found in common batteries, where a liquid electrolyte is used. The great interest SSBs are receiving is a clear recognition of the potential this technology possesses to revolutionise the energy storage field, with SBBs having already been described as the battery technology of the 2030s but the research challenge of the 2020s.[39] The Faraday Institution, the widely renowned UK`s flagship battery research institution, predicts that SSBs will make up 30% of global transportation batteries by 2040.[40]

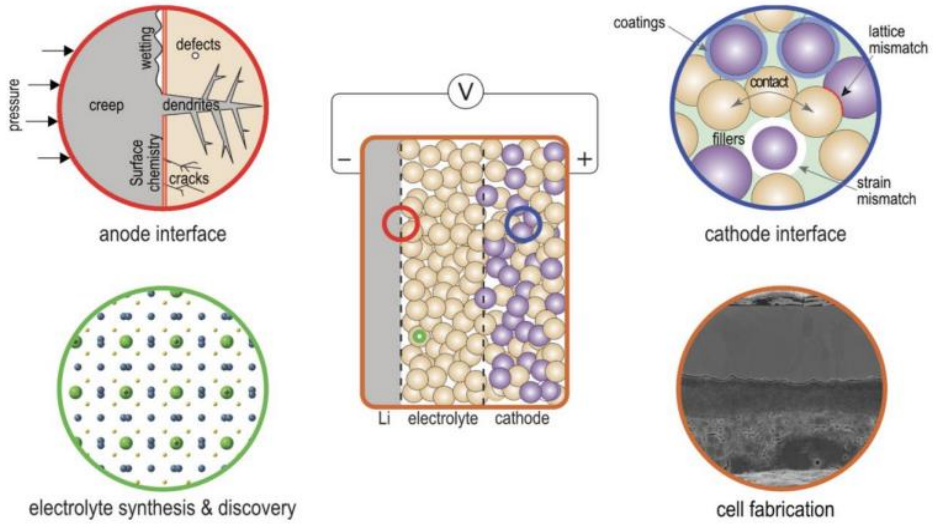

Figure 1.4. Schematic representation of a SSB architecture and a selection of pertinent challenges facing this technology.[41]

Indeed, multiple legacy automakers have set public goals to launch solid-state powered vehicles from 2025 onwards. Volkswagen aims to produce SSBs by 2025 as a result of a $300 million investment in the SSB company QuantumScape.[42] Ford and BMW invested $130 million in the SSB start-up Solid Power and envision debuting the technology in around 2027.[42] Indubitably, Colorado-based Solid Power and Californian QuantumScape are two of the most prominent SSB developers in the current industrial scenario. Mercedes-Benz has the goal to use the technology in passenger vehicles in the second half of the 2020s[43] while Nissan has the target of launching a solid-state powered vehicle by 2028.[44] Honda has the ambition of manufacturing SSBs during the second half of the 2020s.[45]

This significant interest and exciting ambitions are based on a plethora of potential transformative advantages that the usage of SSBs presents compared to traditional batteries, including improved energy density, lifetime, voltage, overall reduced costs, and cycle-life benefits.[7,8,41,46–49] Concomitantly, SSBs have an enhanced safety profile due to the absence of flammable liquid electrolytes and the physical isolation of the electrodes, which avoids Li build-up and possible short-circuiting and explosions.[8,41,46–49] The use of SEs also enables battery operation at a broader temperature range (e.g., –50 to 200 °C or higher) where common liquid electrolytes would freeze, boil or decompose.[8] This latter advantage could be particularly useful for space explorations where batteries are often required to work under extreme conditions. However, numerous challenges are yet to be overcome in order to enable the commercial and large-scale utilisation of SSBs.

For excellent battery performance, it is necessary to have a facile flow of ions across the electrolyte and the complexity and novelty involved in promoting this via an efficient, cost-effective, synthesisable, and stable SE material all whilst maintaining such flow across the battery interfaces with minimum resistance is still a great technological challenge and the reason why the discovery of novel SE materials is critical. Major challenges hindering further advances in SSBs include low ionic conductivities, electrochemical stabilities, dendrite

growth (i.e., branch-like metallic structures that accumulate inside the electrolyte with charge-discharge cycling that can cause fast degradation and short circuits), maintenance of physical contact between solid particles, large-scale SE synthesis, and interfacial resistance, with the latter representing one of the most pivotal obstacles in this context.[8,41,49–51] Concomitantly, although the first recyclable SSB has been reported[52], there are still no established recycling protocols for SSBs. This challenge is, however, not exclusive to SSBs and is also a concern for other battery technologies.

Given the central role that SEs play in SSBs, it is clear that the success of future SSBs implementations relies heavily on the discovery, design, and development of new SE materials that display lower costs, suitable mechanical properties, and high ionic conductivity, stability, synthesisability, scalability, and electrode compatibility. Therefore, the continuous pursuit of understanding the chemistry behind novel SE materials is vital for the future of this field as they will fully reveal the exciting possibilities of these materials.

The following sections provide information on promising SE materials that have risen to prominence in recent years due to their excellent properties. The anti-perovskite SE family, which is the focus of the research documented in this Thesis in Chapters 4 and 5, is covered in detail in Section 1.6.

1.5 Solid Electrolytes

As described in the previous section, due to the critical role SEs play in delivering fast ionic conduction in SSBs, the success of future SSB implementations lies heavily in the discovery, design and development of stable, synthesisable, and efficient SEs.

Consequently, studies focused on the discovery and design of such powerful SEs has soared in recent years. Although promising and competitive materials in terms of conductivity have been identified and developed, including sulphides (e.g., $Li_{10}GeP_2S_{12}$)[53–55], halides (e.g., Li_3InCl_6)[56,57] and oxides (e.g., $Li_7La_3Zr_2O_{12}$)[58,59], the search for a SE material that possesses a

suitable ensemble of qualities (i.e., low costs, suitable mechanical properties, high ionic conductivity, stability, synthesisability, scalability, and electrode compatibility) that could power the large-scale use of SSBs is still ongoing. However, among the promising candidates being considered, there is a material family that stands out due to the excellent ensemble of properties it presents: Li- and Na-based anti-perovskites.

It was based on the prime advantages Li- and Na-based anti-perovskites can potentially bring to SSBs that this material family was chosen as the core of this research. The following section provides details about this material family, including pertinent research results and trends, which served as the foundation and motivation for the research carried out here, as documented in Chapters 4 and 5.

1.6 Anti-Perovskites

Anti-perovskites have their name derived from their structural analogues the perovskite material family, which has been widely investigated for their applications in a vast range of technologies and applications. Perovskites have the typical formula of ABX_3, with cations occupying the A and B sites and an anion populating the X site. Anti-perovskites, conversely, present an inverted lattice to those of perovskites, with the A and B sites being populated by anions while a cation is present on the X site.

In recent years, anti-perovskites, with a typical formula of Li_3OX (X = Cl, Br, I, or a mixture of halides, space group $Pm\bar{3}m$), have become a promising SE family under consideration for SE applications. In this structure, as illustrated in Fig 1.5, the O^{2-} anion (B site) is octahedrally coordinated to six X-site cations and the halide anions at the A-site halide are cuboctahedrally coordinated to twelve nearest-neighbour cations.[7] Structurally, a 3D network for the cation is formed as the cations on the vertices are shared by neighbouring OX_6 sets, establishing octahedra that will form a cubic (sub)lattice that is the foundation of the network.[60] The connectivity between these octahedra enables the hopping of the cations,

which is a process that has been linked to the high ionic conductivities that anti-perovskites display.

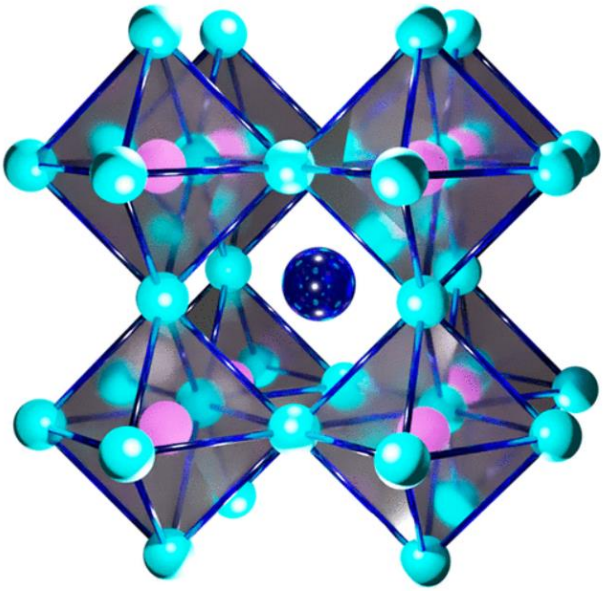

Figure 1.5. Schematic representation of the cubic structure ($Pm\bar{3}m$) of an anti-perovskite with the general formula M_3OX (where M is a cation and X is a halide). The A and B sites (dark blue and pink, respectively) are occupied by anions and a cation occupies the X site (light blue). The B site is octahedrally coordinated to six X-site cations and the A-site anions are cuboctahedrally coordinated to 12 nearest-neighbour cations.[61]

Beyond their reported high room-temperature ionic conductivity (>10^{-3} S cm^{-1}), anti-perovskites are endowed with other excellent features such as structural versatility, wide electrochemical windows, low cost, and stability against Li metal.[7,62–65] This is an ensemble of advantages rarely seen concomitantly in other SE candidates and justifies the outstanding reputation anti-perovskites have gained for SE applications. Additionally, anti-perovskites

possess a remarkably flexible crystal structure that enables easy structural manipulation and the consequent straightforward tailoring of their performance, properties, and ion transport mechanisms, providing substantial chemical versatility and diversity.[66–70]

The chemical and structural diversity provided by anti-perovskites can lead to promising SE candidates that have chemistries beyond the traditional Li_3OX (X = Cl, Br, I or a mixture of halides) anti-perovskites. Interesting candidates that have attracted considerable attention in recent years include Na-, K-, Mg- and Ca-based systems, anti-perovskite systems containing cluster ions (e.g., BH_4^-, BF_4^-, NO_2^-) and low-dimensional-networked (low-DN) anti-perovskites.[61] In this Thesis, Chapter 4 focuses on the study of the defect chemistry and ionic transport mechanisms in low-DN anti-perovskite systems, while Chapter 5 details the analyses of selected Na-based anti-perovskites compared to their Li-based counterparts.

In this context, computational techniques have proved to be excellent tools for the discovery of novel anti-perovskite SE candidates and for the assessment of their features and potential.[7,61,66,69] Chapter 2 provides details of recent findings and progress related to the computational design of anti-perovskite SEs and Chapter 3 introduces a more detailed discussion of the computational modelling methods used in the projects that constitute this Thesis.

Nevertheless, despite the progress shown in studies focused on anti-perovskite materials as SEs, there are still significant obstacles hindering the large-scale application of anti-perovskite materials as SEs, including their strong hygroscopic nature and misconceptions around their synthesisability and stability.[7,61] Furthermore, mirroring the stage of most SE candidates, there are still fundamental challenges inherent to SSBs that remain unsolved, including interfacial resistance, dendrite growth, large-scale synthesis, and electrochemical stability.[7,8,61]

Due to the impact ionic diffusion has on the performance of SEs, understanding the underlying working mechanisms pertinent to ionic migration is key when considering novel

SE materials. Therefore, it is unsurprising that there is a heightened interest in research focused on promoting this understanding as well as on revealing the factors that can impact such ionic diffusion mechanisms (e.g., composition and doping strategies).

In the context of anti-perovskites, mechanistic studies of ion transport represent a particularly interesting topic of discussion. Although the pivotal role that structural defects have in facilitating the ionic transport across anti-perovskite materials is well established, in recent years, many fundamental studies have reported sometimes conflicting theoretical predictions regarding the ionic transport mechanisms at play, especially regarding whether the dominating mechanism is mediated by interstitial or vacancy-based defects.[7,61] In Chapter 2, we provide more details regarding these conflicting predictions.

Such uncertainty regarding the pertinent ionic transport mechanisms present in anti-perovskite systems is even stronger when related to systems whose structures and chemistries differ from the typical formulae traditionally associated with SE research, such as anti-perovskite materials containing mobile Na, K, Mg, or Ca ions and low-DN anti-perovskites. For low-DN anti-perovskites, for example, the ion transport mechanisms and defect chemistry are yet to be fully explored and understood.

Therefore, despite the considerable body of work existent focused on anti-perovskite materials, the features, potential and many of the elementary processes that explain their behaviour are still not fully understood. This means that there is a need to acquire more knowledge regarding the chemistry of the candidates belonging to this promising SE material family, especially those with non-traditional chemistries and structures, to investigate all the possibilities this easily tuneable materials could represent.

It was based on this scenario that low-DN anti-perovskites and Na-based 3DN anti-perovskites were chosen as the core of this doctorate programme. Considering the great power computational techniques have in terms of investigating ionic diffusion, structural disorder and ion transport behaviour in SEs and the excellent recent advances made in the anti-

perovskite field by computational works, an ensemble of computational techniques was chosen to compose this doctorate programme. Chapter 2 provides an overview of pertinent recent findings regarding the computational design of anti-perovskite SEs and Chapter 3 introduces a more detailed discussion of the computational modelling methods used in this research.

1.7 Thesis Outline

Computational models are used to elucidate the chemistry behind Li- and Na-based anti-perovskite systems in the context of their use as SEs. Chapter 4 focuses on investigating the defect chemistry, stability, and ionic transport in a range of bulk Li_xOX_{x-2} (X = Cl or Br; x = 3–6) anti-perovskites with zero- to three-DN structures using classical atomistic simulations. Chapter 5 explores the differences in features and ionic migration in the bulk and at the surfaces of a range of selected 3DN Li- and Na- based anti-perovskite systems with formulae M_3OX (M = Li or Na; X = Cl or Br) using density functional theory (DFT) simulations. The results reported here are summarised in Chapter 6, along with a consideration of possible future work. Such results strengthen our current understanding of the chemistry of anti-perovskites, contributing to the guidance of future experimental decisions and comprehending their potential as SEs in the urgent quest of finding novel materials that could make energy storage safer, more efficient and, most importantly, more sustainable.

Chapter 2 Computational Design of Anti-Perovskite Solid Electrolytes

2.1 Introduction

Computational modelling is a vital tool for tackling the critical challenges associated with solid electrolyte (SE) discovery and design, by, for example, aiding in predicting novel promising SE compositions or by providing a deeper understanding of a candidate's underlying working mechanisms. In this scenario, computational modelling can be a great asset to be used alongside experimental efforts, as computational simulations can not only assist and guide future experimental directions but also provide key insights that cannot be realised experimentally, resulting in more successful synthesis attempts with improved time and resource efficiency.

Atomistic simulations based on density functional theory (DFT), machine learning (ML), ab initio molecular dynamics (AIMD), high-throughput approaches and force field-based molecular dynamics (MD) have been critical in identifying and screening promising solid electrolyte compositions and in understanding and tailoring a wide variety of important phenomena and properties, including ionic and electronic conductivity, diffusion mechanisms, stability, defects and doping, and interfacial resistance and compatibility.

This Chapter highlights the latest progress in the computational design of anti-perovskite SEs, covering crucial topics for their further development and large-scale implementation, including high-throughput screening for new compositions, synthesisability, doping, ion transport mechanisms, grain boundaries, and electrolyte-electrode interfaces.

Furthermore, this Chapter closes with a discussion focused on the remaining challenges in this field, including an outlook in terms of possible future advances and applications for this ever-evolving field.

2.2 Discovery, Screening, and Synthesisability

Discovery and compositional screening studies of anti-perovskites have provided critical information in terms of how different compositions and chemistries can impact the potential performance of these materials as SEs. Such investigations are particularly interesting when comparing Li-based systems to different chemistries, such as Na-based anti-perovskites.

One example is the computational study conducted by Dawson *et al.*[71] concerning a wide range of $Li_{3-x}Na_xOCl_{1-y}Br_y$ compositions, which showed the impact that halide-ion mixing has on the conductivity shown by such systems, the low conductivities and high activation energies for mixed Li/Na systems, and the more prominent Li-ion conductivity when compared to Na-ion conductivity. Li- and Na-based anti-perovskites with Ruddlesden–Popper structures have also recently captured significant attention. Interestingly, Yu *et al.*[72] reported in a fully computational study that Li/Na mixing in anti-perovskites with the general formulas of $Na_{4-c}Li_cAX_4$ (A = O and/or S; X = I and/or Cl) could lead to a promising SE candidate, $Na_3LiS_{0.5}O_{0.5}I_2$, which displayed a very low activation energy of 0.12 eV and a room temperature (RT) ionic conductivity of 6.3 mS cm^{-1}, with both aspects predicted by AIMD calculations, as well as both thermo- and electrochemical compatibility with sodium metal anodes. The most promising candidate based solely on sodium reported by the authors was $Na_4S_{0.5}O_{0.5}I_2$, which possessed a RT ionic conductivity of 0.347 mS cm^{-1} and an activation energy of 0.23 eV, with both aspects being predicted by AIMD calculations. More recently, Jalem *et al.*[73] investigated fully computationally a material space of more than 500 Li-rich anti-perovskites with the n = 1 Ruddlesden–Popper tetragonal structure via DFT, MD, and phonon calculations to find promising SE candidates based on critical features toward

battery applications such as thermal and electrochemical stability, Li-ion transport and surface properties (Figure 2.1). The authors predicted that 167 compounds are thermodynamically (meta)stable and highlighted 20 novel compounds with a DFT decomposition energy below 0.05 eV/atom as well as predicting a low likelihood for lithium dendrite formation in these compounds via slab calculations, illustrating the potential of anti-perovskite SEs with Ruddlesden–Popper structures.

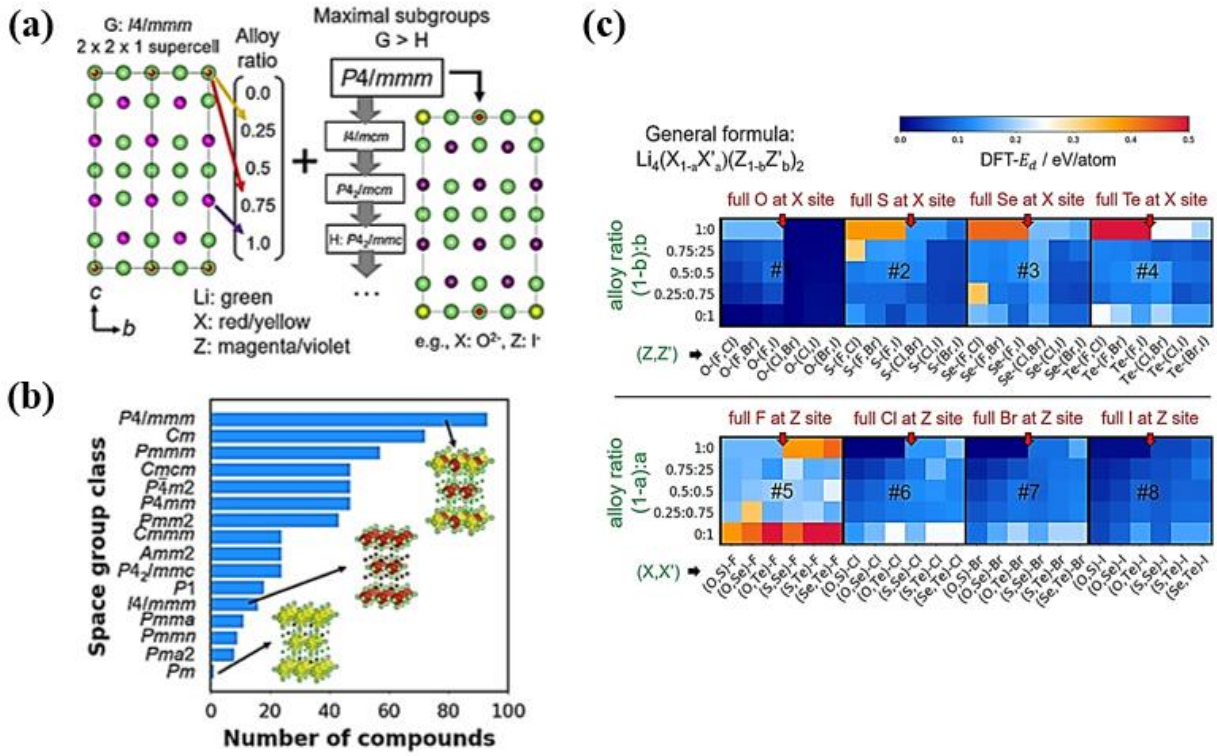

Figure 2.1. (a) Schematic illustration of the generation of tetragonal Ruddlesden–Popper anti-perovskites. (b) Histogram plot of in silico generated anti-perovskites with their space groups from the procedure in (a). (c) Thermodynamic stability map for in silico generated anti-perovskites with one-element full occupancy at one anion site (red), while the other anion site is varied (green). Inset numbers indicate the subplot number (with a #) for each chemical substitution case. The colour map represents the DFT decomposition energy (E_d) values with <0.1 eV/atom set as the phase stability criterion. Vertical axes (red and green) show

substitution ratios corresponding to X/Z combinations described in the horizontal axes. Element combinations (X,X′–Z,Z′) are shown inside parentheses.[73]

Li- and Na-rich anti-perovskites based on cluster ions (e.g., BH_4, AlH_4, BF_4, and BCl_4) have also shown promising results. In a DFT study, Fang and Jena[64] investigated a variety of Li-rich anti-perovskites based on cluster ions (Li_3O^+/Li_3S^+ and BH_4^-/AlH_4^-/BF_4^-), and their results suggested that cluster ions can produce larger band gaps and channel sizes in anti-perovskite structures, providing a larger environment for Li ions to diffuse. Structures including Li_3SBF_4, $Li_3S(BF_4)_{0.5}Cl_{0.5}$, $Li_3O(BH_4)$, and $Li_3O(BH_4)_{0.5}Cl_{0.5}$ were reported as promising SEs with, respectively, RT conductivities of 10^{-2}, 10^{-1}, 10^{-4}, and $>10^{-3}$ S cm^{-1}.[64,74] Na-rich-cluster-based anti-perovskites were also explored by Fang and Jena[75] in a work that reported $Na_3S(BCl_4)$ and $Na_3S(BCl_4)_{0.5}I_{0.5}$ as promising SE candidates, displaying RT ionic conductivities of $>10^{-3}$ S cm^{-1}, low activation energies (<0.2 eV), large bandgaps, and suitable mechanical properties.

More recently, Xu *et al.*[76] used DFT calculations to explore stability, electronic properties, elastic constants, and Na-ion migration in cluster-based anti-perovskites with the formula Na_3SA (A = AlF_4, ClO_4, ICl_4, or IO_4). Their results revealed that cluster substitutions at the A site can lead to larger band gaps and higher ion transport in the selected anti-perovskites when compared to their counterparts that contain halides on their A site. MD simulations suggested that the improved ion transport results from the rotation of cluster ions and the large volume created inside the crystal structure. However, it is noteworthy that cluster substitutions can also lead to lattice distortions that can lower the stability of the material. The authors determined Na_3SAlF_4 to be the best candidate tested, with an activation energy of 0.19 eV, a stable structure, an ionic conductivity of 6.55×10^{-2} S cm^{-1} at RT and a migration barrier of 0.46 eV.

Although the above atomistic studies provide crucial information for the fundamental understanding of anti-perovskite SEs, given the great structural and chemical diversity they

present, high-throughput screening and ML methods are also vital for their timely further development.

The first high-throughput screening that focused on anti-perovskites was conducted by Singh *et al.* in 2018[77], where DFT and phonon calculations were used to evaluate the thermodynamical, mechanical, and dynamical stability of 630 cubic magnetic anti-perovskites. Although this study did not explore anti-perovskites as SEs, it identified 11 novel anti-perovskite compositions, thereby illustrating the potential of this approach. Concurrently, ML has been used for the binary classification of crystal compounds as perovskites or non-perovskites[78], with artificial neural networks successfully used to classify compositions as cubic anti-perovskites and identify those that display octahedral rotation.

More recently, ML has also been used as a powerful tool for synthesisability predictions in anti-perovskites. As seen with the development of many others prediction methods for anti-perovskites, the progress in ML for synthesisability predictions also started with efforts focused primarily on common perovskites.[79–85] Unfortunately, due to their focus on metal oxide perovskites or reliance on the Shannon ionic radii database, many of these models could not successfully be applied in anti-perovskite predictions.[79] However, this scenario changed recently, with Gu *et al.*[79] reporting a general graph neural network model capable of assessing the synthesisability of both common perovskites and anti-perovskites based on structural and thermodynamic data taken from several well-known materials databases (Figure 2.2(a)–(d)). The model used predicted 327 virtual anti-perovskites to be synthesisable, including Na-rich anti-perovskites considered as SEs, namely, Na_3OBr and Na_3OF. The study, however, also stated the importance of considering their findings from ML in the context of thermodynamic metrics to generate more accurate predictions.

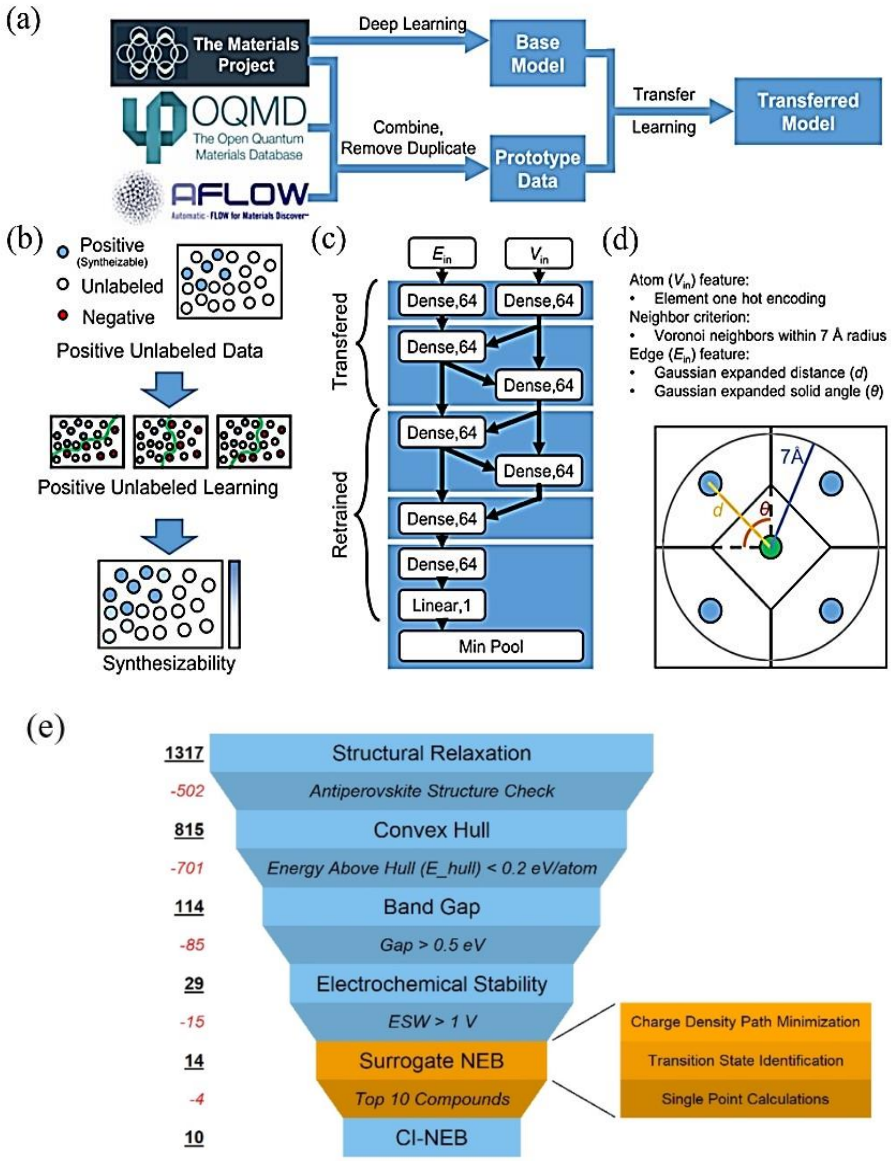

Figure 2.2. (a) Domain-specific transfer learning workflow used to retrieve perovskite structures. The model is first trained with the Materials Project database and then retrained with the perovskite-only data extracted from the three databases. (b) Overview of positive and unlabelled learning procedure. (c) Graph neural network architecture where E_{in} and V_{in} are the atom and edge features, respectively. Dense indicates the linear multiplication followed by the

softplus activation layer, and Linear indicates linear multiplication. The number next to the operation indicates the output feature dimension. Min Pool indicates minimum pooling followed by sigmoid activation. (d) Crystal representation with atoms and edges converted to mathematical representation via featurisation. (e) A visualisation of the steps in the workflow used to screen anti-perovskite candidates, along with the filtering criteria used to lower the total computational cost of the screening. The underscored and italic numbers represent the number of candidates present at each step and the number lost to each criterion, respectively. The inset illustrates the steps of the surrogate nudged elastic band method.[79,86]

ML methods can also be used to accelerate the evaluation of the kinetic properties of anti-perovskites. One of the most critical bottlenecks related to the computational investigation of ion diffusion barriers is the use of time-consuming nudged elastic band (NEB) calculations. As NEB simulations require a supercell approach and several DFT simulations to calculate the energy and forces, the computational cost for NEB-based simulations can be significant, thereby rendering NEB methods unsuitable for large screening studies. To accelerate NEB simulations, different methods have been proposed in recent years, such as the use of crystal symmetries and ML for the identification of transition states.[87,88] In particular, Sjølin *et al.*[86] developed a multitarget multi-fidelity workflow that substitutes the need for expensive NEB simulations, as schematically summarised in Figure 2.2(e). The authors overcame the NEB bottleneck by using a surrogate model capable of identifying the transition-state structure during ionic diffusion and developed the workflow to systematically assess thermodynamic and electrochemical stability and electronic and ionic conductivity. Upon application of the workflow on the chemical space of anti-perovskites, Sjølin *et al.* identified 14 SE candidates, all of which had already been identified by other experimental and computational studies. Although these results show the difficulty in discovering novel anti-perovskite structures, they illustrate how unprecedented advances in the field can be achieved by employing surrogate model-assisted workflows, as conclusions that took traditional studies years to uncover can be rapidly achieved by using such methods.

This work also opens the interesting question of whether similar results would be expected for space groups with distortions (e.g., octahedral tilting) and for low-dimensional-networked (DN) anti-perovskites.[60]

One of the many challenges involved in predicting and confirming a material as a promising SE is that its properties can very often compromise or contradict each another. For example, in the recent study of Gu *et al.*[79] that used graph neural networks to predict the synthesisability of perovskites, eight anti-perovskite systems, namely, Li_3CHg, Li_3BeIr, Li_3CBe, Li_3ClSr, Li_3SPb, Li_3FK, Li_3BeTi, and Li_3PMn, simultaneously showed good synthesisability scores but low thermodynamic stabilities, especially when compared to those computed for Li_3OBr and Li_3OCl. Such results illustrate the importance of establishing a multitargeted search for novel SEs that considers concomitantly multiple pertinent properties (e.g., ionic conductivity, thermodynamic stability, electrochemical stability, and synthesisability) to avoid incomplete analyses that can lead to premature promising status declarations.

In this context, studies that explore the impact different chemical, mechanical, and structural features have on ion mobility, stability, and synthesisability and investigate possible intrinsic correlations between such features are critical for the further development of SE candidates.

Important insights regarding the connections between lattice distortions, stability, and ionic mobility in anti-perovskites were obtained by Kim and Siegel[69] in a work that assessed 24 anti-perovskites with the general formula X_3BA (X = Li or Na; B = O, S or Se; A = F, Cl, Br, or I). The authors introduced lattice distortions (e.g., tilting/rotation of polyhedral building blocks, bond length variations, and symmetry lowering/shifting) via isovalent substitutions and used DFT simulations to calculate the energy barriers for ion migration pathways, assuming both vacancy and interstitial mechanisms. A strong correlation was found between the magnitude of lattice distortions and energy barriers, with larger distortions providing lower energy barriers for ion migration regardless of the preferred migration mechanism. This

work also revealed a correlation between the degree of lattice distortion and thermodynamical stability where higher lattice distortions are accompanied by lower stabilities. These results made evident that promising SE candidates need an appropriate balance between mobility and stability. The authors suggested Na_3SI as a balanced candidate in terms of stability and ionic conductivity. Candidates such as Na_3SeF, Na_3SeI, Li_3SI, and Na_3SF were also highlighted as being worthy of future experimental explorations.

More recently, in an experimental-computational work, Kim *et al.*[89] used DFT calculations alongside the quasi-harmonic approximation to investigate the thermal stability and synthesisability of metastable anti-perovskites with the general formula X_3BA (X = Li, Na, or K; B = O, S, or Se; A = F, Cl, Br, or I). In this study, a linear correlation between the degree of lattice distortion (i.e., the tilting of the alkali metal octahedra and consequent perturbations to bond lengths and angles) and the stabilisation temperature was found, indicating that anti-perovskites endowed with the highest ionic mobility will usually demand the highest synthesis temperatures. This data guided experimental efforts that successfully resulted in the synthesis of Na_3OA (A = Cl, Br, or I) and Li_2OHA (A = Cl or Br) and showed overall good agreement with the computational predictions, indicating that the 0 K decomposition energy of a SE can be a suitable descriptor for assessing the complexity and likelihood of its synthesis.

As a crucial step when designing and assessing new anti-perovskite materials, accurately predicting their synthesisability has proved to be challenging. It has been discussed widely in the literature[7,82,90] how the Goldschmidt tolerance factor, a traditional indicator of stability, is not a suitable descriptor for anti-perovskite materials, especially those containing heavy halides, such as Cl, Br, or I, and cluster ions, such as BH_4, BF_4, or NO_2. One of the reasons for such unsuitability is the use of Shannon radii values, which can potentially contribute to a nonrepresentative description of the ion environment and, consequently, inaccuracies when using the Goldschmidt factor. Attempts to refine the radii for such calculations have been reported[7,82,90] and a modified Goldschmidt tolerance factor formula

recently proposed by Jalem *et al.*[73] proved to be successful as a descriptor for thermodynamic stability and band gap energy for anti-perovskites with the n = 1 Ruddlesden–Popper tetragonal structure.

2.3 Doping, Defects, and Ion Transport Mechanisms

Research into understanding how different doping approaches can impact ionic conduction in SE candidates is crucial for the development of solid state batteries (SSBs). In this context, Squires *et al.*[91] used DFT calculations to investigate the defect chemistry of Li_3OCl and the impact that supervalent and subvalent doping has on its native defect concentrations (e.g., vacancy, interstitial, and anion antisite defects) and ionic conductivity. As shown in Figure 2.3(a),(b), the authors found that lithium and chlorine vacancies were the dominant negatively and positively charged defect species in undoped Li_3OCl, respectively, under Li-poor conditions. Under Li-rich conditions, the dominant disorder types found were the oxygen–chlorine antisite and lithium vacancy, respectively. The identification of this antisite as one of the preferred disorder types shows the importance of investigating beyond Schottky and Frenkel-type defects when analysing the defect chemistry of anti-perovskites. Importantly, lithium vacancies were predicted to be present in concentrations much greater than those of lithium interstitials under all considered synthesis conditions. The study proposed that supervalent doping could be an effective strategy to increase ionic conductivity in the system, especially under Li-poor synthesis conditions, while subvalent doping could have a detrimental effect on the RT ionic conductivity at low-to-moderate doping levels when compared to undoped Li_3OCl.

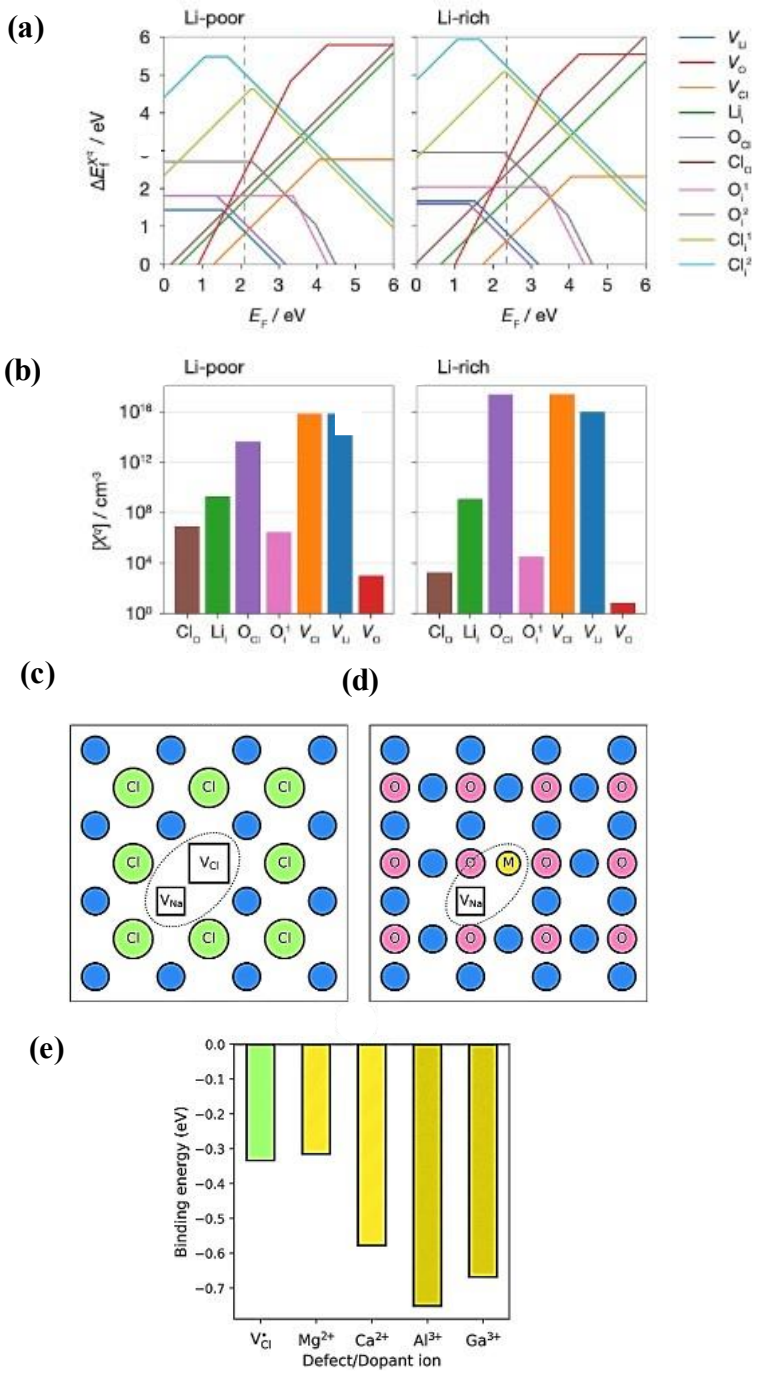

Figure 2.3. (a) Formation energies and (b) concentrations for defects in Li_3OCl under Li-poor and Li-rich synthesis conditions at 360 °C. The dashed line marked on the transition level

diagrams is the position of the self-consistently determined Fermi energy, and defect charge states are given by the gradient. Defect clustering in Na_3OCl: (c) undoped structure with sodium and chloride vacancies; (d) doped structures with a sodium vacancy and a dopant ion; (e) binding energies for defect/dopant clusters.[91,92]

As localised clustering can occur when extrinsic dopants and point defects interact with each other, and this phenomenon can have a detrimental impact on ionic mobility, one of the most pertinent calculations when exploring doping effects is the evaluation of dopant-vacancy binding energies. For example, Clarke *et al.*[93] studied the doping of Li_3OCl with F^- and divalent cations (Mg^{2+}, Ca^{2+}, Sr^{2+}, and Ba^{2+}) via defect and MD simulations and found that while F-doped Li_3OCl displayed high dopant-vacancy binding energies and low conductivity, its Mg-doped analogue displayed high ionic conductivity and low migration barriers with low dopant-vacancy binding energies.

Doping of Na-based anti-perovskites has also captured significant attention. For example, Wan *et al.*[94] used a combination of NEB and AIMD simulations to analyse Mg, Ca, Sr, Ba and Ca doping in Na_3OCl. The authors reported Ca^{2+} to be the most promising dopant tested for this material, as its addition leads to the lowest dopant-vacancy binding energy. More recently, Goldmann *et al.*[92] explored the effects of divalent and trivalent dopants (Mg^{2+}, Ca^{2+}, Sr^{2+}, Ba^{2+}, Al^{3+}, and Ga^{3+}) on the ionic transport and conductivity in Na_3OCl via large-scale atomistic calculations (Figure 2.3(c)–(e)). The authors found that alkali-halide Schottky defects are the dominant disorder in undoped Na_3OCl and revealed Mg^{2+}, Ca^{2+}, Al^{3+}, and Ga^{3+} as the most favourable dopants, with the smallest binding energy and highest conductivity displayed by the Mg-doped system (10^{-5} S cm^{-1} at 500 K). As shown in Figure 2.3(e), higher binding energies were found for Ca^{2+}, Al^{3+}, and Ga^{3+}, indicating a significant level of vacancy/dopant clustering, resulting in reduced ionic conduction compared with that of their Mg-doped analogue.

Due to the importance that effective ion migration has for the performance of SSBs, it is unsurprising that a vast number of studies have also focused on promoting the understanding of the underlying mechanisms involved in ionic diffusion within SEs and uncovering the factors that can impact such mechanisms.

As discussed in Chapter 1, in the context of anti-perovskites, mechanistic studies of ion transport represent a particularly interesting topic of discussion. This interest arises from many fundamental studies with sometimes conflicting theoretical predictions in recent years, especially regarding the dominance of interstitial or vacancy-mediated mechanisms. Emly *et al.* investigated a three-ion hop mechanism that involved Li interstitial dumbbells in Li_3OCl, Li_3OBr, and $Li_3OCl_{0.5}Br_{0.5}$ via DFT simulations.[95] The authors found that such a mechanism leads to a very low Li-ion migration barrier of ~0.17 eV for Li_3OCl and Li_3OBr, indicating a concerted Li-ion motion that is seen in several other solid electrolytes.[93,96–104] However, the same report also found high formation energies for Li interstitials, indicating that the mechanism could not be responsible for the high conductivities observed experimentally.

Mouta *et al.*[105] also attempted to elucidate the dominant ion transport mechanism in Li_3OCl and found a low value of 0.13 eV for interstitial migration based on classical atomistic quasi-static calculations. However, as the concentration of Li vacancies found were six orders of magnitude greater than those for Li interstitials, the authors declared vacancy migration, with an energy barrier of 0.30 eV, to be the pertinent ion transport mechanism in Li_3OCl. Lithium vacancy hopping was also deemed to be the main ionic diffusion mechanism in Li_3OCl by Lu *et al.*[106] in a study that used classical MD and DFT simulations to investigate the defect chemistry and ionic transport of this material based on three types of charge neutral defect pairs (i.e., LiCl and Li_2O Schottky pairs and a Li interstitial with an oxygen–chlorine antisite). The authors found that while all analysed defect pairs have similar formation energies, they all lead to different ionic diffusivities. The LiCl-deficient Li_3OCl displayed the highest ionic conductivity based on the formation of low energy Li transport pathways between the Cl vacancies.

The debate over whether the pertinent ion transport mechanism for anti-perovskites is vacancy hopping or an interstitial mechanism was furthered by a classical atomistic quasi-static study by Mouta *et al.*[98] that suggested that Li interstitials could become dominant in Li-rich anti-perovskites when they are sufficiently Li-halide deficient. In addition, a blended perspective was offered by Stegmaier *et al.*[96], where Li vacancies will be present in Li_3OCl near the cathode and Li interstitials will dominate near the anode–electrolyte interface. Vacancy hopping was found to be the preferred mechanism in a work conducted by Dawson *et al.*[71] that focused on a wide range of anti-perovskites with the general formula $Li_{3-x}Na_xOCl_{1-y}Br_y$ (x = 1–2; y = 0–1). A vacancy-mediated mechanism was also found to be the pertinent mechanism for Na_3OCl by Wan *et al.*[94] in a study that combined NEB and AIMD simulations. However, interstitials were shown to play a significant role in Ruddlesden–Popper anti-perovskites with the general formula X_4OA_2 (X = Li or Na; A = Cl, Br, or I) in a study by Zhao *et al.*[99] that compared vacancy and interstitials mechanisms, with the latter displaying lower migration barriers. In the context of Ruddlesden–Popper systems, using MD simulations, Jalem *et al.*[73] revealed that the characteristic migration mechanism in inverse Ruddlesden–Popper tetragonal anti-perovskites is fast Li-ion diffusion within the O–Li intraslab layer in the ab and ac/bc planes.

More recently, Gao *et al.*[68] successfully combined hydride anions (H^-), endowed with large polarisability, and chalcogenide (Ch_2^-) anions to form a series of anti-perovskites with soft anionic sublattices (M_3HCh (M = Li or Na; Ch = S, Se, or Te)). The NEB-calculated energy barriers for the interstitial dumbbell hopping mechanism in these materials ranged from 0.05 to 0.14 eV (Figure 2.4(a)), values significantly lower than those calculated for vacancy-mediated mechanisms, which ranged from 0.15 to 0.32 eV (Figure 2.4(b)). These low migration barriers indicate a favourable dumbbell migration mechanism.

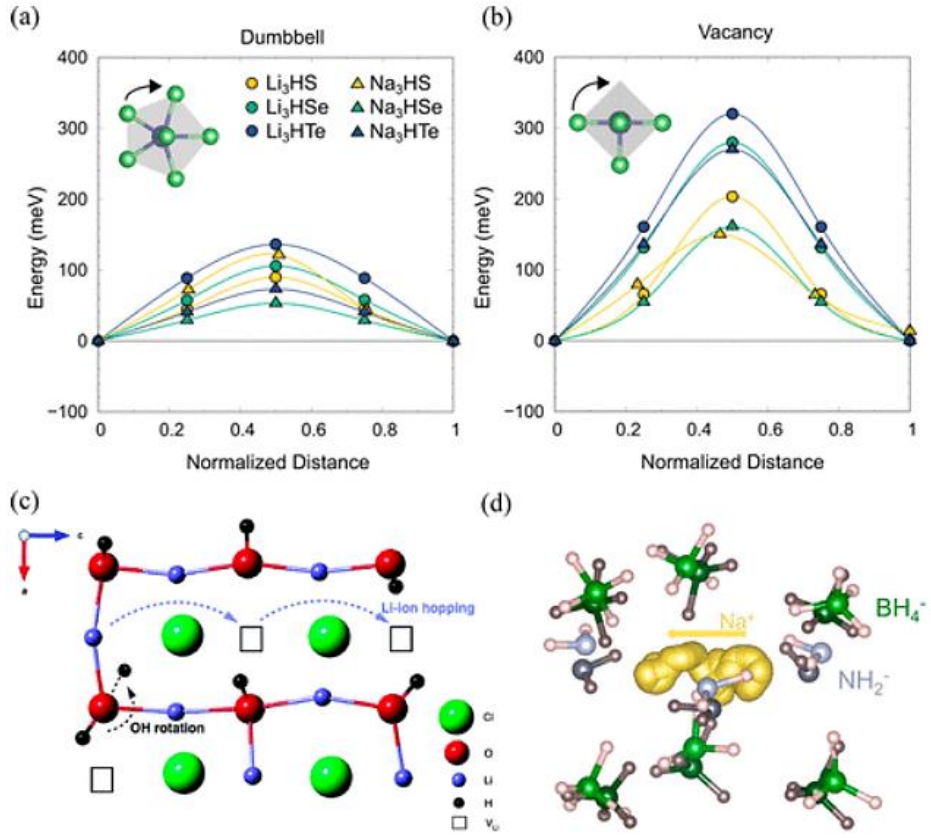

Figure 2.4. Low-barrier migration pathways for (a) vacancy and (b) interstitial dumbbell migration in M_3HCh (M = Li or Na; Ch = S, Se, or Te) anti-perovskites. (c) Calculated Li-ion migration mechanism in Li_2OHCl. (d) Atomic trajectories for a representative Na-ion migration event in $Na_2(NH_2)(BH_4)$ at 363 K. Every frame is shown for the Na ion, while for the neighbouring cluster anions just the initial and final positions are displayed (dark and light, respectively).[68,107,108]

The effect of halide substitution on the ion transport properties of anti-perovskites has also been considered. In a previous experimental–computational study by Ahiavi *et. al* [109], the authors utilised diffraction techniques, impedance spectroscopy, and AIMD simulations to investigate mixed halide compositions with the formulas Na_3OX (X = Cl, Br, I, and/or BH_4),

including $Na_3OCl_{0.5}(BH_4)_{0.5}$, $Na_3OBr_{0.5}(BH_4)_{0.5}$, $Na_3OI_{0.5}(BH_4)_{0.5}$, and $Na_3OCl_{0.33}Br_{0.33}(BH_4)_{0.33}$. The study found a qualitative trend where increasing the halide size concomitantly increases conductivity and decreases the activation energy. This trend illustrates how the halide size impacts the cell volume and, thus, the Na–O distance. Longer Na–O distances lead to a weaker coordination and facilitated Na-ion hopping and, consequently, increased conductivity. Simultaneously, the effect of the halide size on the activation energy can be understood as the polarisability of the halogen controlling the activation energy for conduction via its effect on the lattice softness.[110,111]

Interesting results regarding ionic transport were also obtained for the cluster-ion-based vacancy-rich $Na_2BH_4NH_2$ material, which displayed a high ionic conductivity of 7.56×10^{-4} S cm^{-1} at 90 °C and an activation energy of 0.67 eV in an experimental–theoretical study by Jiang *et al*.[112] The authors used AIMD simulations to explore ionic migration and the role of vacancies in the system and found that Na ions could easily migrate within the bulk of $Na_2BH_4NH_2$ via both interstitial and vacancy migration. Mean-squared displacement plots for this material showed that ionic diffusion was greater in Na vacancy-rich $Na_2BH_4NH_2$ compared to that in Na vacancy-free $Na_3BH_4NH_2$ and $NaBH_4$ at 300 K, illustrating the positive impact vacancies have on ionic transport.

The impact of different structural features, such as polyanion rotation, on ionic migration has also been investigated. Fang *et al*.[64,74] used DFT and AIMD calculations to explore the stability and ionic migration characteristics in superhalogen-based anti-perovskites, such as Li_3OBH_4, Li_3SBF_4, $Li_3OCl_{0.5}(BH_4)_{0.5}$, and $Li_3SCl_{0.5}(BF_4)_{0.5}$. The authors found that the rotation and translation of the superhalogen clusters have a fundamental role in the enhancement of Li-ion migration in the analysed systems, an effect often labelled the "paddlewheel effect". The paddlewheel effect is often reported to be an important factor for improved ionic migration in many anti-perovskites, as well as in other solid electrolytes candidates.[7,100–102,113] Song *et al*. utilised an array of materials characterisation techniques and AIMD simulations to explore the ionic conductivities of $Li_{3-x}OH_xCl$ (x = 0–1) and

Li_2OHBr.[114] Their results found an interesting mechanism for Li-ion transport, where low energy pathways for the formation of Frenkel defects and highly correlated Li-ion jumps were created by the rotation of the OH group. This mechanism results in fast and highly correlated ionic transport and was reported to significantly enhance the ionic conductivity of the analysed systems. Similarly, in a DFT study that investigated the different phases of Li_2OHCl, Howard *et al*.[115] found that the presence of OH groups could affect the ionic motion in this hydrated system.

Dawson *et al*. also investigated the $Li_{3-x}OH_xCl$ system via integrated AIMD and solid-state nuclear magnetic resonance (NMR) studies. As schematically presented in Figure 2.4(c), their results revealed a strong relationship between proton dynamics and long-range Li-ion transport based on Li-ion hopping and the rotation of the OH group, with Li-ion transport being highly correlated with proton concentration and Li-ion vacancy levels.[107] Their atomistic simulations indicated fast Li-ion diffusion but ruled out the possibility of long-range proton diffusion due to the large separation between oxygen ions (∼4 Å). Similar conclusions were found by posterior works by Song *et al*.[116] and Wang *et al*.[117] Such reports indicate that the tailoring of proton content could be a useful strategy for optimising the ionic conductivity of anti-perovskite SEs.

More recently, the first instance of a double paddlewheel effect, where the rotational mobility of both anion groups promotes fast ionic migration, in an anti-perovskite was reported by Tsai *et al*.[108] in an experimental–theoretical study of $Na_{3-x}O_{1-x}(NH_2)_x(BH_4)$ (Figure 2.4(d)). The techniques utilised to confirm the concomitant importance of the rotation of both anion groups included AIMD, electrochemical impedance spectroscopy, powder and synchrotron X-ray diffraction, and NMR and neutron diffraction. The double paddlewheel effect leads to a Na-ion conductivity a factor of 102 times higher at x = 1 compared to the result expected when only a vacancy-mediated mechanism is present. Although the study confirmed that the rotational activity of both anion groups is required to establish high ionic mobility, only the rotation of the amide group is synchronised with Na-ion migration with the

mobility of the borohydride anions displaying an indirect and asymmetric relationship to the Na ions. Such an expansion of the paddlewheel effect concept and further investigation of this in other anti-perovskites could accelerate their future discovery and design.

The use of computational design in probing ion transport mechanisms is particularly important, given that the experimental characterisation of such phenomena can be challenging with significant barriers. These include the limited ability of many characterisation methods to perform in situ monitoring, the need for expensive setups and hardware to carry out in situ measurements and the competitive nature of securing experimental time at national and international facilities to use techniques to probe ion migration, such as, for example, muon spin spectroscopy.[7] Moreover, there are a plethora of factors that can impact ion migration in a system (e.g., composition, pellet texture, and thermal/physical history) that are often disregarded during characterisation, which adds to the challenge of validating ionic migration experimentally.[7] Nevertheless, atomistic modelling also faces a number of challenges and relies on significant assumptions when attempts are made to provide insights into the in situ performance of materials. In this context, numerous outstanding experimental–computational reports on the nature of ion transport in anti-perovskite SEs have been published that overcome the inherent weaknesses of these two complementary paradigms, as described throughout this Chapter.

More recently, ML has been employed to identify and quantify the relevance different structural, chemical, and physical features have on ionic mobility within anti-perovskites. Kim and Siegel[118] used 600 DFT-calculated hopping barriers to train ML algorithms to predict ion migration barriers in 36 anti-perovskites with the general formula X_3BA (X = Li, Na, or K; B = O, S, or Se; A = F, Cl, Br, or I). The authors used mean decrease in impurity and individual conditional expectation plots to quantify the importance of the tested features in the ionic migration shown by the anti-perovskite systems. The study revealed that lattice properties, such as channel width and hopping distance, are the features that have the greatest impact on cation migration, with migration barriers decreasing as the channel width increases

and the hopping distance decreases. Such features were calculated to account for 50% of the total feature importance for interstitial migration and 70% of the importance for vacancy migration. Anion polarisability and defect formation energy were also considered significant features for ion mobility, comprising 22% for vacancy migration and 35% for interstitial migration, respectively. This study represents a significant advancement in the development and design of anti-perovskite SEs, as it uncovers a subset of impactful features for ion mobility, with many of those being elementary and simple to evaluate. The work also opens up the exciting possibility of attempting to generalise the method for other families of SE materials.

2.4 Grain Boundaries, Surfaces, and Electrolyte-Electrode Interfaces

Although the properties of individual materials are fundamental to device efficiency, the success of SSBs also depends heavily on the interfaces within. Nevertheless, as with many energy technologies, despite the importance of interfacial features, the current understanding around such themes in SSBs is limited compared to that of bulk materials, which is largely due to the complexity involved in their investigation both experimentally and computationally. However, recent years have seen a rise in the use of atomistic modelling in studying the structures, formation, and performance of interfaces in SEs and SSBs.

The interfaces formed within a SSB can be classified as heterogeneous (e.g., electrolyte–electrode interfaces) or microstructural (e.g., grain boundaries (GBs)).[7] Given that both types of interfaces can greatly impact ionic conductivity and the overall device performance, understanding the influence and characteristics of such interfaces is critical.[7,8,119] In this Chapter, we focus on highlighting the latest developments regarding the atomistic simulation of GBs, surfaces, and electrode-electrolyte interfaces.

We first consider GBs, which are defined as surfaces of contact between differently orientated crystallites that usually display different structural and composition features when compared to the bulk crystal.[7] GBs can significantly influence the overall conductivity of a

material, either positively or detrimentally.[7,120–123] Despite the fact that GBs are known to significantly impact the overall kinetics of ion transport, their pertinent properties and influence are still not fully understood, especially when compared to those of bulk materials.

To rectify this, Dawson *et al*. used large-scale MD simulations to explore ionic transport at a variety of representative low-energy GBs in Li_3OCl.[66] The authors predicted high GB concentrations and significant GB resistance in this material. They also proposed a polycrystalline model to quantitatively explore the effect of GBs on conductivity as a function of grain size. This work draws attention to the importance of considering the impact of GBs on ionic conductivity when exploring SEs, because solely considering the bulk material can lead to a significant underestimation of the activation energy for ionic diffusion. This investigation has inspired subsequent computational works focused on GBs in Li_3OCl[124,125] and indeed other SEs. For example, Chen *et al*.[124] used DFT to investigate the behaviour of GBs in Li_3OCl and also predicted high concentrations of GBs and GB resistance, aligned with the previous results reported by Dawson *et al*.[66]

More recently, Shen *et al*.[125] utilised an ensemble of first-principles calculations and phase field modelling to quantify the impact of GBs on ionic conduction in Li_3OCl. The authors considered the interaction between point defects and GBs in their simulations at different scales, providing insight into point defect segregation at the GBs. Usually, the high ionic conductivity shown by SEs is heavily reliant on the concentration of point defects in the lattice. As GBs are considered favourable sites for the segregation of point defects, it is natural to deduce that GB segregation could affect the distribution of point defects in the lattice and, consequently, impact its ionic conductivity. The work by Shen *et al*. showed that defect segregation varies with GB orientation, with Li-vacancy segregation energies lowering with the enhancement of GB coherency. This study also showed that defect segregation strengthens the detrimental impact of GBs on ionic conduction by approximately 1 order of magnitude. Nevertheless, the authors reported that such an impact is not significant for grain

sizes of hundreds of nanometres, suggesting that ionic conductivity could be improved by tuning the structure and grain size of the GBs.

In a combined experimental–theoretical study, Lee *et al*. investigated the role of GB resistance in affecting the total Li-ion conductivity in a range of hydrated anti-perovskites with the formula $Li_2OHCl_{1-x}Br_x$ (x = 0.0, 0.1, 0.3, 0.5, 0.7, 0.9, or 1.0).[126] Using DFT calculations, the authors were able to determine the Li-ion diffusion coefficients at the grains and GBs of the materials, with significantly reduced diffusion found for the latter. This was experimentally corroborated using electrochemical impedance spectroscopy on pellets with a controlled grain size.

More recently, Quirk and Dawson used first-principles calculations to establish design principles for GBs in four promising SE candidates, namely, Li_3OCl, Li_2OHCl, β-Li_3PS_4, and Li_3InCl_6[127]. As displayed in Figure 2.5(a), their calculations show that the GBs in Li_3OCl exhibit large barriers to ionic conductivity, while those in its hydrated material are less severe. This could be understood as a result of the perturbation of the electrostatic potential by the GBs in this material not being as significant (Figure 2.5(b)). The addition of highly polarisable ions or those that can adapt to electric fields by reorientation could mitigate the negative effects of electrostatic perturbations. Furthermore, their report showed that even when GBs do not significantly affect ionic conductivity, they can still disrupt the electronic structure and lead to undesirable electrical conductivity and potential lithium dendrite propagation (Figure 2.5c)). Their work also showed for the first time how correlated motion (e.g., the paddlewheel mechanism) can vary significantly at the GBs compared with the bulk.

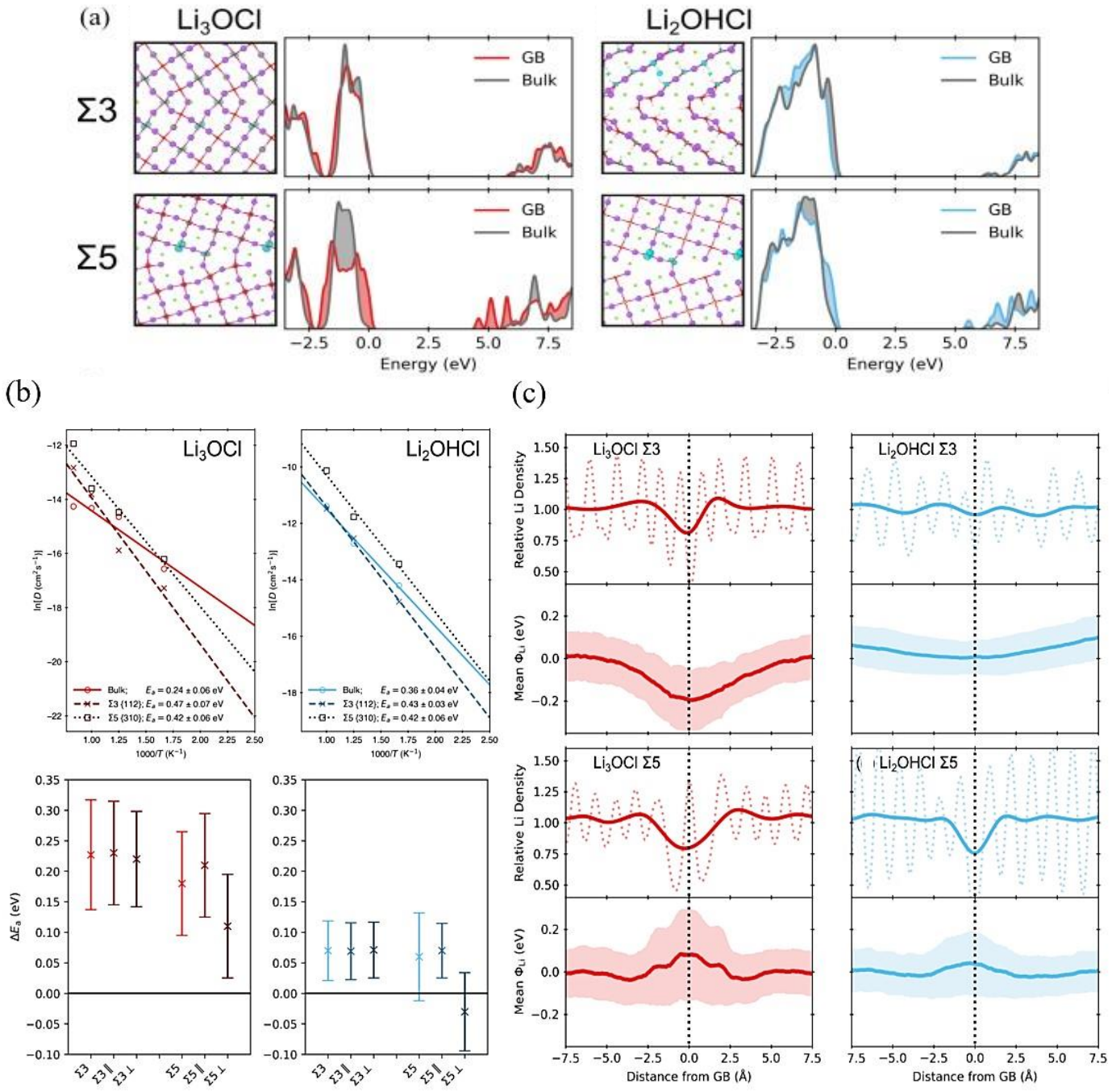

Figure 2.5. (a) Li-ion diffusivities for the bulk and GBs of Li_3OCl and Li_2OHCl. Relative activation energies in the GBs compared to bulk associated with the total diffusion and

decomposed into components parallel (∥) and perpendicular (⊥) to the GB plane are shown below each diffusivity plot. (b) Relative densities of Li (top panels) and mean electrostatic potentials around Li ions, φLi (bottom panels), as a function of distance from the GB for Li_3OCl and Li_2OHCl at 600 K. (c) Projected density of states with associated GB structures for Li_3OCl and Li_2OHCl. Energies are referenced against the position of the valence band maximum in the bulk-like region. Partial charge density isosurfaces show the highest occupied orbital (turquoise).[127]

We now shift our attention to the latest developments in the computational exploration of anti-perovskite solid electrolyte–electrode interfaces, which are essential in determining the stability and performance of SSBs at the device scale. Similar to GB investigations, the complexities involved in explicitly modelling electrolyte-electrode interfaces have led to a relative scarcity of such explorations. However, recent progress in this field for anti-perovskites has been made and resulted in an enhanced understanding of their interfacial phenomena.

Prior to exploring such interfaces explicitly using atomistic methods, it is necessary to determine which electrolyte surfaces are the most stable for the system of interest. Kim and Siegel[128] utilised DFT calculations to explore the stability of a selection of low-index nonstoichiometric surfaces of Li_3OCl with different terminations. Their simulations revealed that the LiCl-terminated (100) surface displayed the lowest surface energy of 0.19 J m^{-2} (at 300 K), suggesting that this surface is the most likely to form Li_3OCl at equilibrium. Using these surfaces, the authors investigated the electronic and thermodynamic properties of the interface between Li_3OCl and a Li metal anode on the atomic scale (Figure 2.6(a)). The authors computed a plethora of properties, including the work of adhesion, electrochemical windows, interfacial energy, wettability, and band edge shifts. Their calculations revealed the oxygen-terminated interface as the most thermodynamically stable interface, and the large work of adhesion found suggests that Li will wet Li_3OCl, indicating potentially low interfacial

resistance. However, the simulations showed that this interfacial interaction also reduced the electrochemical window of Li_3OCl, suggesting that there is a trade-off between strong interfacial bonding and electrochemical stability. Despite the reduction in the electrochemical window, it is noteworthy that the conduction band minimum remained ~1 V more negative than the Li/Li^+ redox potential, suggesting stability against reduction by the anode.

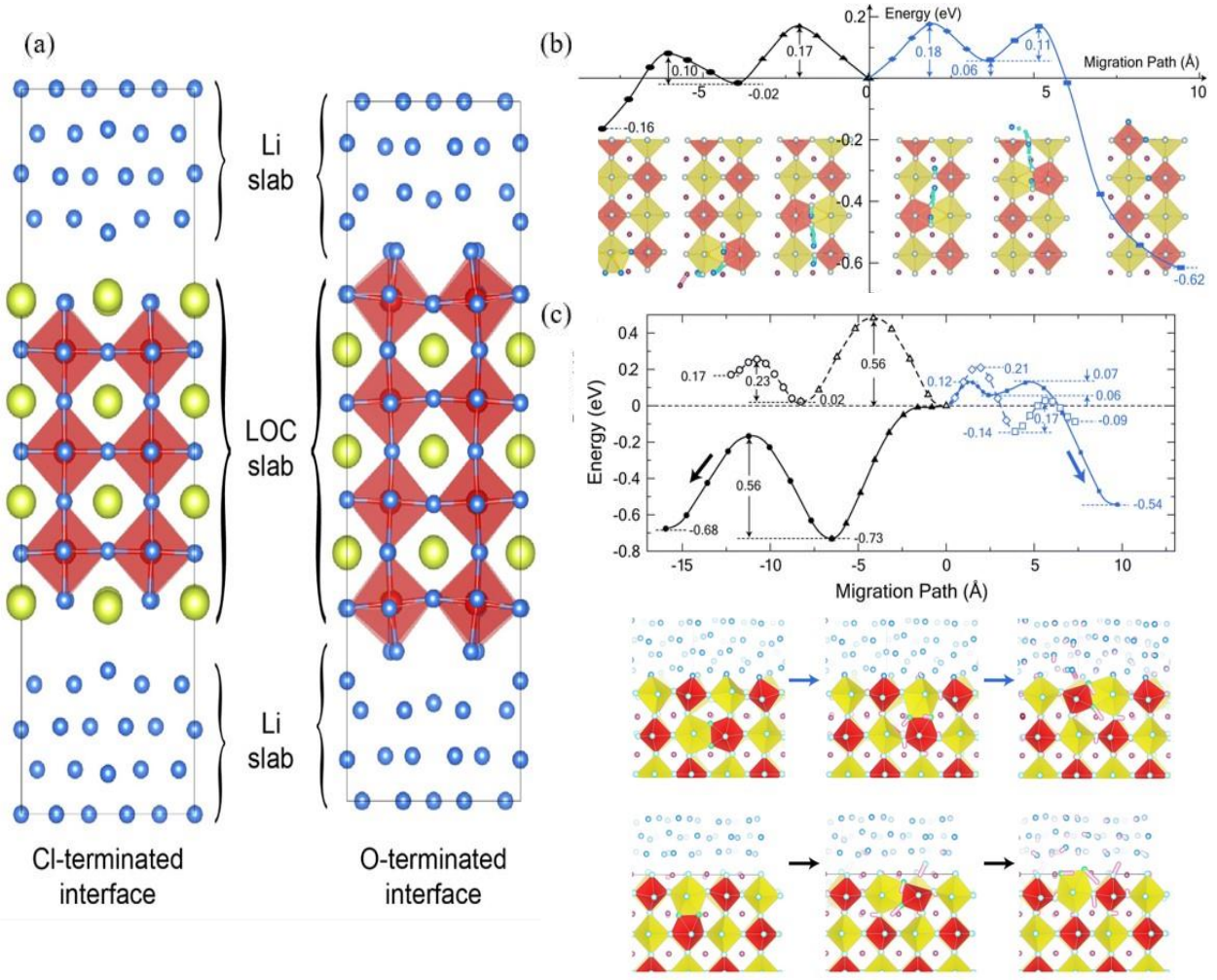

Figure 2.6. (a) Relaxed structures of Cl- and O-terminated interfaces consisting of seven layers of Li_3OCl (100) and bcc Li (100) planes. Energy profiles for the migration of a Na

interstitial (b) toward Na–I and Na–S–O surface terminations along the path shown in the bottom panel for snapshots during migration and (c) near Na_6SOI_2/Na (001) interfaces. Black (blue) curve in the top-left (top-right) panel represents the migration of a Na interstitial from an inner bulk site toward the Na–I (Na–S–O) surface and Na–I/Na (001) (Na–S–O/Na (001)) interface.[128,129]

A later study performed by Wu *et al.*[130] also found the Li–Cl-terminated (100) surfaces to be the most favourable in Li_3OCl. The interface between Li_3OCl and a Li metal anode was then studied by these authors via first-principles and AIMD calculations considering its interfacial charge distribution, geometric structure, electronic properties, and structural stability. They found that the interface was stable at 0 K and operating temperatures. Their AIMD calculations revealed that the Li-ion migration in their model was predominantly along the interface boundary. The calculated self-diffusion, conductivity, and activation energy of Li ions in the interface at 300 K were found to be 0.88 × 10–5 $cm^2\ s^{-1}$, 1.60 S cm^{-1}, and 0.09 eV, respectively. These values were greater than those for their counterparts in the bulk Li_3OCl bulk, suggesting that this interface positively contributes to ionic transport.

The interface between Li_3OCl and an almost ideal metallic intercalation cathode was investigated by Stegmaier *et al.*[96], in a DFT study that utilised a polarisable continuum model. The simulations showed that high Li vacancy concentrations will build up in a single layer of the electrolyte at the interface with the cathode, forming a compact double layer. The onset of oxidation for Li_3OCl and its subsequent products was investigated using first-principles simulations by Emly *et al.*[95] The authors calculated the onset of oxidation for Li_3OCl at 2.55 V relative to Li metal and predicted the formation of Li_2O_2 and LiCl. Richards *et al.*[131] also carried out oxidation analysis of this material and predicted the onset at 3.00 V relative to Li metal with LiCl, ClO_3, and $LiClO_3$ as products. As such products are electronic insulators, it is expected that a passivated interphase can be formed at high voltages, which could protect

the system from further oxidation.[7,132] Similar oxidation explorations have also been carried out for Na-based anti-perovskites. Lacivita *et al.*[133] found an oxidation limit of 1.79 V relative to Na metal for Na_3OBr with anodic reaction products Na_2O_2 and NaBr and an oxidation limit of 1.66 V relative to Na metal for Na_4OI_2 with NaI and $NaIO_3$ as anodic reaction products.

More recently, a first-principles study performed by Choe *et al.*[129] focused on the interface between a metallic Na anode and the Na-based anti-perovskite Na_6SOI_2. Their simulations showed that the Na_6SOI_2 (001) surface with two different terminations (i.e., Na–S–O and Na–I) could be used along with the Na (001) and (101) surfaces to form four different interface models due to their calculated exothermic interlayer binding energies, which ranged from −18.3 to −15.8 meV $Å^{-2}$, and formation energies of −28.0 to −21.5 meV $Å^{-2}$. The work analysed Na-ion conductivity at these interfaces and found that interstitial Na–Na dumbbell migration could be the reason for the ionic conductivity in the system due to a low calculated activation energy of ∼0.17 eV inside the electrolyte. The study also revealed that ionic migration toward the anode is favoured by the interstitial mechanism, while the reverse path is favoured by a Na vacancy-mediated mechanism (Figure 2.6(b),(c)).

2.5 Conclusions and Outlook

In this Chapter, some of the exciting latest developments in the computational design of anti-perovskite SEs, as a highly promising material family whose literature has experienced exponential growth in recent years, have been introduced. We have discussed the progress to date regarding the discovery and screening of new anti-perovskite systems and emphasised the importance of multitargeted studies of properties of interest (e.g., ionic conductivity, lattice distortion, thermodynamic stability, electrochemical stability, and synthesisability), especially when said properties compromise or contradict one another. The novel correlations between properties found for anti-perovskites have revealed, for example, the discovery that larger lattice distortions provide lower energy barriers for ion migration and stabilities and higher synthesis temperatures, suggesting a three-fold mobility-stability-synthesis trade-off.

We have commented on the widely accepted unsuitability of the traditional Goldschmidt tolerance factor for describing anti-perovskite systems, especially those containing heavy halides, and the recent report of a modified Goldschmidt tolerance factor as a successful descriptor for thermodynamic stability and band gap energy for anti-perovskites with Ruddlesden–Popper structures.

High-throughput screening and ML-assisted methods will be essential for the timely discovery and further development of anti-perovskite SEs. Herein, we have drawn attention to the latest reports in this field, including a general graph neural network model capable of assessing the synthesisability of anti-perovskites and a ML-assisted method that can accelerate the evaluation of kinetic properties in anti-perovskites by removing a critical bottleneck of such evaluations, namely, the use of time-consuming NEB calculations. Such works naturally raise the question of whether (or when) similar methodologies can be applied and obtained for more exotic anti-perovskites, for example, multivalent cation (e.g., Mg^{2+} or Ca^{2+})-based and low-DN anti-perovskites and structures with significant octahedral tilting.

In this context, anti-perovskites based on chemistries beyond Li and Na ions, such as systems containing mobile K, Mg, or Ca ions, also offer an intriguing research path. Due to their wide availability, such chemistries are becoming increasingly appealing to battery applications. In fact, several atomistic studies have already been published in this area, with compositions such as K_3OI, $K_{2.9}Ba_{0.05}OI$[134], Mg_3NAs, Ca_3NAs, and Ca_3PSb[135] delivering interesting results. Such interesting reports represent a new avenue for future investigations of high-performance anti-perovskites with more abundant elements for a wider range of energy storage applications.

In recent years, several different doping strategies that can have a significant impact on the ionic conductivity of anti-perovskites have also attracted interest. Herein, we have discussed recent findings for doped Li- and Na-rich anti-perovskite systems, with the majority of these suggesting a detrimental effect on ionic diffusion caused by fluorine doping. In contrast, the doping of anti-perovskite systems with divalent ions, especially Mg^{2+} and Ca^{2+},

has shown promising results (i.e., high ionic conductivity and/or low dopant-vacancy binding energies), highlighting a promising future direction for compositional design.

The ongoing debate regarding the domination of interstitial- or vacancy-mediated mechanisms in anti-perovskite systems has also been covered in this Chapter. Conflicting ideas have been proposed, and this trend continues with the debate not yet resolved. Interesting results focused on ion transport mechanisms in anti-perovskites have also been presented, with intriguing reports determining the correlations between lattice distortion and the barriers for ion migration. We have drawn attention to the importance of the paddlewheel effect in anti-perovskite solid electrolytes, including the first report of a double paddlewheel effect, where the rotational mobility of two anion groups promotes fast ion migration. It can be anticipated that such novel expansion of the paddle-wheel effect concept and further investigation of this in other anti-perovskite systems could greatly accelerate their future discovery and design. Furthermore, the exploration of ionic conductivity and transport mechanisms in SEs under the influence of stack pressures, which are typically required for practical SSBs, has so far been limited to only a few computational studies. This represents an important area of future work for anti-perovskite SEs and fast ion conductors generally.

We have also discussed the latest developments in the application of ML algorithms to predict ion migration barriers in anti-perovskite systems, with lattice properties, such as channel width and hopping distance, being found to be the features that have the greatest impact on cation migration. Such explorations represent a great leap forward in the design of anti-perovskite SEs as they uncover a subset of impactful features for ion mobility, with many of those being elementary and straightforward to determine.

Despite the recent rise in the number of studies focusing on interfacial explorations, this Chapter stresses how the complexity involved in computationally investigating interfacial phenomena and features has hindered advances in the field. However, recent results have provided fundamental knowledge around important properties and mechanisms. We illustrate the recent progress in the area by discussing studies that collectively suggest that the

detrimental impact of GBs on ionic conduction can be reduced by tuning the structure and grain size of the atomistic GBs, with anti-perovskites with larger grain sizes and coherent GBs expected to display enhanced Li-ion transport. We also comment on recent findings that point to the existence of a trade-off between strong interfacial bonding and electrochemical stability between Li_3OCl and Li metal anodes.

We have illustrated how transformative ML-assisted investigations are anticipated to be in the field of interfacial exploration, an area that still severely suffers from the complexities associated with accurately simulating the interfaces they focus on. To the best of our knowledge, no ML-based study has focused on exploring the interface between electrodes and anti-perovskite SEs.

As seen in the examples discussed in this Chapter, the current primary computational methods of choice for investigating interfaces in SSBs at the atomistic scale are based on either DFT or classical force field-based methods. However, the use of ML force fields for interfacial explorations is widely expected[136–138] to enable the DFT-accurate treatment of much more complex and larger simulation cells and time scales, which will be key for investigating interfacial problems, such as sources of charge accumulation and mass transfer resistance at the interfaces (e.g., GBs, chemical and electrochemical reactions, and decomposition products) and allow for the design of stable conducting interfaces in which practical SSBs can be built on.

Although progress has been recently made regarding the creation and exploitation of explicit atomistic models, there are still many unanswered questions. Furthermore, most studies have only focused on Li_3OCl and its hydrated form, leaving the understanding regarding other anti-perovskite compositions unexplored. However, these studies clearly show the potential of such simulations in both understanding and designing new anti-perovskite SEs with good performance in their bulk and at their interfaces.

Chapter 3 Computational Modelling Methods

3.1 Introduction

Computational modelling techniques play a critical role in tackling the critical challenges associated with the discovery, development, and design of solid electrolytes (SEs). As illustrated in Chapter 2, such techniques are well established and have been successfully used to predict novel promising anti-perovskite SE compositions and to provide a deeper understanding of their properties.

In this Thesis, three main computational techniques are used to explore the defect chemistry, properties, electrochemical stabilities, and ionic migration mechanisms in anti-perovskite systems: lattice statics, molecular dynamics (MD), and density functional theory (DFT). This Chapter provides a general overview of these selected techniques, with further details being available in the pertinent literature.[139–144]

The implementation of these techniques can be found in different public and commercial software packages. For the work carried out in this Thesis, the lattice statics calculations were performed using the General Utility Lattice Program (GULP)[145], MD simulations were carried out using the Large-scale Atomic/Molecular Massively Parallel Simulator (LAMMPS)[146] and DFT calculations were performed using the Vienna Ab initio Simulation Package (VASP)[147,148].

3.2 Empirical Force field-based Atomistic Simulations

The techniques covered in this Chapter are based on the evaluation of the interatomic forces in a system. The description of such interactions can be divided into two methodologies: empirical force field-based simulations and ab initio techniques. While the first type of methodology utilises empirically derived equations for the description of the interatomic forces, ab initio techniques rely on fundamental quantum mechanics and consider electron density. Consequently, ab initio calculations are more computationally expensive compared to atomistic simulations that use empirically derived equations and are, therefore, employed in the analyses of systems with a low atom count. Conversely, techniques that use empirically derived equations are widely used in calculations involving systems containing thousands of atoms and are widely used for modelling defects in large crystal structures. Pertinent aspects to empirical force field-based atomistic simulations are covered below.

3.2.1 Force field

The development of a force field that describes the energy of a system as a function of its coordinates is the starting point of any empirical force field-based atomistic simulation. Developing an appropriate force field is fundamental for empirical force field-based atomistic calculations as the level of accuracy the employed force field has in representing the targeted system can directly affect the calculations results.

The lattice energy (U_L) of a system is a critical property that needs to be calculated accurately by the employed potential model to deliver an appropriate system representation. Equation 3.1 is used to calculate U_L:

$$U_L = \sum_{ij} V_{ij}(r_{ij}) + \sum_{ijk} V_{ijk}(r_{ijk}) + \ldots \qquad (3.1)$$

Equation 3.1 contains a series expansion of pairwise, three-body, and increasingly larger body terms. However, in the majority of cases for computational simulations, it is not deemed necessary to expand such equation to include summations terms that account for larger number of ions that surpass the three-body terms. The summation terms explicitly shown in Equation 3.1 consider all ion pairs (*i* and *j*) and triplets (*i*, *j* and *k*) in an individual crystalline structure.

The representative potential model for each crystal structure is constituted by different interatomic equations whose summation gives the lattice energy. Alterations can be made to the parameters of these interatomic potentials to accurately represent pertinent chemical factors related to the targeted crystalline structure (e.g., bond strength, atomic radius, and mass).

The potential models used for the work presented in this Thesis are based on the Born model[149] (Equation 3.2), which focuses principally on the pairwise (two-body) terms from the lattice energy series expansion displayed in Equation 3.1:

$$U_L = \sum_{ij} \frac{q_i q_j}{4\pi\varepsilon_0 r_{ij}} + \sum_{ij} \Phi_{ij}(r_{ij}) + \ldots \qquad (3.2)$$

The two-body terms can be separated into short-range and long-range Coulombic interactions. The Coulombic interactions are considered in the first term of Equation 3.2, where q_i and q_j are the relevant ionic charges, ε_0 is the vacuum permittivity (8.854×10^{-12} F m^{-1}), and r_{ij} is the distance between the ions. The second term of Equation 3.2 accounts for

short-range interactions. Both attractive and repulsive forces are considered in short-range interactions, with attractive forces being caused by the presence of dispersive (London) interactions and repulsive forces being originated by the overlap of ion charge clouds.[140]

The modelling of short-range interactions can be performed by utilising analytical functions known as interatomic potentials. Two examples of the most used interatomic potentials are the Buckingham[150] and Morse[151] potentials. The advantages and disadvantages associated with the usage of these two potentials depend on what type of system is being modelled. While the Buckingham potential explicitly includes a term based on van der Waals interactions ($C_{ij}/\, r_{ij}^{6}$) and is suitable for modelling systems where non-covalent interactions are dominant (e.g., ionic materials), this potential does not explicitly model bond formation or dissociation[150]. Concomitantly, the Morse potential explicitly considers bond breaking and anharmonicity effects and is suitable for modelling systems where covalent bonds, rather than non-covalent interactions, dominate[151]. The computational calculations carried out in this Thesis are focused on anti-perovskite solid electrolyte materials and thus utilise the Buckingham potential model, which is described in Equation 3.3. The exponential term in Equation 3.3 that contains the *A* and ρ parameters accounts for the repulsion forces, while the equation fraction that contains the *C* term is related to the attractive forces in the system.

$$\Phi_{ij}(r_{ij}) = Aexp(\frac{-r_{ij}}{\rho_{ij}}) - \frac{C_{ij}}{r_{ij}^{6}} \qquad (3.3)$$

3.2.2 Ionic polarisation

The existence of an applied external field (e.g., the electrostatic field of a crystal) can lead to the distortion of an ion's electron charge cloud, causing polarisation. To accurately represent the targeted crystal structure, it is vital that the impact of polarisation is accounted

for in the force field used. The accurate modelling of polarisation is particularly pertinent when analysing the defect chemistry of crystals, as the impact of the polarisation caused by the field as a consequence of a charged point defect on the lattice relaxation around the defect is significant.

The description of polarisation can be performed using different models. The simplest model available is the point polarisable ion (PPI) model, described in Equation 3.4.

$$\mu_i = \alpha_i E \qquad (3.4)$$

where μ_i is the dipole moment, α_i is the ion's point polarisability, and E is the magnitude of the applied field.

The simplicity of the PPI model, however, generates issues when it is used in investigations of dynamics and dielectric properties in solid-state ionic materials. The PPI model becomes inadequate to treat such systems as it does not account for the coupling between the polarisation and the short-range repulsion, which is a critical factor when there are polarised ions within solids. Short-range repulsion is the product of the overlap between valence shell orbitals and polarisation, which has a direct impact on the shape of such orbitals. This coupling is capable of "dampening" the overall polarisation effects.[140]

Dick and Overhauser's[152] shell model stands as a well-stablished model that considers the vital coupling between the polarisation and the short-range repulsion. This model divides each ion into a core, which has a charge of X and is constituted of the nucleus and inner electrons, and a massless shell, which has a charge of Y and is formed solely by the polarisable valence electrons. The core and shell are connected by a harmonic spring of constant *k* and the model is illustrated in Figure 3.1. Equation 3.5 can be used to calculate the electronic polarisability of a free ion.

$$\alpha = \frac{Y^2}{k} \qquad (3.5)$$

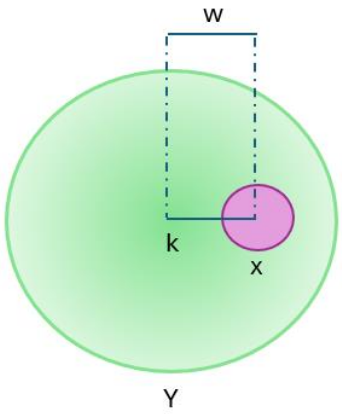

Figure 3.1. Schematic illustration of the shell model. The shell has a charge of Y and the core has a charge of X, with W being the distance between them. The spring constant is represented by *k*.

3.2.3 Deriving force field

The derivation of the components of potential models is needed to allow empirical force field-based atomistic simulations to generate accurate information about the systems they represent. Such derivation can be performed via the empirical fitting to experimental results and/or properties inherent to the materials. Experimental crystal structure data is generally the most easily available data for comparisons but other properties (e.g., elastic and dielectric constants) can also be used. Equation 3.6 can be used to analyse the quality of the parameter fitting.

$$SS = \sum_{i=1}^{N_{obs}} \omega_i (f_i^{obs} - f_i^{calc})^2 \qquad (3.6)$$

where N_{obs} is the number of observables, ω_i is a weighting factor and f_i^{obs} and f_i^{calc} represent the experimental and calculated values of the observables, respectively.

As can be deducted from Equation 3.6, in the unlikely case of a perfect match between the calculated model and the experiments results, the sum of squares (SS) will be equal to zero. Therefore, the fitting process is conducted with the goal of minimising the SS. In this context, the fitting process can be seen as the contrary of the energy minimisation process, as the ionic interactions are modified considering the structure instead of having the structure modified to minimise the energy.

3.2.4 Energy minimisation

The potential energy of a system can be described as a function of the coordinates of its atoms (i.e., the potential energy surface), which creates a dependency between the potential energy of the system and the atomic positions there contained. Each position represents a set of coordinates that are related to a specific atomic configuration. The multi-dimensional nature of the potential energy surface causes its visualisation and characterisation not to be straightforward. However, a greater understanding of such surfaces and systems can be acquired via the analysis of key component coordinates. The minima and the saddle point (SP) are two pertinent stationary points that contribute to the understanding of a potential energy surface:

1. Global/local minima: The point that displays the lowest energy is known as the global minimum and it is the most energetically favourable (i.e. the most thermodynamically stable) point/structure. Some systems display other minima known as local minima. Every minimum found corresponds to a stable state for the analysed system.

2. SP: The SP, also known as the transition state, is the point that displays the maximum energy along the lowest energy path between two minima. Finding a SP can suggest the presence of a reaction pathway.

As the first derivatives of both types of stationary points are equal to zero, their second derivates with respect to distance will be needed to allow for their identification. Minima will display solely positive eigenvalues in the Hessian matrix of second derivatives whereas the SPs will present negative eigenvalues.

Energy minimisation algorithms allow for the identification and analysis of such stationary points. During an energy minimisation calculation, the structural parameters of the analysed system (e.g., atomic coordinates and cell dimensions) are updated continuously until the overall configuration that provides the lowest possible energy for the investigated system is found. When such point is found, the system is considered "optimised".

There are different energy minimisation methods available and different software will allow for different methods to be used. The choice of an energy minimisation method is not trivial as different methods have different impacts on the computational costs of the simulations they are applied to. Two main energy minimisation methods were used in the work presented in this Thesis, namely, the conjugate gradient (CG) and Newton-Raphson methods, as described below.

Conjugate Gradient Method

The CG method is based on a set of orthogonal search vectors ($\boldsymbol{d}_i$). This algorithm finds the minimum of the energy surface by minimising the energy with respect to each direction. The CG method provides a new search vector ($\boldsymbol{d}_i$) from the previous search vector ($\boldsymbol{d}_{i-1}$), the current gradient (g_i) and the previous gradient (g_{i-1}), as shown in Equations 3.7 and 3.8.

$$\boldsymbol{d}_i = -g_i + \beta_i \boldsymbol{d}_{i-1} \qquad (3.7)$$

where:

$$\beta_i = \frac{g_i . g_i}{g_{i-1} . g_{i-1}} \qquad (3.8)$$

The new search vector can be used to calculate a position nearer the minimum ($\boldsymbol{x}_{i+1}$), as shown in Equation 3.9.

$$\boldsymbol{x}_{i+1} = \boldsymbol{x}_i + \alpha_i \boldsymbol{d}_i \qquad (3.9)$$

where α_i represents the step length that is iteratively found using the same line search technique.

Advantages related to the use of the CG method compared to other simpler methods (i.e., the steepest descent method) include the fact that it requires fewer interactions to find the minimum energy of the system and that the shape of the potential well does not hinder the minimum convergence. In terms of computational time, the time needed for the calculation to be performed for each step is relatively rapid.

Newton-Raphson Method

The Newton-Raphson method utilises information based on first (gradient)- and second (Hessian matrix)-order derivatives to provide the minimum of the system. The calculation of a new iteration ($\boldsymbol{x}_{i+1}$) can be performed as shown in Equation 3.10.

$$\boldsymbol{x}_{i+1} = \boldsymbol{x}_i - H_i^{-1} g_i \qquad (3.10)$$

where the atomic coordinates of the current configuration are given by $\boldsymbol{x}_i$, the gradient for that point is g_i and the reciprocal of the Hessian matrix is represented by H_i^{-1}. The atomic coordinates can then be iteratively updated following Equation 3.10.

The energy minimisation process can become troublesome when using the Newton-Raphson method in cases where the starting configuration is very far from its optimised form. Therefore, it is important to choose an appropriate atomic configuration before using this method. Such configuration can be achieved by using another energy minimisation technique first (e.g., the conjugate gradient method) to bring the initial configuration closer to its optimum form and then use the Newton-Raphson method to rapidly find the minimum.

The use of the Hessian matrix allows for the rapid convergence seen in the Newton-Raphson method. However, it also significantly augments the associated computational costs. Additionally, the Hessian matrix needs to have solely positive eigenvalues to avoid the identification of SPs instead of the minimum.

3.3 Periodic Boundary Conditions

Considering periodic boundary conditions is fundamental for the modelling of large solid-state systems as they can significantly minimise the computational costs associated with the simulations needed. Due to their symmetric nature, crystalline solids can be divided into unit cells, which are the simplest repeating unit in a crystal. When periodic boundary conditions are considered, the unit cell is simulated surrounded by copies of itself (Figure 3.2). While the ions contained in the unit cell are able to interact with all the ions in the simulation, including each other, the ions contained in the unit cell replications can only

interact with the ions in the original unit cell and cannot interact with each other. In this context, periodic boundary conditions can be successfully used to represent crystalline systems.

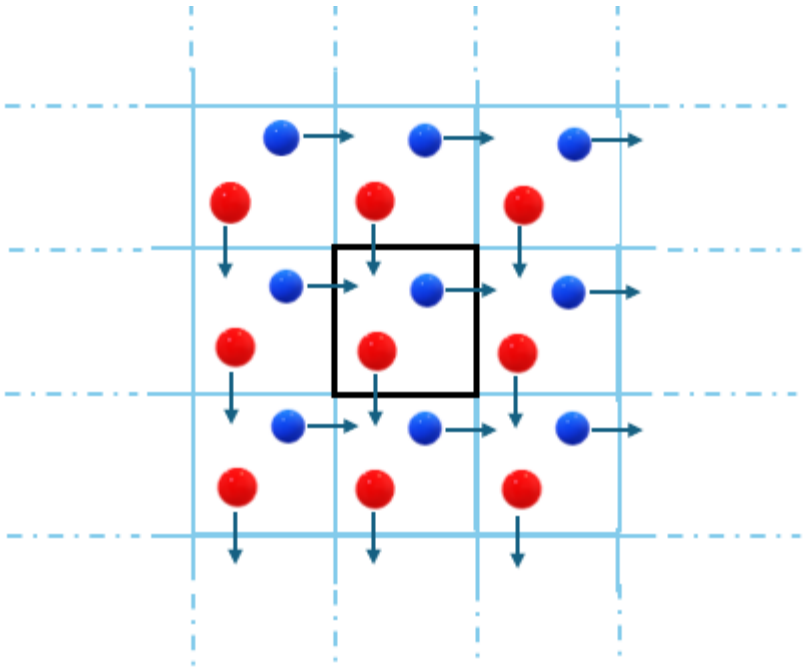

Figure 3.2. Schematic illustration of periodic boundary conditions.

3.4 Point Defects

Due to entropy, every crystal structure will possess defects. The types of defects that are most likely to be displayed by crystalline systems and that are most pertinent to the work presented in this Thesis are shown in Figure 3.3 and can be divided into four types:

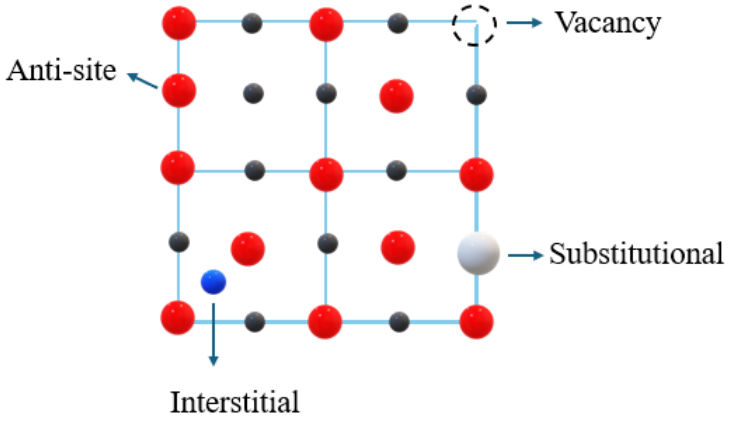

Figure 3.3. Schematic representation of a two-dimensional cross section of a simple crystal lattice, illustrating different defect types.

Vacancy: A lattice site where an atom would usually be expected that is void.

Interstitial: An ion located at a lattice region that is not expected to be occupied.

Anti-site: Two different neighbouring ions exchange lattice sites.

Substitutional: A dopant ion located at a given lattice site.

The creation of a defect significantly impacts the atoms surrounding the defect centre as it generates a Coulombic perturbation in the disordered region. As the lattice relaxation impacts the crystal symmetry, considering the system as an ensemble of symmetric unit cells is not suitable in such cases.

The Mott-Littleton approximation[153] is a method used to account for the lattice relaxation around the defect centre. The Mott-Littleton approximation divides the area around

the created defect into two spherical regions, as shown in Figure 3.4. The first region, region I, is closest to the defect centre and includes the defect centre itself and all ions surrounding it. Due to the proximity of region I to the defect centre and thus to the origin of perturbation, the lattice relaxation in this region will be stronger than in any other regions and the relaxation of the ions will be calculated explicitly for region I. The second region, region II, starts at the border of region I and extends to infinity. This region is subdivided into region IIa, closest to the defect centre, and region IIb. The relaxation of ions in region IIa is allowed and is considered as impacted by the central defect, whereas region IIb is treated as continuous, and the impact of the defect is considered to only be dielectric. To avoid lattice relaxation occurring within region IIb, it is fundamental that the defect energy has converged with respect to the region sizes. The radius of region I and the difference in the radii of regions I and IIa should ideally be greater than the potential cutoff radius.

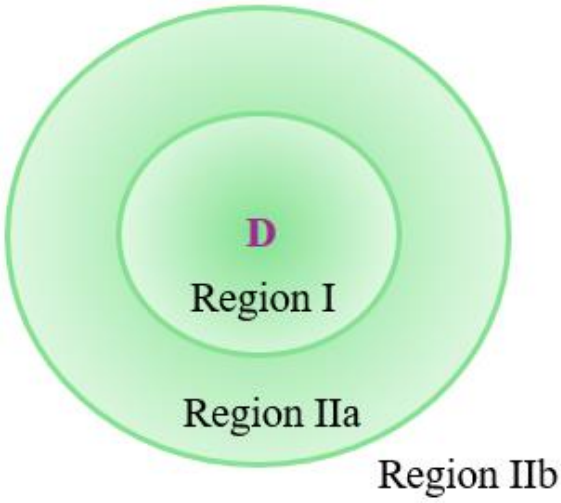

Figure 3.4. Schematic representation of the Mott-Littleton approximation, with D corresponding to the defect centre.

3.4.1 Ion migration

As established in Chapters 1 and 2, the ability to deliver efficient ion transport is an essential feature that promising SE candidates need to display. Although ion transport can occur via several different mechanisms, two mechanisms have been deemed more pertinent and common for anti-perovskite SEs, as discussed in Chapter 2, namely, the vacancy- (i.e., vacancy hopping) and interstitial-based mechanisms. Details on such mechanisms are given in Figures 3.5 and 3.6.

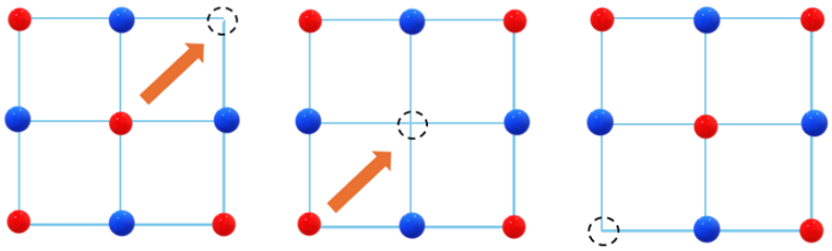

Figure 3.5. Schematic representation of a two-dimensional cross section of a crystal lattice depicting the vacancy-based mechanism. The repeating ionic exchange with a neighbouring vacancy allows for ion migration.

The vacancy-based mechanism is based on the migration of an ion to a neighbouring vacancy, whereas the interstitial-based mechanisms is based on the migration via either exchange with lattice ions or between interstitial sites.

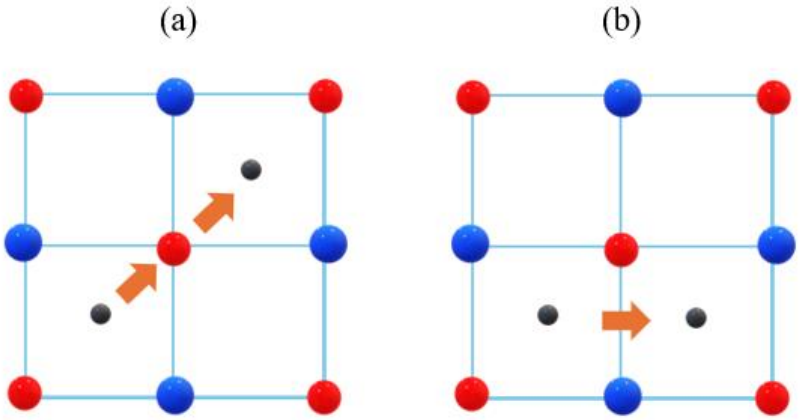

Figure 3.6. Schematic representation of a two-dimensional cross section of a crystal lattice depicting the interstitial-based mechanism. (a) An interstitial ion migrates to a site occupied by a lattice ion, leading the lattice ion to migrate to a nearby interstitial site. (b) An interstitial ion migrating to another interstitial site.

The concentration of a certain type of defect can provide a preference for a certain type of mechanism to develop across the investigated system. For example, a system with a high concentration of interstitial defects could potentially display a preference for interstitial-based ionic migration. The types of defects that are preferably formed in a system can also impact the efficacy of the ionic migration. For example, as interstitial defects are more mobile, ionic transport that occurs via interstitial-based mechanisms can potentially display faster migration. Ionic trajectories obtained via MD studies and energy barriers acquired via nudged elastic band (NEB) calculations are powerful tools to assess the pertinence of different ionic transport mechanisms in different systems. More details on MD studies and NEB calculations are given in Sections 3.5 and 3.8, respectively.

3.5 Molecular Dynamics

Energy minimisation calculations consider systems at absolute zero temperature and, consequently, cannot provide information on the effects of thermal energy and kinetic energy associated with the investigated system. Conversely, MD simulations consider the kinetic energy of the atoms in the system and the variable of temperature is incorporated in the MD calculations. Differing from energy minimisation techniques, MD calculations can overcome small local energy barriers (i.e., barriers in the order of a few k_BT) and find configurations with higher thermodynamic stabilities.

MD simulations have proved to be excellent tools in assessing ion trajectories within solid-state crystals.[7,8,61,154] Such studies can provide important information regarding the dynamical properties (e.g., crystal vibrations and ion migration mechanisms) pertinent to the investigated system.

The acceleration of an atom in space can be calculated via Newtonian equations of motion, as shown in Equation 3.11.

$$\boldsymbol{f} = m\frac{\boldsymbol{d^2r}}{dt^2} = m\boldsymbol{a} \qquad (3.11)$$

where f is the force acting on the atom, m is the mass of the atom, d^2r is the second derivative of the atomic position with time (dt^2).

MD calculations iteratively solve the Newtonian equations of motion. Every time an infinitesimal time step (Δt) has passed, MD simulations calculate the iterations ($\boldsymbol{x}_i$) and velocities ($\boldsymbol{v}_i$) again, with the acceleration of the particle being used to calculate velocities at times $t + \Delta t$. This is illustrated in Equations 3.12 and 3.13.

$$\boldsymbol{x}_i(t + \Delta t) = \boldsymbol{x}_i(t) + \boldsymbol{v}_i(t)\Delta t + \frac{1}{2}\boldsymbol{a}(t)\Delta t^2 \qquad (3.12)$$

$$\boldsymbol{v}_i(t + \Delta t) = \boldsymbol{v}_i(t) + \boldsymbol{a}(t)\Delta t \qquad (3.13)$$

A major source of inaccuracy related to MD simulations is the assumption that the force acting on the atom is constant between *t* and *t* + Δ*t*. In real systems, the forces acting on atoms will not be constant and will be affected by interatomic distances. To minimise this inaccuracy, it is fundamental that the value of Δ*t* is small enough that integration errors are negligible. When the analysis of the motion of the ions over larger time scales is desired, the application of numerical integration algorithms is needed.

3.5.1 Integration algorithms

Several integration algorithms are available for the integration of the Newtonian equations of motion, with Taylor expansions generally being used by them to calculate accelerations, positions, and velocities approximations.

The Verlet algorithm[155] is a well-established integration algorithm that can be used in MD calculations. The Verlet algorithm is generated through the approximation of the ionic trajectories as Taylor series in terms of the current ionic positions which is truncated at the third derivative (Equation 3.14).

$$\boldsymbol{r}_{t+\Delta t} = \boldsymbol{r}_t + \boldsymbol{v}_t\Delta t + \frac{\boldsymbol{a}_t}{2}\Delta t^2 + \frac{\boldsymbol{b}_t}{6}\Delta t^3 + \theta(\Delta t^4) \qquad (3.14)$$

where $\boldsymbol{r}_t$ is the ionic position at time t, $\boldsymbol{v}_t$ is the velocity at time t, Δt is the time step, $\boldsymbol{a}_t$ is the acceleration, $\boldsymbol{b}_t$ is the acceleration changes and θ is an error term. By adding the $\boldsymbol{b}$ term into the calculation, the simulation can account for the changes in force. As discussed in section 3.5, the disregard of such changes was a source of inaccuracy. Facing the difficulty associated with the calculation of the **b** term, Loup Verlet developed a mathematical trick to facilitate its calculation.

Verlet realised that the inclusion of the third derivative can be implicitly carried out using the information acquired from the previous step ($t-\Delta t$). Equation 3.15 describes the Taylor series at the previous step. The overall algorithm developed by Verlet can be seen in Equation 3.16, being a summation of Equation 3.14 and 3.15, and it shows how the $\boldsymbol{b}$ term is no longer explicitly needed in order to solve the equation. It is important to notice, however, that although this mathematical trick solves the third derivative issue, it also causes the total error to increase, as the errors of Equation 3.14 and 3.15 are carried forward into Equation 3.16.

$$\boldsymbol{r}_{t-\Delta t} = \boldsymbol{r}_t - \boldsymbol{v}_t \Delta t + \frac{\boldsymbol{a}_t}{2} \Delta t^2 - \frac{\boldsymbol{b}_t}{6} \Delta t^3 + \theta(\Delta t^4) \qquad (3.15)$$

$$\boldsymbol{r}_{t+\Delta t} = 2\boldsymbol{r}_t - \boldsymbol{r}_{t-\Delta t} + \boldsymbol{a}_t t^2 \, \Delta t^2 + \theta(\Delta t^4) \qquad (3.16)$$

In order to obtain the total energy of the system, it is necessary to consider its associated kinetic energy and, therefore, the calculation of ionic velocities is needed. Additionally, ionic velocities are used to guarantee the desired system temperature. Verlet trajectories can be used to calculate velocities by subtracting Equation 3.14 from Equation 3.15, as shown in Equation 3.17.

$$\boldsymbol{v}_t = \frac{\boldsymbol{r}_{t+\Delta t} - \boldsymbol{r}_{t-\Delta t}}{2\Delta t} + \theta(\Delta t^2) \qquad (3.17)$$

It is noteworthy that the Verlet algorithm is not self-starting, having its calculations based on information acquired in previous steps. In practice, initial ionic velocities are chosen randomly and guarantee that the system has the initial desired temperature and no translational momentum. As seen in Equation 3.17, another pertinent facet of the Verlet algorithm is its large level of inaccuracy (Δt^2).

3.5.2 Time step and equilibrium

Choosing the time step (Δt) to use in MD simulations is a highly pertinent task. The use of an exceedingly large time step can give rise to instabilities in the system, as atoms could be able to move unphysical distances and collide. Concomitantly, a redundantly short time step will lead the simulations to be excessively laborious, as more force evaluations will be needed to produce the same amount of simulation time, causing the computational cost of such simulations to significantly rise. In practice, time steps ranging from 0.1 to 2 fs are generally found to be suitable for MD simulations. Factors such as atomic weight and temperature can also affect time step requirements, with atoms that display low atomic weights (e.g., Li and H) and simulations that are performed at higher temperatures requiring smaller time steps.

MD simulations start by allowing the initial configuration of the system to reach equilibrium. The monitoring of different properties such as the total and kinetic energies is conducted during this period and the equilibrium is considered obtained when such properties converge. Such period generally lasts for tens of thousands of time steps. After the

equilibrium period is finished, the production period is started; this is the period where the desired statistics can be achieved.

3.5.3 Ensembles

The description of the constraints used in a system during a MD simulation can be carried out using ensembles. For example, the micro-canonical ensemble (NVE) guarantees that the number of atoms (N), the volume of the simulation cell (V) and the total energy of the system (E) are constant. It is noteworthy that the kinetic and potential energies can still change, as long as the total energy of the system remains constant. This can be observed in Equation 3.18.

$$H = K + V \qquad (3.18)$$

where the total energy of the system is represented by the Hamiltonian (*H*) and the kinetic and potential energies are *K* and *V*, respectively.

The canonical (NVT) and isobaric-isothermal (NPT) ensembles represent alternatives to the micro-canonical ensemble where the temperature stands as one of the parameters kept constant. This allows for the system to be investigate as a function of the temperature, in the case of the canonical ensemble, or of the pressure, in the case of the isobaric-isothermal ensemble. All the MD simulations presented in this Thesis used the NPT ensemble.

The control of the temperature can be carried out by using mathematical thermostats during MD simulations. Many mathematical thermostats are available such as the Andersen[156], the Berendsen[157] and the Nosé-Hoover[158] thermostats. The Nosé-Hoover

thermostat is one of the most efficient methods for constant-temperature MD calculations and was the thermostat of choice for all the MD work presented in this Thesis.

The Nosé-Hoover thermostat includes the effect of a constant temperature through the introduction of an extra degree of freedom(s) and the conjugate momentum. This Hamiltonian is given in Equation 3.19.

$$\widehat{H} = \sum_i \frac{p_i^2}{2m_i s^2} + U(\boldsymbol{r}^N) + \frac{p_s^2}{2Q} + (3N+1)k_B T \ ln\ s \qquad (3.19)$$

where H is the Hamiltonian, p is related to the momenta, m represents the mass, N is the number of particles, k_B is the Boltzmann constant, and T is the temperature. The term Q serves to control the coupling of the heat bath to the system needs to be selected in a way that guarantees the canonical ensemble. While the first two terms are related to the kinetic and potential energy of the system, respectively, the third and fourth terms are related to the kinetic and potential energy of the introduced coordinate (s).

3.5.4 MD data analysis

The production period of MD simulations can be used to acquire relevant information concerning properties (e.g., activation energy) and ionic diffusion pertinent to the investigated system. Such information can be obtained from mean squared displacements (MSDs) calculations. MSDs represent the displacement of atoms in the cell from their initial conditions after time t. This measurement can be defined by Equation 3.20 below, where $r_i(0)$ and $r_i(t)$ are the positions of atom i at times 0 and t, respectively, and N is the number of atoms.

$$MSD(t) = \frac{1}{N}\sum_{i=1}^{N} |r_i(t) - r_i(0)|^2 \qquad (3.20)$$

The relationship between MSD and the self-diffusion coefficient (*D*) comes from the MSD gradient, as can be seen in Equation 3.21, where *d* is the dimensionality of the diffusion within the system. For all the MSD simulations presented in this Thesis, the diffusion was considered three dimensional within the investigated systems, which is described by Equation 3.22.

$$MSD(t) = 2dDt \qquad (3.21)$$

$$MSD(t) = MSD(0) + 6Dt \qquad (3.22)$$

Arrhenius plots of diffusion data can be obtained from MSD data generated at several different temperatures. Such plots can be used to estimate the activation of ionic diffusion energies. Equation 3.23 is used to acquire the Arrhenius plots, where *D* is the slope of the MSD plot at temperature *T*, *R* is the gas constant and E_a is the activation energy. Therefore, through this method, it is possible to obtain pertinent information concerning diffusion barriers that static lattice simulations would not be able to provide.

$$lnD = \frac{-Ea}{RT} + lnA \qquad (3.23)$$

Additionally, MD calculations can provide relevant insights concerning the spatial properties of ionic transport within the investigated system, revealing fundamental information about the diffusion mechanics. Time-averaged atomic density plots can be generated from MD trajectories to successfully acquire information about diffusion pathways in solid-state systems.

3.6 Density Functional Theory

As discussed in section 3.2, the techniques covered in this Chapter can be divided into two methodologies: techniques based on empirical potentials and ab initio techniques. Whilst the former use empirically derived equations for the description of the interatomic forces, the latter rely on fundamental quantum mechanics and develop models from theoretical properties. In this context, ab initio techniques stand as a critical tool in the study of ground-state electronic properties that cannot be analysed via empirical methods (e.g., band structure, charge distribution and orbital occupancies).

Techniques based on quantum mechanics focus on solving the Schrödinger equation and deriving a wavefunction. Equation 3.24 describes the simplest form of the Schrödinger equation.

$$H\psi = E\psi \qquad (3.24)$$

where H is the Hamiltonian operator, ψ represents the wavefunction and E represents the total energy of the system.

The wavefunction is the equation term that contains all information related to the spins and positions of the atoms in the analysed system. Consequently, in theory, the calculation of material properties can be performed via the analysis of the wavefunction. The exact solution can be derived from the identification of the suitable Hamiltonian form. The full Hamiltonian is described in Equation 3.25.

$$H = T_e + T_n + V_{int} + V_{nn} + V_{ext} \qquad (3.25)$$

where T_e is the electronic kinetic energy, T_n represents the nuclear kinetic energy, V_{int} is related to electron-electron interactions, V_{nn} describes nuclear-nuclear repulsions and V_{ext} represents the electron-nuclei interactions. The summation of the V_{int}, V_{nn}, and V_{ext} terms leads to the potential energy of the system.

The complete description of a system can be acquired by adding the terms shown in Equation 3.25 over all the nuclei and electrons in the system, generating Equation 3.26.

$$H = -\frac{h^2}{2m_e}\sum_i \nabla_i^2 - \sum_I \frac{h^2}{2M_I}\nabla_I^2 + \frac{1}{2}\sum_{i\neq j}\frac{e^2}{|r_i - r_j|} + \frac{1}{2}\sum_{I\neq J}\frac{Z_I Z_J e^2}{|R_I - R_J|} - \sum_{i,I}\frac{Z_I e}{|r_I - R_I|} \qquad (3.26)$$

where M_I is the mass of nucleus I, R_I is the position of nucleus I, Z_I is the charge of nucleus I, m_e is the mass of electron i and r_i is the position of electron i.

The full solution of the Schrödinger equation is mathematically unviable for non-basic systems and such full analytical solutions cannot be acquired. Numerical solutions, however, can be obtained and computational power is essential for this task. An ensemble of approximations is necessary to facilitate solutions to be found.

The first approximation used is the Born-Oppenheimer approximation, which separates nuclear and electronic motion. The significant disparity between the mass of the nucleus and the mass of surrounding electrons impacts their velocities, with electrons moving so much faster that one could safely consider that the nucleus is static. The Born-Oppenheimer approximation leads to the Hamiltonian to be updated as the electronic Hamiltonian, as described in Equations 3.27, 3.28, and 3.29.

$$H_{elec} = T + V_{int} + V_{ext} \qquad (3.27)$$

$$H_{elec} = -\frac{h^2}{2m_e}\sum_i \nabla_i^2 + \frac{1}{2}\sum_{i\neq j}\frac{e^2}{|r_i - r_j|} - \sum_{i,j}\frac{Z_I e}{|r_I - R_I|} \qquad (3.28)$$

$$H_{elec} = -\frac{h^2}{2m_e}\sum_i \nabla_i^2 + \frac{1}{2}\sum_{i\neq j}\frac{e^2}{|r_i - r_j|} + \sum_i V_{ext}(r_i) \qquad (3.29)$$

Although the Born-Oppenheimer approximation allows the wavefunction to be only dependent on the electronic configuration of the investigated system, the full solution for this equation is still not acquirable for non-simple systems as there is a plethora of electron-electron interactions to be considered, which makes the associated computational costs the limiting factor. Therefore, more approximations are still needed, as described below.

3.6.1 Hohenberg-Kohn theorems

A simplified model for the calculation of the many-electron Schrödinger equation can be obtained via the application of the Hohenberg-Kohn theorems[159]. The two Hohenberg-

Kohn theorems form the fundamental principles of DFT, with Walter Kohn being awarded the 1998 Nobel Prize in Chemistry for the development of DFT[160]. The theorems can be defined as:

i. The three-dimensional electron density of a many-electron system uniquely determines the ground state properties of that system.
ii. The energy of a system can be defined as a functional of the electron density, with the minimum energy functional corresponding to the ground-state electron density.

The first theorem removes the necessity of solutions for the N electron wavefunction, leaving only the information regarding the three-dimensional electron density as necessary. The second theorem states that the ground-state electron density of the system can be calculated through the calculation of the energy functional of the system, which will define all the other properties of the system.

The energy functional defined by Hohenberg and Kohn can be seen in Equation 3.30.

$$E[\rho(\mathrm{r})] = \int \mathrm{V_{ext}}(\mathrm{r})\rho(\mathrm{r})\mathrm{dr} + F[\rho(\mathrm{r})] \qquad (3.30)$$

where the first term is related to the interactions between electrons and the external potential, and the second term concerns the kinetic information of the electrons and terms derived from electron-electron interactions.

While the Hohenberg-Kohn theorems provide a simplified model for the calculation of the many-electron Schrödinger equation, and hence the foundations for the development of DFT, they are unable to provide a form for $F[\rho(\mathrm{r})]$. Therefore, information needed to calculate the ground-state of the system is still missing. The application of the Hohenberg-Kohn

Theorems is not, however, capable of providing a form for $F[\rho(r)]$ and thus further approximations are still needed to calculate the ground-state.

3.6.2 Kohn-Sham equations

In 1965, Kohn and Sham introduced a method that allow for the calculation of the ground-state through an ensemble of equations known as the Kohn-Sham equations[161], building the foundation of modern DFT. In their approach, Kohn and Sham state that for a system with a set of interacting electrons and with electron density ρ(r), an equivalent system endowed with the same ρ(r) can be derived with non-interacting electrons. The application of this approach leads to Equation 3.31.

$$F[\rho(r)] = E_{ke}[\rho(r)] + E_H[\rho(r)] + E_{xc}[\rho(r)] \qquad (3.31)$$

where $E_{ke}[\rho(r)]$ is the kinetic energy of the non-interacting electrons, $E_H[\rho(r)]$ is the Hartree term that contains the Coulombic energy of the electron-electron interactions and $E_{xc}[\rho(r)]$ is the contribution from the exchange-correlation term and the energy disparity between the interacting electrons and the non-interacting electrons to the energy functional.

The exchange-correlation term unites the unknown terms into a single approximated contribution. While E_{ke} and E_H are known, the exchange-correlation term is solely known for selected simple systems. However, its definition was critical for the establishment of modern DFT.

The Hartree term is described in Equation 3.32 and is the summation of the classical pairwise interactions between charge densities.

$$E_H[\rho(r)] = \frac{1}{2}\iint \frac{\rho(r_1)\rho(r_2)}{r_1 - r_2} dr_1 dr_2 \qquad (3.32)$$

The Kohn-Sham-based Schrödinger equation can be derived from the Hohenberg-Kohn theorems and the Kohn-Sham energy functional, as described in Equation 3.33.

$$\left[\frac{-h}{2m_e}\nabla^2 + V_{eff}(r)\right]\psi_i(r) = \varepsilon_i\psi_i(r) \qquad (3.33)$$

where ψi(*r*) is related to the Kohn-Sham orbitals of non-interacting electrons, ε_i is related to the orbital energies and V_{eff} is the effective potential for the system.

A stationary solution for the Schrödinger equation can be derived from Equation 3.33 to deliver Equation 3.34. Equation 3.35 shows the relationship between the exchange correlation potential and the exchange-correlation energy.

$$V_{eff}(r) = V_{ext}(r) + \int \frac{\rho(r')}{[r - r']} dr' + V_{xc}(r) \qquad (3.34)$$

$$V_{xc}(r) = \frac{\delta E_{xc}[\rho(r)]}{\delta\rho(r)} \qquad (3.35)$$

where $V_{ext}(r)$ and $V_{xc}(r)$ are the external and the exchange correlation potentials, respectively.

Through this method, it is possible to iteratively find solutions to the Schrödinger equation. An initial guessed electron density is used to calculate an initial effective potential which is then utilised to derive the Kohn-Sham orbitals as per Equation 3.33. Equation 3.36 can then be used to estimate an improved electron density.

$$\rho(r) = \sum_{i}^{N} |\psi_i(r_i)|^2 \qquad (3.36)$$

Posteriorly, the improved electron density is utilised to update the effective potential. This process is repeated until the obtained electron density converges. Following the Hohenberg-Kohn theorems, the obtained electron density allows for the definition of all ground-state properties as it corresponds to the ground-state energy. It is important to note that a valid approximation of the exchange-correlation function is needed to generate a value for the effective potential at each step as the exact form of the exchange-correlation term is still unknown.

3.6.3 Approximations to exchange-correlation functional

Although the exact form of the exchange-correlation functional is unknown for general systems, certain constraints and properties allow for the creation of approximations that can be used to perform DFT calculations with satisfactory accuracy and computational costs. The choice of an approximation functional depends on the type of DFT calculations needed and on the systems there involved. Such choice is critical as the use of a non-appropriate functional can greatly impact the acquired results. Although there are various

approaches available, functionals based on the local density approximation (LDA) and on the generalised gradient approximation (GGA) are widely and successfully used. Details concerning the LDA and the GGA are provided below.

Local Density Approximation (LDA)

The LDA is a simple exchange-correlation functional that has become one of the most widely used.[162] Despite its simplicity, the LDA has been successful in calculating a range of ground-state properties in appropriate systems (i.e., systems without very inhomogeneous charge distributions, metallic systems and non-isolated systems). Although the exact form of the exchange-correlation functional is unknown for general systems, it has been successfully calculated for the case of the uniform electron gas. The LDA treats the exchange-correlation per electron of a system with an electron density of ρ(r) and that of the uniform electron gas with the same electron density of ρ(r) as equivalents (Equation 3.37).

$$E_{xc}^{LDA}[\rho(r)] = \int \rho(r)\varepsilon_{xc}^{hom}\big(p(r)\big)dr \qquad (3.37)$$

where $\varepsilon_{xc}{}^{hom}$ is the exchange-correlation energy density related to the uniform electron gas per particle.

Despite being derived from a comparison to the uniform electron gas, the LDA is successful in analysing inhomogeneous systems that differ from the uniform electron gas. This success is caused by the underestimation of the correlation energy and concomitant overestimation of the exchange energy that occurs within LDA, which lead to the cancellation of errors. However, the use of LDA in simulations for isolated systems (e.g., molecules) and systems with very inhomogeneous distributions leads to accuracy issues. Additionally, LDA-

based calculations generally overestimate binding energies and can generate incorrect predictions for some electronic ground-states too. In such cases, a different approximation should be chosen.

Generalised Gradient Approximation (GGA)

The GGA is an expansion of the LDA that includes a dependence on the gradient of the density. GGA can be used to obtain the exchange-correlation energy according to Equation 3.38.

$$E_{xc}^{GGA}[\rho] = \int \rho(r)\varepsilon_{xc}^{GGA}\big(\rho(r), \nabla\rho(r)\big)dr \qquad (3.38)$$

Various types of GGA functionals are available, with the most popular type for solid-state applications being the Perdew-Burke-Ernzerhof (PBE) functional[163]. Compared to the LDA, the GGA has been able to successfully predict properties such as binding energies and crystal structures more accurately. However, as pure DFT approximations, both the GGA and the LDA underestimate band gaps. This issue is not exclusive to GGA- and LDA-based calculations and is common to all pure DFT calculations.

Hybrid Functionals

Hybrid functionals are functionals that contain elements of DFT exchange-correlation functions and Hartree-Fock theory. Such functions can be used to correct the band-gap underestimation that occurs within pure DFT calculations and, therefore, are pertinent in cases when the analysis of band gaps is relevant for an investigation. Additionally, binding energies

and geometries have also been more accurately predicted by hybrid functional compared to GGA-based results. However, the computational costs associated with hybrid functional-based calculations still limits the size of the systems that can be studied using these functionals. Examples hybrid functionals include the B3LYP functional[164,165], the PBE0[166], and the Heyd–Scuseria–Ernzerhof (HSE) functional[167], with the latter being used in the work presented in this Thesis. The HSE functional is described in Equation 3.39.

$$E_{xc}^{\omega PBEh} = aE_x^{HF,SR}(\omega) + (1-a)E_x^{PBE,SR}(\omega) + E_x^{PBE,LR}(\omega) + E_c^{PBE} \qquad (3.39)$$

where $E_x^{HF,SR}$ is the short-range Hartree-Fock exchange functional, E_c^{PBE} is the PBE correlation function, ω is an adjustable parameter, a represents the mixing parameter and $E_x^{PBE,SR}$ and $E_x^{PBE,LR}$ are the short-range and long-range components of the PBE exchange functional, respectively. Standard values of 0.2 and 0.25 for the ω and mixing parameters are found to generate reasonable results for most systems.

3.6.4 DFT and solids

Calculations aiming to solve the Schrödinger equation tend to analyse the bulk of a system and, consequently, they tend to treat the system as infinite. In order to perform such type of calculation, an infinite number of basis sets would be needed which would lead to extreme computational costs. Periodic boundary conditions can be used to treat the system as a finite crystal and decrease the simulation associated computational costs. To do this, periodic boundary conditions utilising reciprocal space, or k-space, rather than real space are used to describe the system and its lattice properties.

Reciprocal Lattice and k-space

Lattice vectors $\boldsymbol{a}$, $\boldsymbol{b}$, and $\boldsymbol{c}$ are described in reciprocal space as $\boldsymbol{a}^*$, $\boldsymbol{b}^*$, and $\boldsymbol{c}^*$, as shown in Equations 3.40, 3.41, and 3.42.

$$\boldsymbol{a}^* = 2\pi \frac{\boldsymbol{b} \times \boldsymbol{c}}{\boldsymbol{a} \cdot \boldsymbol{b} \times \boldsymbol{c}} \qquad (3.40)$$

$$\boldsymbol{b}^* = 2\pi \frac{\boldsymbol{a} \times \boldsymbol{c}}{\boldsymbol{b} \cdot \boldsymbol{a} \times \boldsymbol{c}} \qquad (3.41)$$

$$\boldsymbol{c}^* = 2\pi \frac{\boldsymbol{a} \times \boldsymbol{b}}{\boldsymbol{c} \cdot \boldsymbol{a} \times \boldsymbol{b}} \qquad (3.42)$$

A unit cell in real space that displays lattice vectors equal to $\boldsymbol{a}$, $\boldsymbol{b}$, and **c** can be defined in the reciprocal space as the Brillouin zone. This stands as a critical concept in the analysis of periodic systems, which is described below by the Bloch's Theorem[168], as a complete description of the wavefunction arises from its volume.

Bloch's Theorem

Bloch's Theorem states that the wavefunction of an electron (i) within a periodic field can be defined as shown in Equation 3.43.

$$\psi_i(\boldsymbol{r}) = e^{i\boldsymbol{k}\boldsymbol{r}} f_i(\boldsymbol{r}) \qquad (3.43)$$

where e is Euler's number, $\boldsymbol{r}$ is related to the position vector, f is a periodic function with the same periodicity as the crystal and $\boldsymbol{k}$ represents a wavevector in the Brillouin zone that can control the direction and the frequency of the wave-based term.

The periodic function can be further described as shown in Equation 3.44.

$$f_i(\boldsymbol{r}) = \sum_{\boldsymbol{G}} c_{i,\boldsymbol{G}} e^{i\boldsymbol{G}.\boldsymbol{r}} \qquad (3.44)$$

where $c_{i,\boldsymbol{G}}$ are the plane wave expansion coefficients and $e^{i\boldsymbol{G}.\boldsymbol{r}}$ is a basis set of discrete plane waves with $\boldsymbol{G}$ standing as wavevectors that are related to all translations to symmetrically identical lattice points.

The plane wave description of the wavefunction can be generated from the combination of Equations 3.43 and 3.44, as shown in Equation 3.45.

$$\psi_i(\boldsymbol{r}) = \sum_{\boldsymbol{G}} c_{i,\boldsymbol{k}+\boldsymbol{G}} e^{i(\boldsymbol{k}+\boldsymbol{G}.\boldsymbol{r})} \qquad (3.45)$$

The solution is defined by the coefficient $c_{i,\mathbf{k}+\mathbf{G}}$. This lowers the number of one-electron wavefunctions from infinite to just the electrons in the unit cell, which makes the calculation feasible. However, there are an infinite number of k-points in the reciprocal space and further approximations, covered in the next section, will be needed to facilitate this calculation.

Plane waves

Choosing the plane wave basis set is a critical decision as it impacts both the results accuracy and the associated computational costs. Two approximations are used in order to facilitate this calculation. First, plane waves endowed with large values of |G| display higher kinetic energies and, consequently, are deemed to have a lower contribution to the ground-state wavefunction. Therefore, a cutoff for the value of |G| (i.e., an energy cutoff) is applied to Equation 3.45. Plane waves that display |G| values higher than the stipulated cutoff are deemed insignificant to ψi(r) and are not analysed. The second approximation states that small changes in k will have a low impact on ψ, since ψ is a continuous function of k. Therefore, a finite number of points in k-space, known as k-points, can be used to provide a suitable description of k-space[169].

Using a suitable set of k-points is crucial for generating an appropriate representation of the investigated system and thus an ill-fated choice of k-points could lead to non-accurate results. The Monkhorst-Pack (MP) selection scheme[170] samples the Brillouin zone via the definition of a homogenous k-point mesh. Due to the symmetric equivalence existent between many of the k-points within the grid, the use of the MP selection scheme reduces the associated computational costs as it is only necessary to calculate the wavefunction at non-equivalent k-points.

In practice, the ground-state properties of a material can be used to check the convergence of both approximations. By varying the energy cutoff and the k-point mesh, it is possible to calculate the effects that such variations have on the investigated properties. When alterations in the cutoff and in the k-point mesh are showed to have an insignificant impact on the calculations, then convergence is deemed achieved. The lowest values of cutoff and k-point mesh that allow for convergence to be acquired are typically used to represent the investigate the system as these would be the values that will represent the system with the lowest associated computational costs.

Pseudopotentials

The potential and the electron wavefunction suffer from significant variation near the nuclei of an atom or an ion. A suitable representation of the fine spatial detail related to the wavefunctions at close distances from the nuclei would require several plane waves, which would lead to high computational costs. Nevertheless, core electrons are not usually involved in chemical bonding and, consequently, they are deemed significantly fixed. Therefore, it is possible to divide the analysis of core and valence electrons in two separate regions through the use of pseudopotentials.

The pseudopotential describes the core potential via a smooth function and can be reproduced by using a reduced set of plane waves, which lowers the associated computational costs. This approximation is only valid within a certain cutoff radius. Although the only exact representation involved in this approximation is that of the valence region, this method has shown to be adequate for the analysis of many ground-state properties.

The smoothness of the pseudopotential function and the size of the cutoff radius used can be described by the "softness" of the pseudopotential, with softer pseudopotentials needing fewer plane waves to be reproduced. However, as softer pseudopotentials also display larger cutoff radius, the use of pseudopotentials that are too soft could lead to issues as the cutoff radius could be excessive and cause an inaccurate representation of the atom. Therefore, a balance needs to be found between the computational time available and the accuracy of the representation needed.

Projector Augmented Waves (PAWs)

As discussed in the previous section, the pseudopotential method is a successful approximation for the wavefunction. However, such a method does not provide a strategy for

the calculation of the exact true wavefunction. The PAW method[171] allows for the efficient calculation of the all-electron wavefunction. This method utilises a linear transformation term (T) to change the smooth pseudopotential function ($|\Psi\rangle$) to a true wavefunction ($|\widetilde{\Psi}\rangle$), as shown in Equation 3.46.

$$|\psi\rangle = T\big|\tilde{\psi}\rangle \qquad (3.46)$$

The transformation term is described in Equation 3.47, where R is the atomic positions and T_R represents an operator that works solely within spheres centred on the nucleus, which are contained by the cutoff distance around each atom. It is important that such a region, known as the augmentation region, is delimited by a suitable cutoff distance to avoid overlapping. In this way, T has a form where the wavefunction and the pseudopotential wavefunction only differ when concerning the core region and within the cutoff distance, with the valence region remaining the same for both wavefunctions.

$$T = 1 + \sum_{R} T_R \qquad (3.47)$$

The pseudopotential wavefunction can be expanded within each sphere, as shown in Equation 3.48, where $\widetilde{\Phi}$ stands for pseudo-partial waves and c_i represents unknown expansion coefficients. As the pseudo-wavefunctions, the partial waves also remain the same outside the augmentation regions.

$$|\tilde{\psi}\rangle = \sum_i |\widetilde{\Phi}_i\rangle c_i \qquad (3.48)$$

The expansion coefficients can be described by Equation 3.49, where $\tilde{p}$ are projector functions. The biorthogonality condition show in Equation 3.50 must be respected by the projector functions.

$$c_i = \langle \widetilde{p}_i | \tilde{\psi} \rangle \qquad (3.49)$$

$$\sum_i |\widetilde{\Phi i}\rangle\langle \widetilde{p} i| = 1 \qquad (3.50)$$

Considering that T_R is approximately null outside of the augmentation regions, it is possible to describe the transformation operator following Equation 3.51.

$$T = 1 + \sum_i (|\Phi_i\rangle - |\langle \widetilde{\Phi i} \rangle)\langle \widetilde{p}_i| \qquad (3.51)$$

Consequently, the transformation operator can be used for the all-electron Kohn-Sham wavefunction:

$$|\psi\rangle = |\tilde{\psi}\rangle - \sum_i |\widetilde{\Phi_i}\rangle\langle\widetilde{p_i}|\widetilde{\psi}\rangle + \sum_i |\Phi_i\rangle\langle\widetilde{p_i}|\,\tilde{\psi}\rangle \qquad (3.52)$$

where Φ_i represents the all-electron partial waves. Consequently, the PAW method is separated into three components: the all-electron and pseudo-partial waves and the projector functions. Therefore, the direct calculation of the wavefunction is allowed as well as the calculations of any physical properties. As the properties of the core electrons are still approximated and those of the valence electrons are treated with smooth pseudo wavefunctions, the computational costs are still manageable. In the DFT work presented in this Thesis, the interactions between core and valence electrons were described by the PAW method.

3.7 Surface Calculations

A surface is formed at the point where the solid system ends and is subsequently followed by another region (e.g., liquid, gas or vacuum regions). A surface can be considered as a perfect symmetrical bulk system that was "cut" alongside a chosen crystallographic plane. The surface is periodic in all dimensions except in the dimension that is normal to itself.

In practice, one of the methods available for simulating surfaces is based on the production of "slabs". An example slab, along with a vacuum region, are shown in Figure 3.7. The slab is a material with finite width and the lattice vector corresponding to its normal can be altered to control the region (e.g., a vacuum region) between different slabs. However, as the computational costs rises along with the size of the vacuum region, it is important that a balance is sought when concerning the choice of the vacuum size. Convergence tests are pertinent in this context, during which the vacuum size can be altered until its impact on the calculated surface energies remains constant (i.e., convergence is achieved).

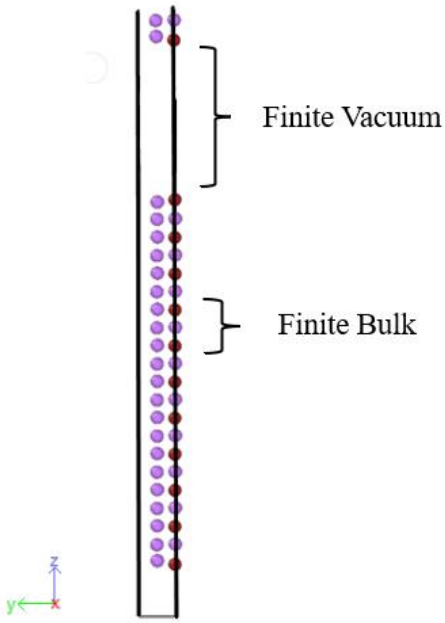

Figure 3.7. Schematic representation of an arbitrary “slab” model. Black lines represent periodic boundaries.

The validity of the slab model depends on the distance between the slabs and their thickness. The slabs must be sufficiently large so that their middle regions can be considered approximately as bulk-like and the distance between the slabs must be large enough they cannot significantly interact with each other.[172] The energy associated with the formation of a charge neutral and stoichiometric slab is shown in Equation 3.53.

$$\gamma_S = \frac{E_{slab} - NE_{bulk}}{2A} \qquad (3.53)$$

where E_{slab} is the energy of the slab model that is constituted by N units of the bulk system, E_{bulk} is the energy of the bulk system, A represents the cross-sectional area of the slab and the factor 2 accounts for the equivalent surfaces in the system.

In cases where the surface stoichiometry needs to be removed to maintain the surfaces symmetry, the surface energy can be calculated following Equation 3.54.

$$E_{surf} = \frac{1}{2S}[E_{slab} - NE_{bulk} - M\mu_i] \qquad (3.54)$$

where E_{slab} and E_{bulk} are the calculated free energies of the slab and the bulk unit cell, respectively, with N representing the number of bulk unit cells contained in the slab structure. The surface area is represented by S and μ_i is the chemical potential of species i that exceeds the stoichiometric expectancy in the slab. M is the number of species units that needs to be removed.

3.8 Nudged Elastic Band Calculations

The calculation of the energy barriers between different states allowed for in a particle system can provide important information about that system's dynamics. The minimum energy path (MEP) for such transitions can be found by applying different search methods. Such methods can be divided into single-ended search methods, where only one starting state, local minimum or specific state is known, and double-ended search methods, where both the initial and final states are known. Examples of single-ended search methods include the dimer method[173] and the activation-relaxation technique[174,175], while the string[176,177] and NEB

methods[178,179] are examples of double-ended search methods. The energy pathways studied in the work presented in this Thesis were explored via the NEB method.

The NEB method can be used to calculate the energy barriers between two states and explore the MEP. This method is based on the creation of a number n of images that represent the intermediate stages between the initial and final states, resulting in *n*-1 vectors joining each point. The intermediate images can be generated either by linear interpolation or via the image dependent pair potential (IDPP) method[180]. The IDPP method can be more efficient in cases, for example, where the linear interpolation is hindered by unfavourable paths or when atoms are exceedingly close to each other. The initial images are created via a simple pair potential that solely accounts for the atomic distances, as shown in Equation 3.55.

$$d_{ij}^{k} = d_{ij}^{\alpha} + k\left(d_{ij}^{\beta} - d_{ij}^{\alpha}\right)/n, \;\; k = 1, \dots, n-1 \qquad (3.55)$$

with:

$$d_{ij} = \sqrt{\sum_{\sigma} (r_{i,\sigma} - r_{j,\sigma})^2} \qquad (3.56)$$

where $r_{i,\sigma}$ is the coordinate of atom i in the σ direction. The σ direction is equal to x, y, and z, and represents the distance between the atoms i and j. The term k stands for the index of the image and α and β are the initial and final states, respectively.

A function for the potential energy for each image can be generated, as shown in Equation 3.57.

$$V_k^{IDPP}(r) = \sum_i^N \sum_{j>i}^N \omega(d_{ij})(d_{ij}^k - d_{ij})^2 \qquad (3.57)$$

With the weight function (ω) being:

$$\omega(d) = \frac{1}{d^4} \qquad (3.58)$$

where N is number of atoms in the system. This is minimised using the NEB method. Once minimised, the NEB method is applied to the original potential energy functions.

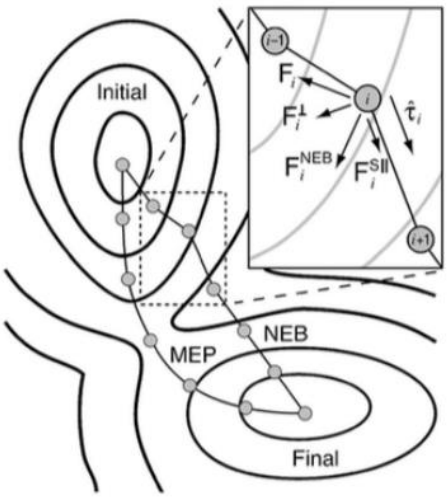

Figure 3.8. Schematic representation of NEB method and a MEP. Each image possesses a real force $\mathbf{F}_i$ and a newly generated NEB force $\mathbf{F}_i^{NEB}$.[181]

The vector decomposition process that follows is the same for NEB calculations performed via linear interpolation or IDPP techniques. The real force vector ($\mathbf{F}_i$) will be decomposed at each image i in two components: a parallel force ($\mathbf{F}_i^{\parallel}$) and a perpendicular force ($\mathbf{F}_i^{\perp}$) with respect to the tangent vector ($\boldsymbol{\tau}_i$) (Figure 3.8).

A spring interaction is utilised to manage the spacings between the adjacent images. Equation 3.59 describes the spring force.

$$\boldsymbol{F}_i^{s\parallel} = \kappa(|\boldsymbol{R}_{i+1} - \boldsymbol{R}_i| - |\boldsymbol{R}_i - \boldsymbol{R}_{i-1}|)\boldsymbol{\tau}_i \qquad (3.59)$$

where κ is the spring constant and $\boldsymbol{R}_i$ represents the coordinates of the particles.

The definition of the tangent of image i is given in Equation 3.60.

$$\boldsymbol{\tau}_i = \begin{cases} \boldsymbol{R}_{i+1} - \boldsymbol{R}_i & \text{if } V_{i-1} \le V_i \le V_{i+1} \\ \boldsymbol{R}_i - \boldsymbol{R}_{i-1} & \text{if } V_{i+1} \le V_i \le V_{i-1} \\ (\boldsymbol{R}_{i+1} - \boldsymbol{R}_i)\Delta V_i^{max} + (\boldsymbol{R}_i - \boldsymbol{R}_{i-1})\Delta V_i^{min} & \text{if } V_i \le V_{i-1} \le V_{i+1} \\ (\boldsymbol{R}_{i+1} - \boldsymbol{R}_i)\Delta V_i^{min} + (\boldsymbol{R}_i - \boldsymbol{R}_{i-1})\Delta V_i^{max} & \text{if } V_i \le V_{i+1} \le V_{i-1} \end{cases} \qquad (3.60)$$

where:

$$\Delta V_i^{max} = \max\left(|V_{i+1} - V_i|, |V_{i-1} - V_i|\right) \qquad (3.61)$$

$$\Delta V_i^{min} = \min\left(|V_{i+1} - V_i|, |V_{i-1} - V_i|\right) \qquad (3.62)$$

The total force is described as the summation of the perpendicular component and the spring force, as shown in Equation 3.63.

$$\boldsymbol{F}_i^{NEB} = \boldsymbol{F}_i^{\perp} + \boldsymbol{F}_i^{s||} \qquad (3.63)$$

The total force on each image can be then iteratively minimised via the conjugate gradient method until the tangential force on each image converges (i.e., the images have converged to the MEP).

The saddle point (SP) can be acquired more accurately via the climbing image NEB, which is used after a plethora of relaxation steps. The image that displays the highest energy can move up the potential energy surface towards the SP as the spring force is deemed insignificant.

$$\boldsymbol{F}_{imax} = \boldsymbol{F}_i - 2\boldsymbol{F}_{i\tau} \qquad (3.64)$$

3.9 Software and Computational Resources

Different software and hardware were needed to carry out the empirical force field-based atomistic, MD and DFT calculations presented in this Thesis. Empirical force field-based atomistic simulations were run using the General Utility Lattice Program (GULP)[145] via the Newcastle University Aidan Unix time sharing system. The MD calculations were run using the Large-scale Atomic/Molecular Massively Parallel Simulator (LAMMPS)[146] via the

Newcastle University Rocket High Performance Computing service. The DFT calculations were run on the UK's high performance computing facility ARCHER2 using the Vienna Ab initio Simulation Package (VASP)[147,148].

Chapter 4 Defect Chemistry and Ion Transport in Low-Dimensional-Networked Li-Rich Anti-Perovskites

4.1 Introduction

The heart of the solid-state battery (SSB) technology lies in the replacement of liquid electrolytes by solid counterparts, resulting in potential critical advantages that could lead to lighter, safer, and more durable batteries. Consequently, research concern in assessing different solid electrolyte (SE) families has flourished in recent years.

Li-rich anti-perovskites have the typical formula of Li_3OX (X = Cl, Br, I or a mixture of halides) and are attracting significant attention as a SE family endowed with promising features, including good Li-ion conductivity, stability against Li metal, wide electrochemical windows and low-cost synthesis.[7,62–65] Anti-perovskites also possess a remarkably versatile structure that allows for easy structural manipulation, enabling the tailoring of performance, properties and ion transport mechanisms, as well as providing substantial chemical versatility and diversity.[66–70]

The accurate measurement of the Li-ion conductivities and activation energies in anti-perovskite SEs has gained fresh prominence in the context of recent findings. While an early study by Zhao and Daemen[62] on Li_3OCl, Li_3OBr and $Li_3OCl_{0.5}Br_{0.5}$ reported Li-ion conductivities of $>10^{-3}$ S cm^{-1} at room temperature and activation energies of 0.2–0.3 eV,

more recent works have obtained activation energies of ~0.6 eV and lower conductivities (e.g., 10^{-6} S cm^{-1} at room temperature) for bulk Li_3OCl and Li_3OBr.[63,67,71,93,106,107,109,114,182,183] Several reasons for this disparity, including high grain boundary resistance, unintended doping and the presence of moisture (e.g., Li_2OHCl), have been proposed.[63,66,71,109,114,116,125,126,130,182–185]

Such discrepancies have highlighted the pertinence of atomistic modelling studies in accessing fundamental information on the ion transport mechanisms and defect chemistry present in Li-rich anti-perovskites[70,71,74,94–97,105–107,114,115,186–192], contributing to revealing the underlying processes that cause their intriguing behaviour. In particular, significant efforts have been made to determine the dominant defect types in anti-perovskites and how they affect their ionic diffusion.[69,95,98,105,192] For example, in a density functional theory (DFT) study of Li_3OCl, Li_3OBr and $Li_3OCl_{0.5}Br_{0.5}$, Emly *et al.*[95] investigated a three-ion hop mechanism that involved Li interstitial dumbbells that promoted a very low Li-ion migration barrier of ~0.17 eV for all systems, indicating a concerted Li-ion motion that is seen in several other SEs.[93,96–99] However, the high formation energies of Li interstitials found for these structures suggested that this mechanism was not responsible for the high conductivities found. Mouta *et al.*[105] also found a low enthalpy of 0.13 eV for interstitial migration in Li_3OCl *via* classical atomistic quasi-static calculations. However, their explorations deemed vacancy migration, with a vacancy migration enthalpy of 0.30 eV, to be the pertinent transport mechanism in the system due to the concentration of Li vacancies being six orders of magnitude greater than the one found for Li interstitials. The dominance of vacancy hopping mechanisms from interstitial diffusion was also reported by Dawson *et al.*[71] in a study that explored the defect chemistry of a wide range of $Li_{3-x}Na_xOCl_{1-y}Br_y$ anti-perovskites.

In addition to the well-reported three-dimensional-networked (DN) anti-perovskites discussed above, low-DN Cl-based anti-perovskites (i.e., 2DN Li_4OCl_2, 1DN Li_5OCl_3 and 0DN Li_6OCl_4) have recently been introduced by Lu *et al.*[60] based on advances in low-DN

hybrid perovskites for photovoltaic applications.[193] Low-DN anti-perovskites are formed when the dimensionality of the interconnected BX_6 octahedra is lowered, as illustrated in Fig 4.1. Consequently, the BX_6 octahedra are connected along planes separated by LiX (X = Cl or Br) layers in the 2DN anti-perovskite (space group I4/mmm). Analogously, a 1 DN anti-perovskite (space group Pnam) is formed if a 2DN anti-perovskite is perpendicularly sliced to the inorganic sheets, leading the octahedra to be connected only along one axis. 0DN (space group $R\bar{3}c$) anti-perovskites are formed by further slicing a 1DN anti-perovskite to form isolated octahedra. Following this nomenclature, the traditional X_3OA (space group $Pm\bar{3}m$) anti-perovskite is a 3DN anti-perovskite.

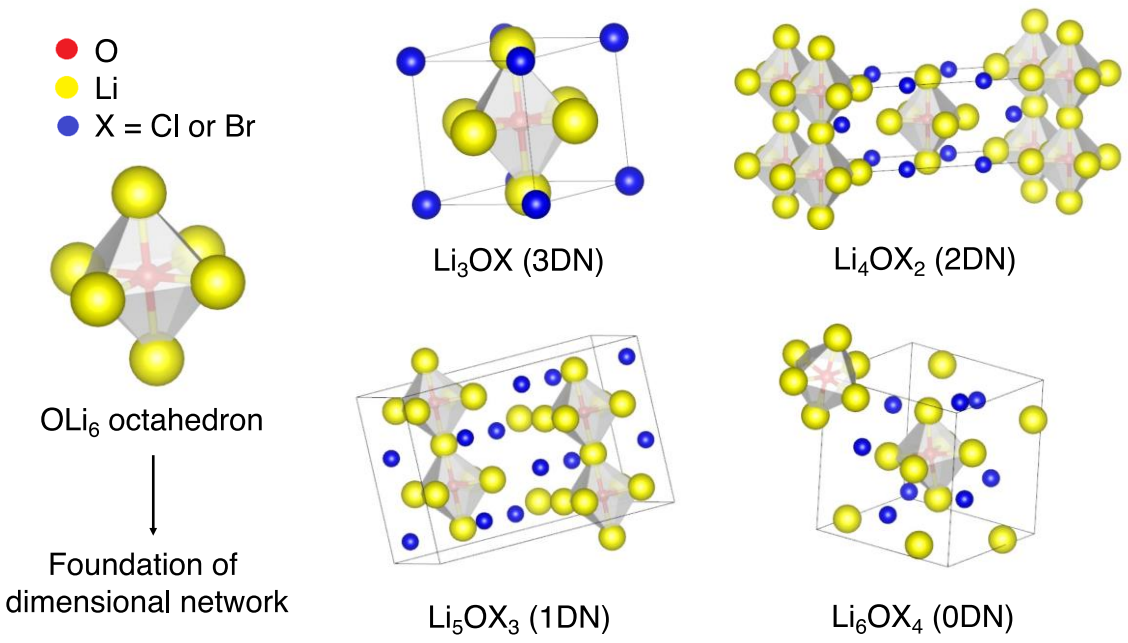

Figure 4.1. Schematic illustration of OLi_6 octahedron as the foundation of the cation network and crystal structures of Li_xOX_{x-2} (X = Cl or Br, x = 3-6) anti-perovskites.

In the same report that introduced low-DN Cl-based anti-perovskites, Lu *et al.*[60] used DFT and *ab initio* molecular dynamics (AIMD) to analyse low-DN anti-perovskites with

formulae Li_xOCl_{x-2} (x = 3–6) and found that the Li-ion conductivity increases with decreasing dimensionality in these systems due to the decreased ion migration bottlenecks and the softening of the rotation modes of the OLi_6 octahedra.

In terms of synthesising low-DN anti-perovskites, although the synthesis of 1DN and 0DN anti-perovskites has yet to be reported, recent progress in synthesising 2DN anti-perovskites has been made. Zhu *et al.*[194] successfully synthesised a mixture of 2DN $Li_7O_2Br_3$ and 3DN Li_3OBr anti-perovskites, which displayed improved ionic conductivity (5×10^{-5} S cm^{-1}) compared to Li_3OBr alone (10^{-6} S cm^{-1}), suggesting the possibility of low-DN anti-perovskites having higher ionic conductivities than their 3DN counterparts. Wakazaki *et al.*[195] recently synthesised Li_4OBr_2 for the first time by high-pressure synthesis. Progress has also been made for the synthesis of 2DN Na-based low-DN anti-perovskites, with Zhu *et al.*[189] reporting the synthesis of Na_4OI_2 (first reported by Sabrowsky *et al.*[196] via a solid-state reaction.

Despite the considerable body of work focused on anti-perovskites, many of the elementary processes that explain their behaviour are still misunderstood. For low-DN anti-perovskites, the ion transport mechanisms and defect chemistry are yet to be fully explored and understood. Considering the pivotal role that ionic diffusion and structural disorder have on the ion transport behaviour of anti-perovskites, there is a heightened need for studies that investigate these factors in these materials.

In this Chapter, the energetics of defect formation, stability, and ionic transport in a range of Li_xOX_{x-2} (X = Cl or Br; x = 3–6) anti-perovskites with zero- to three-dimensional-networked structures are investigated via atomistic simulations. The performed calculations found that the targeted systems generally possess Li–halide Schottky defect pairs as dominant native defects. The results achieved reveal that defect formation is generally energetically preferable in the Li_xOCl_{x-2} series compared to the equivalent structures in the Li_xOBr_{x-2} set.

Moreover, the molecular dynamics simulations results obtained reveal the strong relationship between dimensionality and Li-ion dynamics in the targeted systems, namely, increasing Li-ion diffusion and decreasing activation energy with reduced dimensionality. Enhanced Li-ion diffusion is found for the low-dimensional-networked Br-based materials (4.81×10^{-9} and 6.08×10^{-9} $cm^2\ s^{-1}$ for Li_5OBr_3 and Li_6OBr_4 at 300 K, respectively) compared to their Cl-based counterparts (9.85×10^{-10} and 2.06×10^{-9} $cm^2\ s^{-1}$ for Li_5OCl_3 and Li_6OCl_4 at 300 K, respectively), showing the impact of lattice polarisability in these soft and unstable materials.

4.2 Computational Methods

The procedures followed to design the defect and classical molecular dynamics (MD) calculations performed in this work are based on well-established protocols that have been widely and successfully used to investigate defect energetics and ion transport mechanisms in a plethora of battery materials.[104,113,154,197–199]

4.2.1 Structural details

The structural details (e.g., atomic sites and lattice parameters) for the Li_3OCl system were obtained from the Materials Project repository[200], while the details for the other targeted anti-perovskites were acquired from the publication by Lu *et al*.[60] The structural details for Li_2O, LiCl and LiBr were necessary for the purpose of calculating the partial Schottky defect formation energies and were also obtained from the Materials Project repository. A comparison of the calculated and available experimental lattice parameters is given in Table A1.1 in Appendix A.1. The input structures used for the optimisations are also available in Appendix A.1.

4.2.2 Potential model

The Buckingham potential model of Mouta *et al.*[105], with refinements from Dawson *et al.*[71], was utilised in this work for all the calculations. This model has previously been used to successfully describe Li-rich anti-perovskites for the study of their defect chemistry and ion transport mechanisms. Formal valence charges were used for all ions. The long-range ionic interactions were modelled using Coulombic terms. The shell model of Dick and Overhauser[152] was used to account for ionic polarisation, as described in Section 3.2.2.

4.2.3 Defect formation energy calculations

A diverse range of defect types, namely, full Schottky, alkali-halide partial Schottky, Li_2O partial Schottky, antisite and lithium, oxygen and halide Frenkel defects, were explored in the targeted anti-perovskite systems via the General Utility Lattice Program (GULP)[145] with the Mott–Littleton approximation[153], as described in Section 3.4. For the calculations performed in this Chapter, the radii of 13 and 21 Å were used for regions I and IIa, respectively.

4.2.4 Molecular dynamics calculations

All MD simulations were performed using the Large-scale Atomic/Molecular Massively Parallel Simulator (LAMMPS) code[146]. An example LAMMPS input file can be seen in Appendix A.2. Long MD runs of 10 ns were completed utilising a time step of 2 fs with supercells of 10×10×10. Long-range Li-ion diffusion was acquired by randomly removing ~2% of Li and halide ions from the systems. The constant-temperature, constant-pressure ensemble (NPT) was used in all simulations with a Nosé–Hoover thermostat[158]. The MD simulations were run for a temperature range of 500–800 K at intervals of 100 K for all

structures and for an additional temperature range of 200–400 K at intervals of 50 K for the 1DN and 0DN systems. Self-diffusion data for the Li ions were acquired from the mean-squared displacement (MSD), as described in Section 3.5.4. The calculation of activation energies for the targeted systems was performed by using an Arrhenius plot of MSD data collected at the different temperatures used for the MD simulations, as described in Section 3.5.4.

4.3 Results

4.3.1 Structures, stability, and intrinsic defect formation

First, to assess the stability of the target low-DN anti-perovskite systems, the calculation of their formation energies was carried out with respect to their starting oxides (i.e., Li_2O and LiX (X = Cl or Br)). For the Cl-based systems, the values obtained were −0.60, −0.63, −0.44 and −0.08 eV for the 3DN, 2DN, 1DN and 0DN structures, respectively. These energies are in good agreement with the decomposition energies calculated by Lu *et al.*[60] using DFT for the same systems, i.e., 0DN Li_6OCl_4 is predicted to be the least thermodynamically stable and 2DN Li_4OCl_2 is predicted to be the most thermodynamically stable at 0 K. For the Br-based systems, the values acquired were −0.93, −1.06, −0.85 and −0.64 eV for the 3DN, 2DN, 1DN and 0DN structures, respectively. Therefore, the calculations performed suggest that the Br-based materials are more stable than their Cl-based counterparts. A similar finding was also reported by Lu *et al.*[60] for the 3DN and 0DN materials. These results highlight the impact caused by reducing dimensionality on these systems (i.e., a clear reduction in stability).

Different types of intrinsic defects have different features, which can lead them to impact ion transport mechanisms and conductivity within a material differently. Therefore,

the study of intrinsic defect energetics can provide a wealth of information, not only regarding the defect chemistry of a system itself but also about its pertinent ion transport mechanisms.

In this Chapter, the calculation of the energetics of intrinsic Schottky, Frenkel, and antisite defects in a wide range of Li_xOX_{x-2} (X = Cl or Br; x = 3–6) anti-perovskites with 3DN to 0DN structures is performed. All the defect types explored in this Chapter are displayed below in Kröger–Vink notation for the Br-based materials (equivalent equations for the Cl-based materials can be acquired by simply replacing Br with Cl):

Li Frenkel:

$$Li_{Li}^{x} \longrightarrow V_{Li}^{/} + Li_{i}^{\bullet} \qquad (4.1)$$

O Frenkel:

$$O_{O}^{x} \longrightarrow V_{O}^{\bullet\bullet} + O_{i}^{//} \qquad (4.2)$$

Br Frenkel:

$$Br_{Br}^{x} \longrightarrow V_{Br}^{\bullet} + Br_{i}^{/} \qquad (4.3)$$

Antisite:

$$O_{O}^{x} + Br_{Br}^{x} \longrightarrow O_{Br}^{x} + Br_{O}^{x} \qquad (4.4)$$

Full Schottky:

$$3Li_{Li}^{x} + O_{O}^{x} + Br_{Br}^{x} \longrightarrow 3V_{Li}^{/} + V_{O}^{\bullet\bullet} + V_{Br}^{\bullet} + Li_3OBr \qquad (4.5)$$

Li_2O Partial Schottky:

$$2Li_{Li}^{x} + O_{O}^{x} \longrightarrow 2V_{Li}^{/} + V_{O}^{\bullet\bullet} + Li_2O \qquad (4.6)$$

Li-halide Partial Schottky:

$$Li_{Li}^{x} + Br_{Br}^{x} \longrightarrow V_{Li}^{/} + V_{Br}^{\bullet} + LiBr \qquad (4.7)$$

The calculated formation energies for these defect types in the targeted systems are displayed in Figure 4.2. The calculated formation energies are also given in Table A3.1 in Appendix A.3. Given that a lower defect formation energy indicates its more energetically

favourable formation, the results in Figure 2 reveal key information regarding the concentration of intrinsic defects in the investigated systems and their potential role in ionic diffusion.

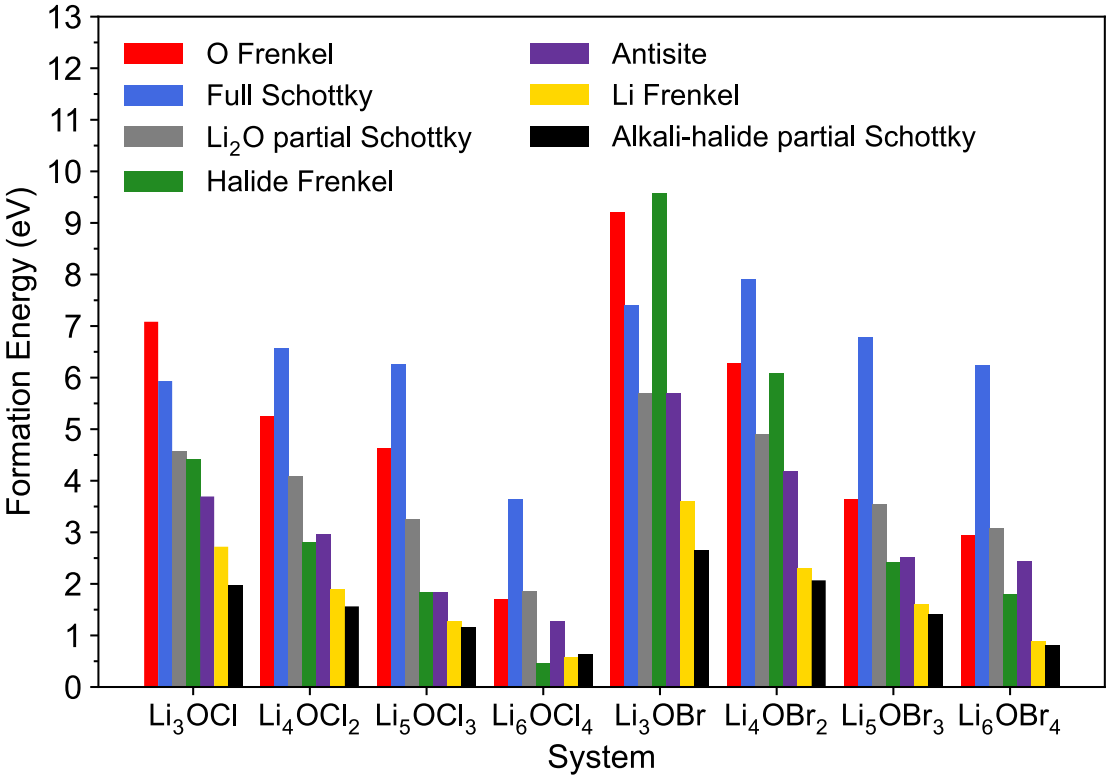

Figure 4.2. Calculated formation energies for Schottky, Frenkel, and antisite defects in Li_xOX_{x-2} (X = Cl or Br; x = 3–6) anti-perovskites.

First, the results show that the formation of almost all defect types in both the Cl- and Br-based systems investigated becomes energetically more favourable when the dimensions are reduced for the 3DN to 0DN materials, with the only exception being the full Schottky defect pairs. This trend is in accordance with previous literature findings for the Cl-based materials.[60] Additionally, the calculations indicate that the formation of the great majority of

defect types is more energetically favourable in Cl-based systems if compared to their equivalent Br-containing structures. This relationship found between defect formation energy and the nature of the halide contained in a system is in agreement with previous calculations results reported for Li_3OCl, Li_2NaOCl and $LiNa_2OCl$ and their Br-based counterparts.[71] This potential for higher defect concentrations in their structures suggest that systems with lower dimensions and with Cl instead of Br as their chosen halide can potentially display enhanced ionic transport and conductivity, albeit with a concomitant reduction in stability.

The comparison of the results across the different halide sets also shows that the concentrations of halide Frenkel defects in the 3DN and 2DN Br-based systems are expected to be significantly lower than those for their counterparts in the Cl set based on the calculated formation energies. Moreover, whereas almost all these systems are predicted to present Li–halide Schottky defect pairs as dominant defects, which aligns with previous literature reports for Li_3OCl[71], Cl interstitials are the predicted dominant type of defect in Li_6OCl_4. This result suggests that Li_6OCl_4 may present interstitial diffusion as the main ion transport mechanism and not a Li vacancy hopping mechanism, contrary to the other anti-perovskites explored in this work, as well as to what has been predicted for this system in the literature previously[60]. Frenkel-type defects have been reported to be more mobile in anti-perovskites and other important solid electrolytes and present lower migration barriers than other types of defects[91,95,102,105], which could potentially lead to more favourable ion transport mechanisms in systems possessing higher concentrations of Frenkel-type defects. Therefore, our calculations indicate that Li-ion transport and conductivity could be enhanced in Li_6OCl_4 compared to the other targeted structures.

4.3.2 Li-ion transport

To investigate Li-ion diffusion in the targeted anti-perovskite systems, MD calculations for all the chosen structures were carried out with a representative Li–halide

Schottky defect concentration of ~2%. Li–halide Schottky defect pairs were the defect type chosen for the MD calculations as these have been predicted as the dominant defect type for all investigated systems except for Li_6OCl_4, as discussed above.

The self-diffusion coefficients obtained via MSD plots as a function of time along with their corresponding temperatures were used to create the Arrhenius plots in Figure 4.3, which were used to calculate the activation energies for Li-ion conductivity for all systems. Example MSD plots for the Br-based structures at a representative temperature of 700 K are given in Figure A4.1 in Appendix A4.

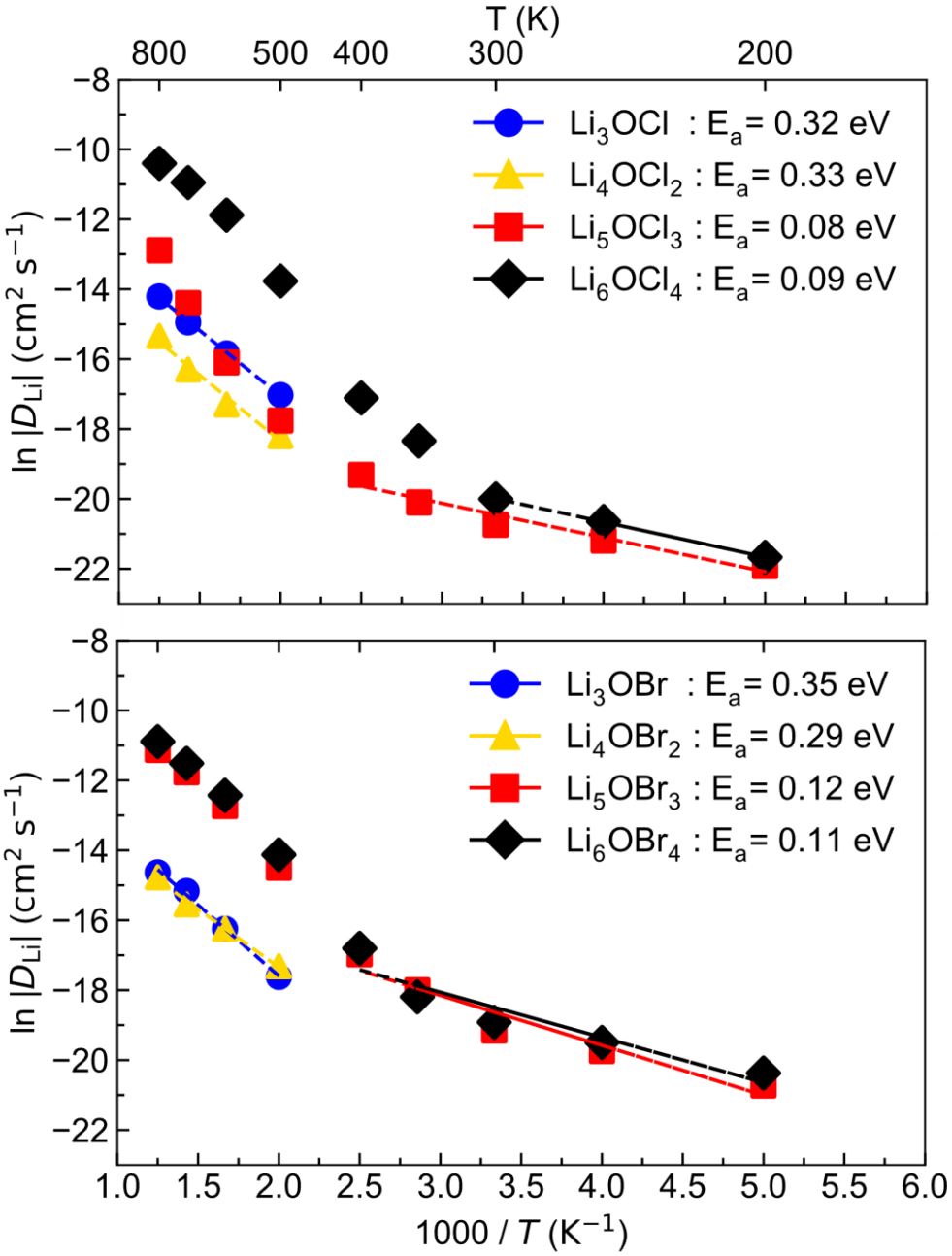

Figure 4.3. Arrhenius plots of Li-ion diffusion for Li_xOX_{x-2} (X = Cl or Br; x = 3–6) anti-perovskites.

The Arrhenius plots in Figure 4.3 show that 1DN and 0DN structures exhibit a strong increase in ionic diffusion above ~300 K, which prevents the data across the whole temperature range for these materials to be described by a single linear fit. To determine the reason for such a significant increase in ionic diffusion at relatively modest temperatures for these materials, all their possible radial distribution functions (RDFs) were computed throughout the MD simulations, as shown in Figure A4.2 in Appendix A4 for 300 K.

There is a clear distinction between the structures of the 3DN (Li_3OX) and 2DN (Li_4OX_2) systems compared to the 1DN (Li_5OX_3) and 0DN (Li_6OX_4) structures. While the high-dimensional-networked systems show distinct peaks for all elemental combinations across the entire range of interatomic distances (r), the low-dimensional-networked systems present remarkably flat RDFs at >5 Å, suggesting a solid-to-liquid transition, i.e., melting. This discrepancy is further verified by the smooth curves for the integrated RDFs of the 1DN and 0DN materials, which indicate an almost linear increase in coordination number with increasing r. In contrast, for the 3DN and 2DN anti-perovskites, regular plateaus are observed where the coordination number remains unchanged with increasing r, thereby highlighting their highly ordered crystalline structures. The effect of temperature on the RDFs in these systems can be seen in Figure 4.4 for the example of Li–Li at 300 and 600 K. These plots display the increase in disorder with decreasing dimensionality in the systems. This trend becomes even clearer at 600 K with the Li–Li RDFs for the 1DN and 0DN material presenting liquid-like behaviour beyond 3 Å.

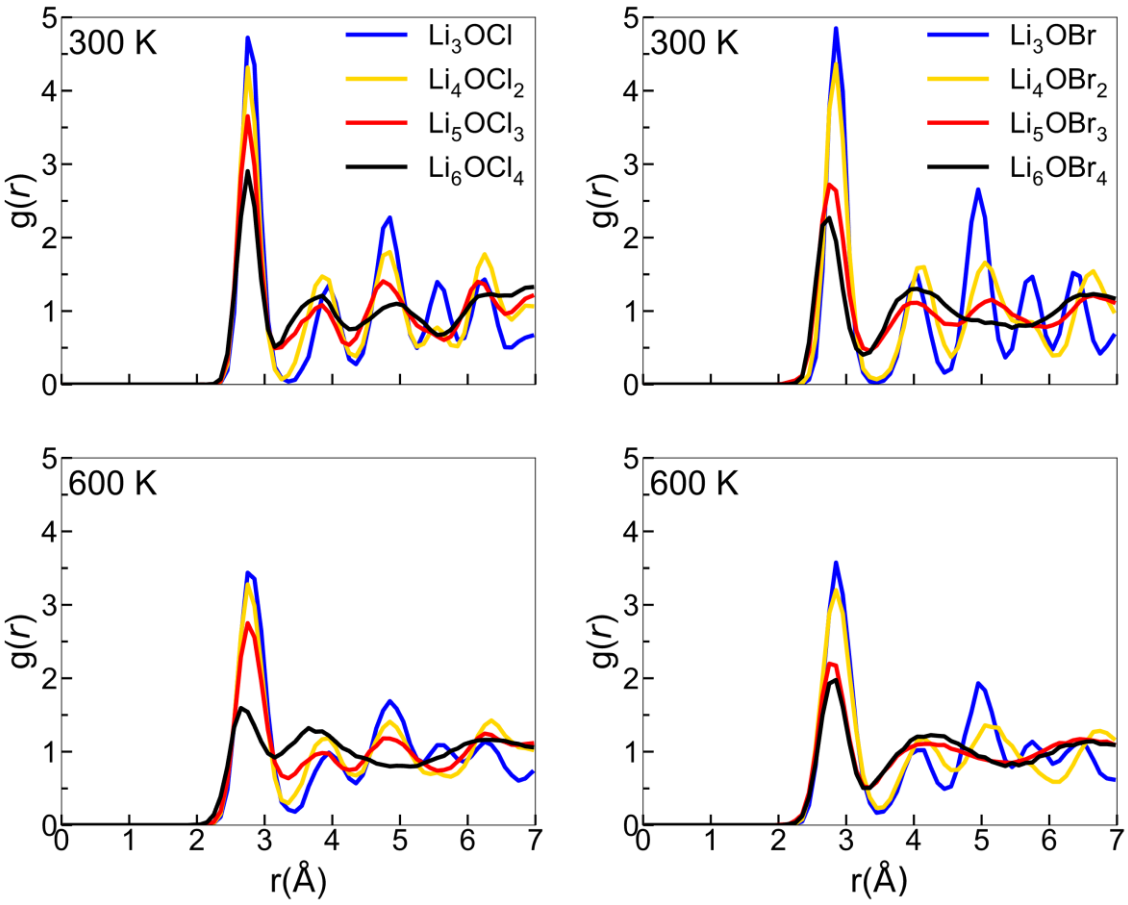

Figure 4.4. Li–Li RDFs for Li_xOX_{x-2} (X = Cl (left) or Br (right); x = 3–6) anti-perovskites at 300 and 600 K.

Although Lu *et al.*[60] reported the melting of Li_5OCl_3 at 800 K in their smaller scale DFT simulations, this is the first time the melting of these 1DN and 0DN anti-perovskites at temperatures as low as 300 K has been reported. This melting at low temperatures indicates instability (and therefore superionic Li-ion conductivity) in the 1DN and 0DN systems, which is reasonable considering the low dimensionality within the structures and the fact that the feasibility of their synthesis is still yet to be confirmed experimentally.

The comparison of the self-diffusion coefficients obtained at 300 K for all systems in Figure 4.5 reveals the clear relationship between Li-ion dynamics and dimensionality in these systems, with Li-ion diffusion increasing and the associated activation energy decreasing with reducing dimensionality. The calculated values and observed trends are in excellent agreement with the DFT results of Lu *et al.*[60] for the Cl-based materials, who attributed their results to the enlarged bottleneck sizes for ionic hopping and the softening of the lattice with reducing dimensionality. Additionally, the calculated activation energies for Li_3OCl (0.32 eV) and Li_3OBr (0.35 eV) are similar to those predicted by Dawson *et al.*[71] (0.29 and 0.31 eV, respectively). It is noteworthy that these calculated values are significantly lower than recently reported experimental results (~0.6 eV)[7], which has been attributed to the high grain boundary resistance in these materials which is not generally considered in atomistic simulations.[66]

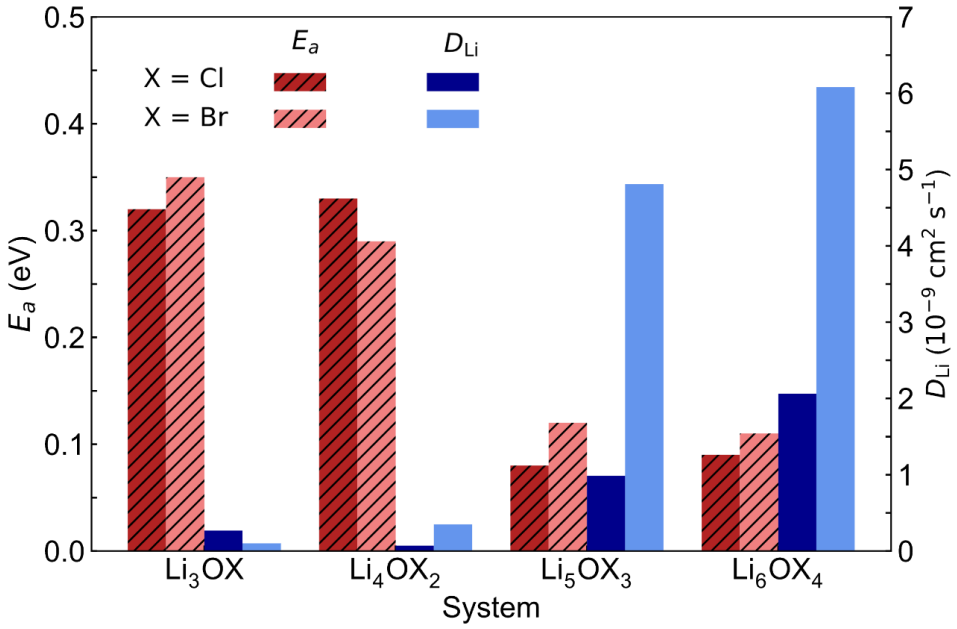

Figure 4.5. Self-diffusion coefficients (D_{Li}) at 300 K and activation energies (E_a) for Li-ion diffusion in Li_xOX_{x-2} (X = Cl or Br; x = 3–6) anti-perovskites.

This work is the first to consider low-dimensional-networked Br-based anti-perovskites. A comparison between the different halide sets reveals the generally greater ionic diffusion for the Br-containing structures, with Li_6OBr_4 displaying a very high self-diffusion coefficient of 6.08×10^{-9} cm^2 s^{-1} that is almost three times the value found for Li_6OCl_4 (2.06×10^{-9} cm^2 s^{-1}). The prevalence of increased ionic diffusion in Br-based structures is also seen for the 2DN and 1DN systems, with Li_4OBr_2 and Li_5OBr_3 showing self-diffusion coefficients of 3.49×10^{-10} and 4.81×10^{-9} cm^2 s^{-1}, respectively, compared to values of 7.07×10^{-11} and 9.85×10^{-10} cm^2 s^{-1} for Li_4OCl_2 and Li_5OCl_3, respectively. The results in Figure 4.5 display that the activation energies for the 3DN and 2DN structures are very similar for both sets of materials, ranging from 0.29 to 0.35 eV. Similar activation energies were also calculated for the 1DN and 0DN systems for both sets, with values ranging from 0.08 to 0.12 eV.

The only exception to the trend of increasing ionic diffusion with decreasing dimensionality is seen for Li_4OCl_2, which displays a self-diffusion coefficient at 300 K of 7.07×10^{-11} cm^2 s^{-1} and an activation energy of 0.33 eV, values that are lower and higher than the respective values for its 3DN counterpart, Li_3OCl (2.68×10^{-10} cm^2 s^{-1} and 0.32 eV, respectively). This behaviour is perhaps expected given that the structure of Li_4OCl_2 contains LiCl layers that represent barriers for Li-ion hopping, thereby resulting in 2D Li-ion diffusion. This is clearly illustrated by the Li-ion diffusion density plots displayed in Figure 4.6 for the Cl-based systems at 300 K (the equivalent plots for the Br-containing structures are given in Figure A4.3 in Appendix A4). As illustrated, while strong isotropic 3D Li-ion diffusion is observed in Li_3OCl, Li_5OCl_3 and Li_6OCl_4, Li-ion diffusion in Li_4OCl_2 is primarily restricted to the perovskite layer.

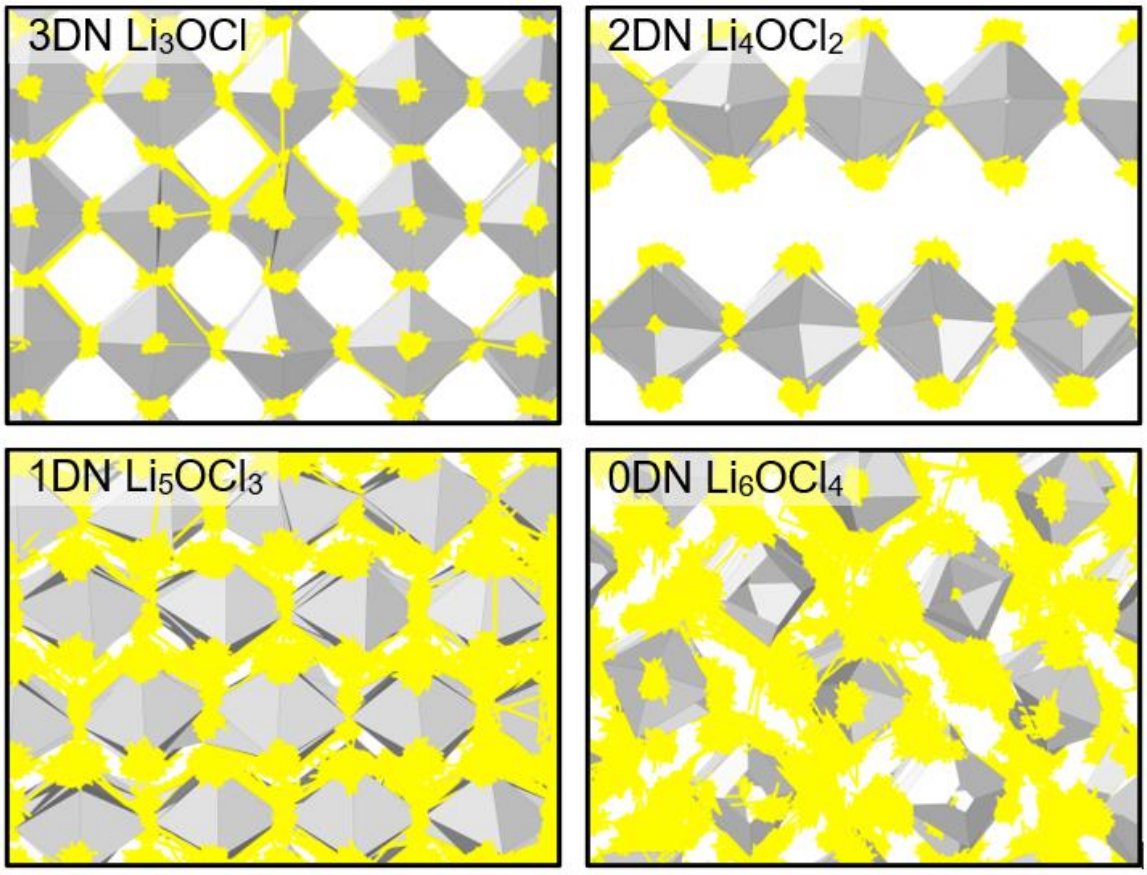

Figure 4.6. Diffusion density plots of Li ions (yellow) overlaid on OLi_6 (grey) octahedra in Li_xOCl_{x-2} (x = 3–6) anti-perovskites at 300 K. Cl ions have been omitted for clarity.

In contrast, 2DN Li_4OBr_2 does not display the same reduction in Li-ion diffusion and increase in activation energy as its counterpart, 2DN Li_4OCl_2, despite having the same structure. As shown by Figure 4.6 and A4.3 (Appendix A4), this discrepancy is not related to the LiX (X = Cl or Br) layer as both materials primarily exhibit 2D Li-ion diffusion and the fact that the width of the LiBr layer is larger than that of the LiCl layer. This therefore suggests another fundamental reason why the 2D, 1D and 0D Br-based materials exhibit higher Li-ion diffusion than their Cl-based counterparts, as visualised in Figure 4.6 and A4.3

(Appendix A4). An explanation could be the increased volume of the Br-based systems; however, it has been shown that the bottlenecks for Li-ion transport in Br-containing anti-perovskites are smaller than in Cl-based anti-perovskites, thereby potentially limiting it.[99]

Another factor to consider is the polarisability of the halide sublattice. It is well known that highly polarisable anion sublattices can have a significant impact on Li-ion conductivity in solid electrolytes by weakening the interaction between the Li ions and surrounding anions[111]. Several studies have shown that substituting the harder Cl ions with softer and more polarisable Br ions can result in significantly enhanced Li-ion transport[111,201,202]. Furthermore, the importance of a soft anion sublattice for fast Li-ion transport in hydride-based anti-perovskites has been revealed[68]. Given the inherent metastability/instability of the low-dimensional-networked materials in this study, it is likely that the presence of Br further weakens the Li–halide interactions, resulting in superionic Li-ion diffusion. This also raises the question of whether iodine doping in these systems could further enhance their ionic conductivity. As proposed previously for thiophosphate solid electrolytes, tailoring of the halide composition could also be an important strategy for tuning the conductivity and stability of anti-perovskite solid electrolytes.

4.4 Conclusion

In this Chapter, the analysis of the energetics of Schottky, Frenkel and antisite defect formation, stability and ion transport mechanisms in a wide range of Li_xOX_{x-2} (X = Cl or Br; x = 3–6) anti-perovskites with 3DN to 0DN structures was carried out. The results obtained show that defect formation for all systems becomes energetically more favourable as the dimensionality of the system is lowered. Moreover, the acquired results find that the formation of the majority of the analysed defect types is more energetically favourable in Cl-based structures rather than in systems containing Br. Apart from Li_6OCl_4, where Cl interstitials are the dominant native defects, the calculations performed show that all targeted

systems are predicted to possess Li–halide Schottky defect pairs as the dominant type of intrinsic disorder.

Based on the MD calculations results obtained and structural analysis performed, the low-temperature melting of the 1DN and 0DN systems at temperatures as low as 300 K is predicted, highlighting the clear instability of these systems but potential for superionic Li-ion transport if they can be stabilised. The acquired results show that the activation energy decreases and the Li-ion diffusion increases with reducing dimensionality in the targeted anti-perovskite materials. Additionally, the results obtained find that the low-dimensional-networked Br-based systems display the highest Li-ion diffusion, indicating that lattice polarisability plays an important role in these soft and unstable materials.

Therefore, the results presented in this Chapter provide interesting insights on the impact that the dimensionality and composition of the targeted systems have on their defect formation chemistry and ionic diffusion. Consequently, the results herein presented can potentially guide future experimental synthesis choices and further advances in the fields of solid-state battery and energy storage. Nevertheless, the preparation of these materials will have to consider their instability (or metastability), potentially via doping. Routes for their preparation could also be found via alternative synthesis routes (e.g., mechanochemistry). Given the recent advances in the synthesis and stabilisation of solid electrolytes, there is hope that variations of these materials will be reported in the near future.

Chapter 5 Impact of Surfaces on Ion Transport in Lithium and Sodium-Rich Anti-Perovskite Solid Electrolytes

5.1 Introduction

In recent years, solid-state batteries (SSBs) have been widely considered as a next-generation technology that has the potential to revolutionise the energy storage field. The core of the SSB technology lies in the substitution of flammable liquid electrolytes by solid counterparts, a replacement that leads to a plethora of potential benefits, including improved energy density, voltage, cycle life, safety profiles and reduced costs[8,41,46–49]. Nonetheless, several challenges still hinder the widespread use and commercialisation of SSBs such as lithium dendrite growth, low ionic conductivity, electrochemical stability, large-scale solid electrolyte (SE) synthesis and interfacial resistance, with the latter standing as one of the most complex obstacles hampering SSBs advances[8,41,49–51].

Despite the great progress made in the last decade in terms of discovering and assessing different SE candidates, the incorporation of these novel materials into the architecture of high-performing batteries has shown to be challenging[131], which can be significantly attributed to interfacial issues. The electrolyte-electrode interfaces have shown to be a fertile terrain for challenges such as chemical incompatibilities, undesired electrochemical reactions, degradation products formation and mechanical difficulties, with interfacial resistance being the limiting factor in many systems. Such problems play a significant role in rate capabilities, ionic conductivities, and cycle life, damaging the overall

battery performance. Therefore, SE candidates that are viewed as promising based on results that solely consider their bulks may be revealed as not as outstanding when their surfaces are considered alongside battery electrodes.

Given that the success of future SSB implementations relies heavily on engineering more synergic interfaces, the understanding of such regions, their underlying mechanisms and the surfaces and materials that form them stands as vital for the future of the SSB field. Consequently, studies focused on analysing SE-electrode interfaces and their respective surfaces and morphologies have gained momentum in recent years [127,128,130,203–205].

Despite this recent progress, the current understanding around such topics is still very restricted compared to that of bulk materials and not comprehensive enough to lead transformative changes that could render interfacial resistance irrelevant. Part of the issue concerning solving interfacial challenges in SSBs and the reason the volume of studies focusing on those can still be considered scarce is the inherent difficulty related to studying such interfaces, either computationally or experimentally.[61,131] While explicitly and accurately modelling SE-electrode interfaces is a complex task[61], accessing a solid-solid interface experimentally is also challenging, with the reaction layers usually being solely a small fraction of the total solids[131].

Notwithstanding the difficulties associated with simulating SE-electrode interfaces, in the context of computational atomistic modelling, calculations based on density functional theory (DFT), ab initio molecular dynamics (AIMD), and force-field-based molecular dynamics (MD) have been critical in forming the current state of knowledge by providing fundamental information regarding a plethora of pertinent mechanisms and properties involving SE-electrode interfaces and their respective surfaces. [61,96,128–130] In this scenario, research directed towards computationally exploring different SE-electrode pairings and their surfaces has flourished, with a heightened need for finding SE candidates that are chemically stable facing metallic anodes. Among the many SE material families assessed in recent years, anti-perovskites have stood out as promising SE candidates due to their excellent ensemble of

features (e.g., good Li-ion conductivity, stability against Li metal, wide electrochemical windows, low-cost synthesis, and a flexible and versatile structure).[7,61–65]

Considering the advantageous properties displayed by the anti-perovskite material family, computational interfacial studies that use and analyse the surface of anti-perovskite SE candidates have gained fresh prominence in recent times. A pertinent example is the DFT work carried out by Kim and Siegel[128] which assessed the stability of a range of low-index nonstoichiometric surfaces of Li_3OCl with different terminations and the Li_3OCl-Li metal anode interface. Their calculations revealed that the LiCl-terminated (100) surface possessed the lowest surface energy of 0.19 J m^{-2} (at 300 K), a result that indicates this surface as the most likely to form Li_3OCl at equilibrium. The study also found the oxygen-terminated interface as the most thermodynamically stable interface as well as the existence of a trade-off between strong interfacial bonding and electrochemical stability, with results concomitantly finding a large work of adhesion, suggesting potential low interfacial resistance, and a consequent lowered electrochemical window of Li_3OCl. However, the conduction band minimum remained ~1 V more negative than the Li/Li^+ redox potential, indicating stability against reduction by the anode.

The Li–Cl-terminated (100) surface was also deemed as the most favourable surface for Li_3OCl in a more recent study led by Wu *et al.*[130]. Using first-principles and AIMD calculations, the authors also assessed the Li_3OCl-Li metal anode interface and the found the self-diffusion, conductivity, and activation energy of Li ions in the interface at 300 K as 0.88 × 10^{-5} cm^2 s^{-1}, 1.60 S cm^{-1}, and 0.09 eV, respectively. Such values were greater than those for their analogues in the Li_3OCl bulk, indicating that there is a positive contribution to ionic transport in this interface.

Another interesting insight provided by an interfacial exploration involving an anti-perovskite SE is the indication of the formation of a compact double layer, a result found in a DFT study performed by Stegmaier *et al.*[96] that analysed the interface between Li_3OCl and an almost ideal metallic intercalation cathode. The results found in this work revealed high Li

vacancy concentrations building up in a single layer of the electrolyte at the interface with the cathode, leading to the formation of the compact double layer.

Although great progress has been recently made regarding the study of surfaces and SE-electrode interfaces involving anti-perovskite SEs, there are still many unanswered questions, especially about their underlying mechanisms, stabilities, and chemical compatibilities. Furthermore, most studies have only focused on the features and ionic transport mechanisms present in Li_3OCl, leaving the understanding regarding the surfaces and SE-electrode interfaces that involve other anti-perovskite SE candidates, such as Na-, K- and Mg- based anti-perovskite SEs virtually unexplored. Such lack of diversity is especially alarming when considering the limited nature of lithium resources and its consequent high associated costs in battery applications. One of the few examples of studies focused on the electrolyte surface and the SE-electrode interface for a Na-based anti-perovskite SE is the recent work carried out by Choe *et al.*[129], where the interface between a metallic Na anode and the Na-based anti-perovskite Na_6SOI_2 was explored. Such work interestingly revealed that ionic migration toward the anode is favoured by the interstitial mechanism, while the reverse path is favoured by a Na vacancy-mediated mechanism. Given that interfacial resistance is one of the greatest challenges inhibiting further progress in the SSB field, the rarity associated with works dedicated to the analysis of surfaces and interfaces related to Na-based anti-perovskite SEs is concerning.

The work introduced in this Chapter contributes to advancing the understanding related to the surfaces of and Li- Na-based anti-perovskite SEs by analysing the stability of six nonstoichiometric symmetric low-index surfaces of M_3OX (A = Li or Na; X = Cl or Br) anti-perovskites and exploring the pertinent defect chemistry, electronic properties, and ionic migration barriers across the bulk and at the surfaces of each one of the analysed systems via DFT calculations.

Our calculations show that the (100) surfaces with metal-halide terminations are the most thermodynamically stable surface type for all analysed systems. We find that that the

most preferable vacancy type and site are the same for all investigated systems, showing that the Li/Na vacancy at the first layer of the supercell is the most energetically favourable defect type and site for all systems. Additionally, our simulations predict that the choice of the cation has a greater impact on defect formation at the surfaces of the investigated anti-perovskite systems compared to the choice of halide, with the formation of any defect type at any sites being most energetically favourable in systems containing Na instead of Li, regardless of their halide content. Moreover, our migration energy barriers results illustrate the importance of accounting for the free lattice space between metal sites when designing new SE materials, with our results suggesting the existence of a trade-off between choosing highly polarisable atoms and losing critical free space in the lattice for ionic migration.

We find that although our ionic migration barrier simulations predict that Na_3OCl is the most promising SE candidate among the analysed systems, the analysis of the electronic properties reveals that the Na-based systems could potentially present lower electrochemical stabilities. Furthermore, our energy migration and electronic properties results focused on Li_3OCl and Li_3OBr suggest that mixed halide SEs (e.g., $Li_3OCl_{0.5}Br_{0.5}$) could be an interesting direction for further studies focused on Li-based anti-perovskite SEs, especially if the maintenance of the Br-containing layers at the surface is possible.

5.2 Computational Methods

The procedures followed to calculate the surface, defect formation, ion migration barriers and electronic structures for M_3OX (M = Li or Na; X = Cl or Br) are based on well-established protocols that have been widely and successfully used in similar explorations in a wide range of SE candidates.[95,128,130,192,205] All calculations herein were performed using the Vienna Ab initio simulation package (VASP) code[147] based on density functional theory with the Perdew-Burke-Ernzerhof (PBE) exchange-correlation functional[163]. Interactions between core and valence electrons were described by the projector augmented wave (PAW)

method[171]. The valence configurations used in the pseudopotentials were $1s^2$ $2s^1$ for Li, $2p^6$ $3s^1$ for Na, $2s^2$ $2p^4$ for O, $3s^2$ $3p^5$ for Cl and $4s^2$ $4p^5$ for Br.

5.2.1 Structural details

The structural details (e.g., lattice parameters and atomic positions) for all the anti-perovskite systems were obtained from the Materials Project repository[200]. The structural details for Li_2O, LiCl, LiBr, Li metal and their equivalent Na-containing structures were required for the purpose of calculating the surfaces energies and were also obtained from the Materials Project repository[200]. The energy of an isolated O_2 molecule was determined using a 10×10×10 cell.

5.2.2 Surface energy calculations

Full geometry optimisations of the bulk systems were carried out by allowing for relaxation of the lattice and ions. The energy of the electronic ground state was converged to within 10^{-5} eV and the cutoff energy and convergence tolerance were set to 500 eV and 0.01 eV/Å, respectively. Convergence tests with respect to k-point sampling density for bulk systems were performed for the optimisation of the crystals. A Monkhorst-pack (MP) 4×4×4 *k*-point mesh was found adequate for the Li_3OCl, Na_3OCl and Na_3OBr systems, while a MP 5×5×5 *k*-point mesh was needed for Li_3OBr. A MP 3×3×3 *k*-point mesh was used for Na_2O, LiBr and NaBr and a MP 2×2×2 *k*-point mesh was chosen for Li_2O, LiCl and NaCl. For the Li metal and Na metal systems, a MP *k*-point mesh of 10×10×10 and a MP 15×15×15 *k*-point mesh were found to be suitable, respectively.

In order to create the surface models, we used the periodic "slab" approach, where the geometrically optimised bulk crystal is cut alongside the desired Miller plane (h k l) to expose

the targeted surface. The crystal structure of Li_3OCl showing the three Miller indices cuts used is shown in Figure B.2.1, in the Appendix B2. We focused on six-low index symmetric surfaces for each system analysed, namely, two (100) surfaces, one with a metal-halide termination and one with a metal-oxygen termination, two (110) surfaces, one terminated solely by the metal atoms and one terminated by a metal-oxygen-halide ensemble, and two (111) surfaces, one with a metal-halide termination and one terminated solely by oxygens. The slab models were built with the desired terminations and symmetrical features. Respectively, the (100) metal-halide terminated, (100) metal-oxygen terminated, (110) metal terminated, (110) metal-oxygen-halide terminated, (111) metal-halide terminated and (111) oxygen terminated slabs possessed 52, 53, 47, 43, 44 and 46 atoms each. The lengths of the slabs used can be found in Table 5.1. For the Li-based surfaces, the lengths of the slab models used for the (100) metal-halide terminated, (100) metal-oxygen terminated, (110) metal terminated, (110) metal-oxygen-halide terminated, (111) metal-halide terminated and (111) oxygen terminated slabs were 39-40, 39-40, 25, 23, 18 and 20 Å. For the Na-based surfaces, the lengths of the slab models used for the (100) metal-halide terminated, (100) metal-oxygen terminated, (110) metal terminated, (110) metal-oxygen-halide terminated, (111) metal-halide terminated and (111) oxygen terminated slabs were 45-46, 46-47, 29-30, 27, 21-22 and 24 Å.

Surface energies for all slab models containing a 12 Å vacuum region were calculated by fixing the lattice parameters and allowing ionic relaxations. The specific MP *k*-point mesh used for optimising each one of the surfaces created can be found in Tables B1.1 and B1.2 in Appendix B1. The energy of the electronic ground state was converged to within 10^{-5} eV, and the cutoff energy and convergence tolerance were set to 500 eV and 0.01 eV/Å, respectively. The effects of the slab size and vacuum thicknesses (12−30 Å) were tested and it was revealed that the surface energy was well converged using the parameters described above.

Table 5.1. Lengths of the slab models (Å) used for (100) MX, (100) MO, (110) M, (110) MOX, (111) MX and (111) O (M = Li or Na; X = Cl or Br) surface types

	Length of slab (Å)			
Surface Type	M = Li, X = Cl	M = Li, X = Br	M = Na, X = Cl	M = Na, X = Br
(100) MX	38.7394	39.5197	45.3855	46.3609
(100) MO	38.8374	39.9697	45.6278	46.7333
(110) M	24.7457	25.2591	29.2400	29.6771
(110) MOX	22.6780	22.9897	27.0494	27.4279
(111) MX	17.9647	18.3858	21.298	21.6682
(111) O	19.5673	19.6744	23.5574	23.7119

5.2.3 Defect formation energy calculations

Defective models were created by using 3 x 3 x 1 expansions of the (100) metal-halide-terminated surfaces, corresponding to supercells containing 333 atoms (15 layers). Convergence tests showed that such number of layers were sufficient for all supercells.

In order to create isolated single vacancy defects (e.g., $V_{Li}^{/}$, $V_{Cl}^{/}$, $V_{O}^{/}$ in Kröger–Vink notation) in the structures, we systematically removed the targeted atom from the middle section of the supercell. We carried out this procedure for all possible non-equivalent atoms in the first three anti-perovskite layers of the supercell (i.e., first seven layers of the supercell), labelling the vacancies with respect to their positions in relation to the central oxygen atom in the layer they were created. A schematic representation displaying the analysed layers and labelling system is given in Figure 5.2.

5.2.4 Migration energy calculations

In order to investigate the ionic migration pathways and energy barriers on the analysed defective bulk systems and their surfaces, the nudged elastic band (NEB) method[179] implemented in VASP was used. This is a versatile method for finding energy saddle points for ionic migration previously used in the literature in the analysis of numerous SE candidates[95,130,192,205]. NEB calculations were performed by fixing the lattice parameters and allowing ionic relaxations while using a single k-point. The energy of the electronic ground state was converged to within 10^{-5} eV, and the cutoff energy and convergence tolerance were set to 520 eV and 0.01 eV/Å, respectively. The number of images used between fixed endpoints was five. The defective structures used for such endpoints were optimised using the same electronic ground state convergence and cutoff energy parameters used for the NEB calculations.

5.2.5 Density of states calculations

Density of states (DOS) were calculated for all anti-perovskite systems and surfaces using PBE[163] and hybrid DFT Heyd–Scuseria–Ernzerhof (HSE06)[167] functionals, the latter being used to improve bad gaps and charge localisation. The tetrahedron method with Blöchl corrections was used for the calculation of the DOS plots, with the global break condition for the electronic self-consistency-loop set as 10^{-6} eV. The k-point mesh used for DOS calculations were two times greater than those used for the same systems during their geometry optimisation. DOS plots were built using the Sumo Python toolkit[206].

5.3 Results

5.3.1 Surface energies and stability

Prior to exploring the surface properties, it is fundamental to determine which surface cuts and terminations for each analysed system have greater stability and are more energetically favourable to form. The stability of six nonstoichiometric symmetric low-index surfaces for M_3OX (M = Li or Na; X = Cl or Br) anti-perovskites was examined (Figure B2.2 in Appendix B2) via the calculation of their respective surface energies. The six low-index surfaces were, namely, two (100) surfaces, one with a metal-halide termination and one with a metal-oxygen termination, two (110) surfaces, one terminated solely by the metals and one terminated by a metal-oxygen-halide ensemble, and two (111) surfaces, one with a metal-halide termination and one terminated solely by oxygens. The surface energy (E_{surf}) was calculated from:

$$E_{surf} = \frac{1}{2S}[E_{slab} - nE_{bulk} - m\mu_i] \qquad (5.1)$$

where E_{slab} and E_{bulk} are the calculated free energies of the slab surface system and the bulk unit cell, respectively, with n representing the number of bulk unit cells contained in the slab structure. The surface area is represented by S and μ_i is the chemical potential of the species that exceeds the stoichiometric expectancy in the slab system and m is the number of formula units that needs to be removed. As an example, the structural formula of a Li_3OCl slab with ten atomic layers could be described as $Li_{31}O_{10}Cl_{11}$. In this case, the stoichiometric expectancy would be to have a system with the structural formula equal as $Li_{30}O_{10}Cl_{10}$. Therefore, the compound LiCl is exceeding in one unit the stoichiometric expectancy in this slab and thus its chemical potential is used as μ_i in Equation 5.1, with m equal to one, in order to calculate the surface energy of this particular Li_3OCl slab system. Such procedure to calculate surface energies for anti-perovskite systems has been successfully used previously in

the literature.[130,205] The calculated surface energies for the anti-perovskite systems are displayed in Figure 5.1.

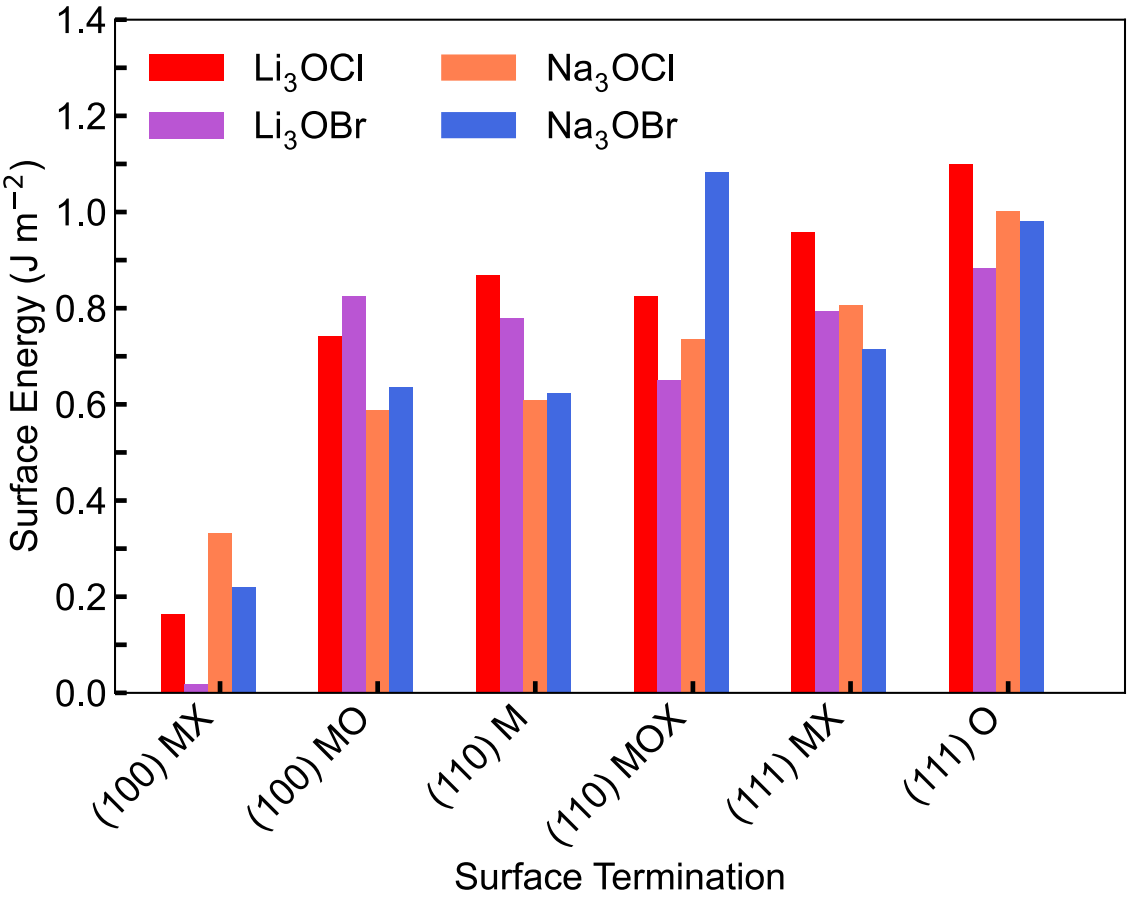

Figure 5.1. Calculated surface energies for M_3OX (M = Li or Na; X = Cl or Br).

Our calculated surface energies for the Li_3OCl system for all six analysed low-index surface types are in excellent agreement with the equivalent surface energies predicted by Kim and Siegel[128] and Wu *et al.*[130] for the Li_3OCl system. Similarly, our calculated surface energies for the Li_3OBr system are in great agreement with the surface energies predicted by

Luo *et al.*[205] for the (110) metal-terminated surfaces, (111) oxygen-terminated surfaces and all (100) surfaces.

Given that a lower surface energy indicates its more energetically favourable formation, the results depicted in Figure 5.1 reveal that (100) surfaces with metal-halide terminations are the most thermodynamically stable surface type for all analysed systems. Such preference for (100) surfaces terminated by metal-halide ensembles agrees with previous findings for the Li_3OCl system reported by Kim and Siegel[128] and Wu *et al.*[130] and with previous reports authored by Luo *et al.*[205] for Li_3OBr.

Our calculated surface energies for the (100) metal-halide terminated surfaces are 0.164, 0.018, 0.332 and 0.220 J m^{-2} for the Li_3OCl, Li_3OBr, Na_3OCl and Na_3OBr systems, respectively. Given their low energies, the (100) metal-halide terminated surfaces were adopted for the intrinsic defect formation and ionic transport investigations in the target systems, as described below.

5.3.2 Intrinsic defect formation and ion transport

In this section, we explore the defect chemistry pertinent to the surfaces of the selected M_3OX (M = Li or Na; X = Cl or Br) anti-perovskite systems and further advance to study the ionic migration paths that are most energetically favourable at the bulk and at the surfaces of each one of the analysed systems. In this context, the work presented in this section provides important information in terms of ionic mobility at the bulk and at the surfaces of the chosen anti-perovskite systems and contributes greatly to future interfacial studies that choose to use such anti-perovskite structures as their SE.

As discussed in Chapters 1, 2 and 4, vacancy-mediated ionic transport mechanisms have showed to be pertinent to Li_3OCl, Li_3OBr and their low-dimensional-networked (DN) anti-perovskite analogue systems studied in Chapter 4. Indeed, the Li-halide Schottky defect

type was found to be the most energetically favourable intrinsic disorder for the bulk of the great majority of anti-perovskite systems analysed in Chapter 4.

Considering this prominent role vacancy-mediated mechanisms display at the bulk of the selected anti-perovskites studied in Chapter 4 and considering the similarities between those structures and the M_3OX (M = Li or Na; X = Cl or Br) anti-perovskites chosen to be studied, we herein explore the migration of a Li/Na atom into a single vacancy at the surface of the selected systems to systematically study the contribution of such vacancies to Li^+/Na^+ conductivity.

First, we calculate the defect formation energy for isolated single Li/Na, Br/Cl and O vacancies in the structures, in order to reveal the defect type that is the most energetically favourable in each one of the analysed systems. Defective models were created by using 3 x 3 x 1 expansions of the (100) metal-halide-terminated surfaces, corresponding to supercells containing 333 atoms (15 layers).

To create isolated single vacancy defects (e.g., $V_{Li}^{/}$, $V_{Cl}^{/}$, $V_{O}^{/}$ in Kröger–Vink notation) in the structures, we systematically removed the targeted atom from the middle section of the supercell. We carried out this procedure for all possible non-equivalent atoms in the first seven layers of the anti-perovskite supercell, labelling the vacancies with respect to their positions in relation to the central oxygen atom in the layer they were created. A schematic representation displaying the analysed layers and labelling system can be seen in Figure 5.2. Their respective defect formation energies were calculated following Equation (5.2):

$$E_{def} = E_{tot}[def] - E_{tot}[perf] - \sum_i n_i \, \mu_i \qquad (5.2)$$

where $E_{tot}[def]$ represents the free energy of the defective supercell, $E_{tot}[perf]$ is the free energy of the perfect supercell (i.e., with no defects present in the structure), n_i is the number of atoms of type i that had to be removed from (n_i < 0) the perfect supercell when the defect is created and μ_i is the chemical potential of i. Such procedure to calculate defect formation energies for anti-perovskite systems has been successfully used previously in the literature.[130,135,205,207]

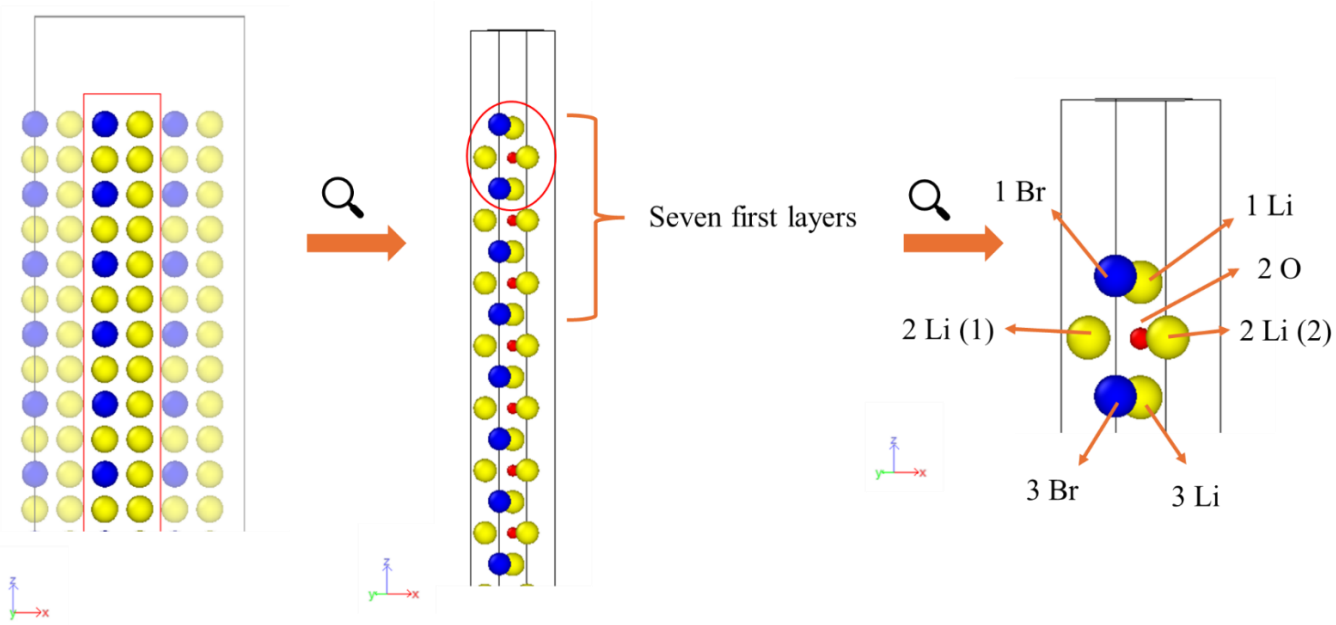

Figure 5.2. Schematic representation of analysed surface layers and labelling system.

The calculated defect formation energies for all targeted systems are displayed in Figure 5.3. Given that a lower defect formation energy indicates its more energetically favourable formation, the results in Figure 5.3 reveal key information regarding the defect chemistry in the investigated systems.

a)

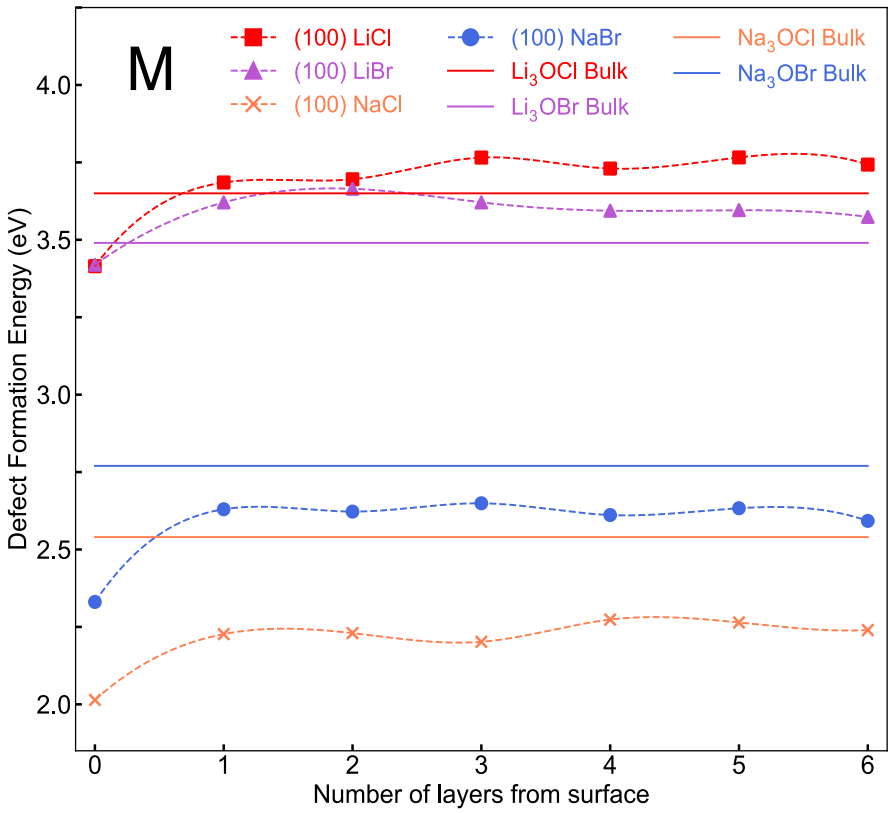
M
(100) LiCl
(100) LiBr
(100) NaCl
(100) NaBr
Li3OCl Bulk
Li3OBr Bulk
Na3OCl Bulk
Na3OBr Bulk
Defect Formation Energy (eV)
Number of layers from surface

b)

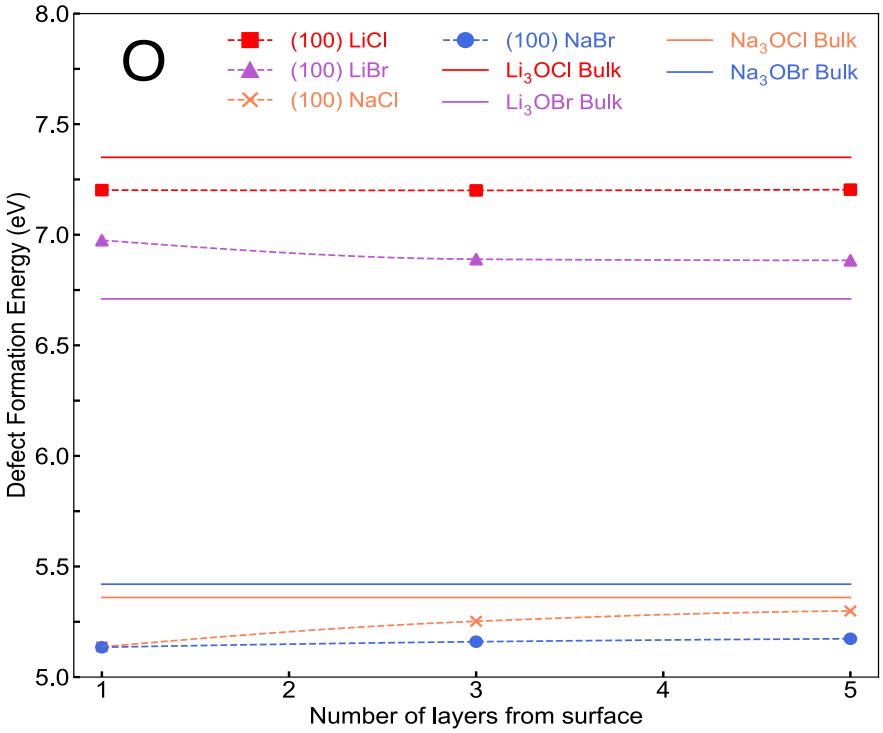
O
(100) LiCl
(100) LiBr
(100) NaCl
(100) NaBr
Li3OCl Bulk
Li3OBr Bulk
Na3OCl Bulk
Na3OBr Bulk
Defect Formation Energy (eV)
Number of layers from surface

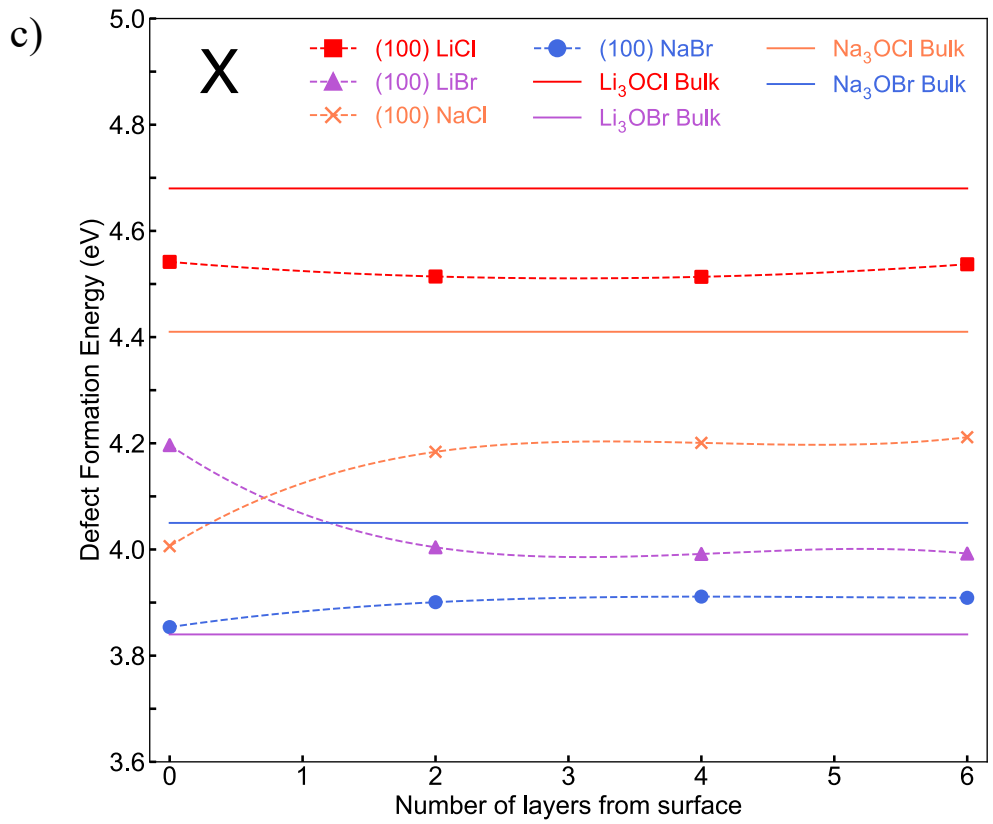

Figure 5.3. Defect formation energies for (a) M, (b) O and (c) X vacancies in M_3OX (M = Li or Na; X = Cl or Br) as a function of surface depth. Bulk values are also presented for comparison.

First, the results reveal that the most preferable vacancy type and site are the same for all investigated systems, showing that the Li/Na vacancy at the first layer of the supercell is the most energetically favourable defect type for all systems. The defect formation energies calculated for this defect type and site for all chosen systems are displayed in Figure 5.4. The most preferable vacancy site being at the first layer of the supercell was expected as there are less electrostatic constraints at the top layer compared to its sublayers. Additionally, Li vacancies are known in the literature for having most energetically favourable formation

energies than halide-based or oxygen vacancies in anti-perovskite systems[205]. This trend is confirmed in our results, which show that the defect formation energies of Li/Na vacancies are lower than those of halide-based or oxygen vacancies for all investigated systems.

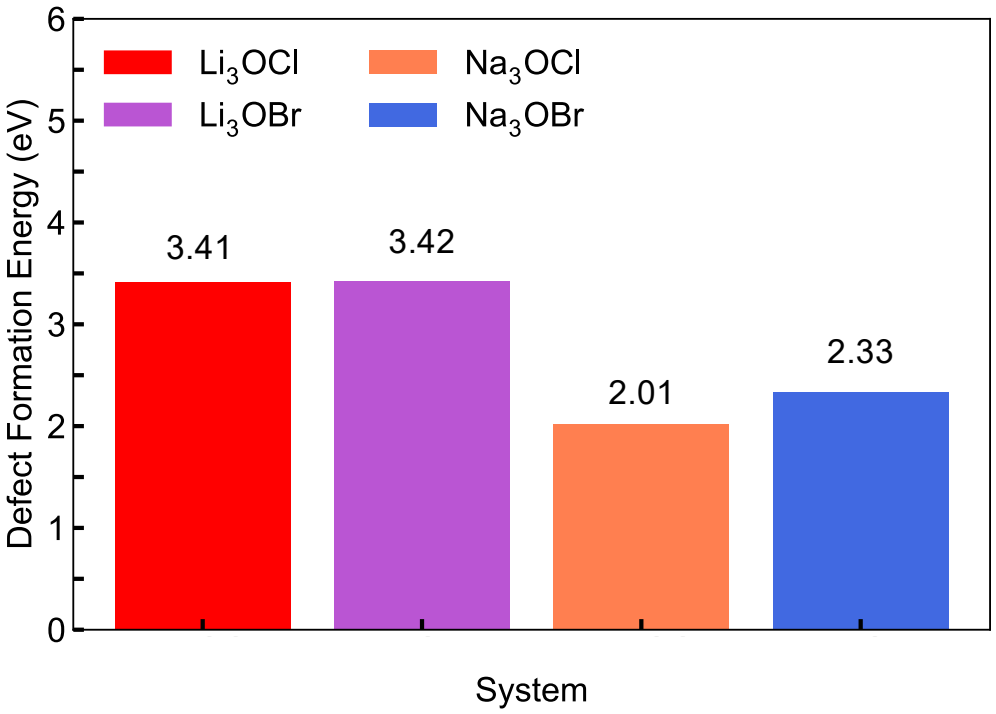

Figure 5.4. Calculated defect formation energies for Li/Na vacancies at the first layer in M_3OX (M = Li or Na; X = Cl or Br).

The comparison of the results across the different metal choices shows the formation of any defect types at any sites is most energetically favourable in systems containing Na instead of Li, regardless of their halide content. This could be potentially caused by the weaker metal-halide interactions present in Na-based systems due to Na higher polarisability. Interestingly, no similar clear trend was found when comparing the results across different halide choices, revealing that the choice of the metal has a greater impact on the defect

formation at the surfaces of the investigated anti-perovskite systems compared to the choice of the halide.

Considering the defect formation energies obtained and the importance that ionic migration across the bulk and surfaces has for promising SEs, we analysed the migration of neighbouring Li/Na atoms into the most preferable defect type and site at the surface and in the bulk for all analysed systems.

We calculated the migration energy barriers for two possible pathways via the NEB method. The first pathway, abbreviated as Pathway 1, consists of a Li/Na atom that is adjacent to the defect site migrating into the defect site at the same layer level. The second pathway, abbreviated as Pathway 2, consists of the closest Li/Na atom to the defect site, which is in the subsurface layer compared to the defect site, migrating into the defect site. An illustration of the two pathways used is shown in Figure 5.5.

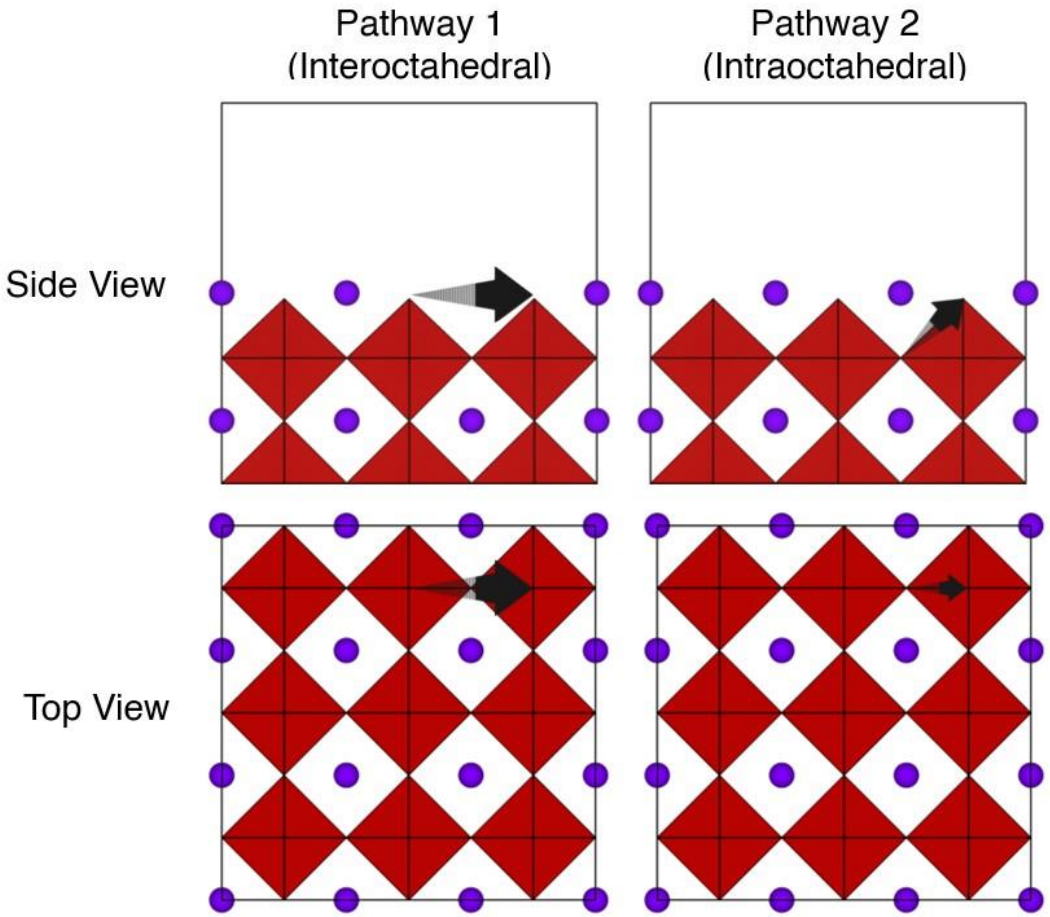

Figure 5.5. Schematic representations of the two NEB pathways considered for Li and Na migration, i.e., pathway 1(interoctahedral) and pathway 2 (intraoctahedral) hopping, at the metal-halide-terminated (100) surface of M_3OX (M = Li or Na; X = Cl or Br). The black arrows show the path of the migration Li or Na atom.

The calculated migration energy barriers are displayed in Figure 5.6 and 5.7. The results obtained for both pathways in the bulk of the Li-based systems are in good agreement with previous computational findings[95,192]. Similarly, the results achieved for both pathways at the surface of Li_3OCl agrees well with previous literature reports[192].

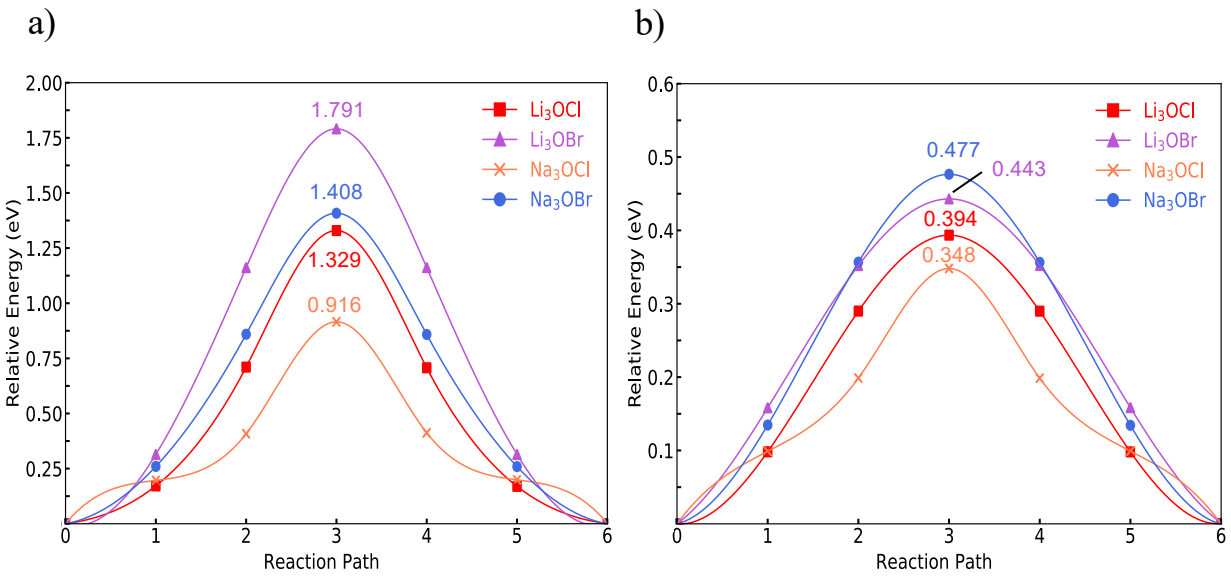

Figure 5.6. Calculated migration energies barriers (eV) for bulk M_3OX (M = Li or Na; X = Cl or Br) systems where a) shows results obtained following Pathway 1 and b) shows results obtained following Pathway 2.

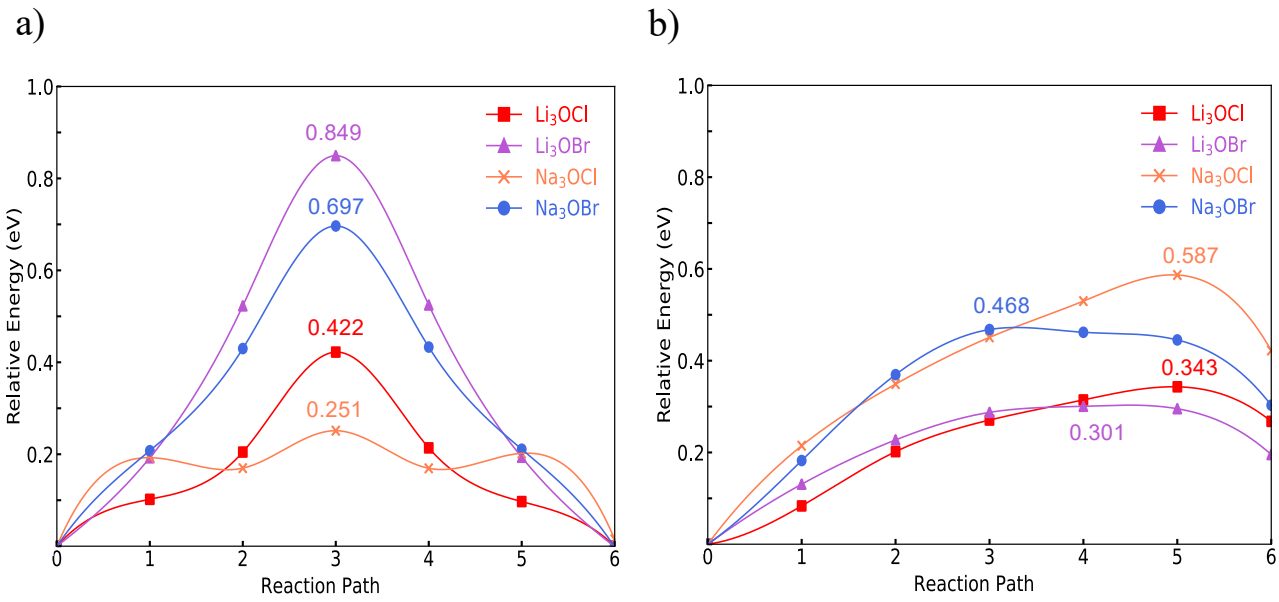

Figure 5.7. Calculated migration energies barriers in (100) metal-halide terminated surfaces in M_3OX (M = Li or Na; X = Cl or Br) systems where a) shows results obtained following Pathway 1 and b) shows results obtained following Pathway 2.

The comparison of the results related to ionic diffusion occurring in the bulk shows that ionic migration is more energetically favourable for all systems when path 2 is followed. This preference for path 2 over path 1 was seen previously in the literature for migrations across the bulk in Li_3OCl and Li_3OBr in a report by Zhang *et al.*[192]. Additionally, this trend was also expected due to path 2 involving the migration of the closest Li/Na neighbouring atom to the defect site into the vacancy site.

The analysis of the results for migrations across the bulk following path 2 provides interesting insights regarding the impact that highly polarisable atoms and lattice free space have in the ionic diffusion across the bulk in the analysed systems.

Our simulations show that Cl-based systems display more energetically favourable migrations compared to their Br-based counterparts. This preference was seen previously in the literature for Li_3OCl and Li_3OBr[192] and we herein show that this trend also holds for Na-based systems. Concomitantly, our results show that while Cl-based systems display lower migration barriers when containing Na instead of Li, the same trend is not seen in their Br-analogues, which display more energetically favourable migrations when their respective systems contain Li instead of Na.

It is known in the literature that the exchange of less polarisable atoms for larger, softer, and more polarisable atoms (e.g., the replacement of Cl by Br or the substitution of Li by Na) weakens the metal-halide interactions which could potentially improve ionic diffusion[61,111,208], as the metal ion would be allowed to move more freely. Such effect could potentially justify the preference seen in our results from Cl-based systems to be paired with Na instead of Li. As Na is more polarisable than Li, the Na-Cl interactions would be weaker than the Li-Cl interactions, which could potentially lead to an easier migration of the Na atom compared to the Li atom.

However, our results also show that Br-based systems have more energetically favourable migrations when containing Li instead of Na which would not be expected if only considering the atoms polarisability changes in the involved systems. As Br is also a big, soft and highly polarisable atom, the free space between the metal sites is severely narrowed when Br is paired with another big, soft and highly polarisable atom like Na, which could potentially hinder ionic diffusion in such systems.

The importance of free space for ionic migrations across the bulk can also be seen when comparing our results based on their halide content, with Cl-based systems displaying more energetically favourable migrations compared to their Br-based counterparts. Although metal-halide interactions are weaker in Br-based systems, the free space between metal sites is also reduced in Br-based systems, leading to less favourable ionic migrations.

Therefore, our results suggest that although the atoms polarisability still plays an important role in the ionic diffusions across the bulk for the investigated systems, the free space between metal sites stands as a critical parameter for ionic migrations across their bulks. Such relevance is understandable when considering that the bulk is the most compact section of the systems. Overall, our simulations show that Na_3OCl is the system that provides the most energetically favourable ionic diffusion across its bulk, with Na_3OBr delivering the highest migration energy barrier.

The comparison of the results related to ionic diffusion occurring at the surface shows that ionic migration is more energetically favourable for the majority of the systems when path 2 is followed. This preference was expected due to path 2 involving the migration of the closest Li/Na neighbouring atom to the defect site into the vacancy site.

The only exception to this trend is the Na^+ migration that occurs at the surface of Na_3OCl, which occurs with higher favourability when path 1 is followed. Considering that path 2 involves a layer change during the migration pathway, this exception could potentially be justified by Na_3OCl possessing stronger Na-halide interactions than Na_3OBr and a larger metal atom present (i.e., Na) than those in Li_3OCl. The migration via path 2 would not be hindered in Li_3OCl and Li_3OBr due to the lack of an atom as large as Na in their structures, allowing for greater lattice space and a consequential easier migration between layers. Concomitantly, the migration via path 2 would not be hindered in Na_3OBr as this system displays the weakest metal-halide interactions, which could potentially lead to a softer lattice that would allow for easier ionic diffusion across layers. Consequently, the migration via path 2 in Na_3OCl could potentially be hindered by the lack of lattice free space caused by the presence of Na and the stronger Na-halide interactions in this system that would not allow for a flexible lattice.

The comparison of the results related to ionic diffusion occurring at the surface following their respective most favourable paths shows that the majority of trends observed for the results related to ionic diffusion across the bulk are maintained in the results related to

ionic migration at the surfaces. The only exception to this is that Li-based systems will display lower migration barriers at the surface when having Br instead of Cl in their chemistries, with the opposite preference being observed for the bulk results. This result suggests that as the surface is not as compact as the bulk, the importance of maintaining a large free lattice space between the metal sites is lower at the surface when having Li-based systems, with the weakened metal-halide interactions caused by the replacement of Cl by Br being the most prevalent factor in this case.

Altogether, our migration energy barriers results illustrate the importance of considering beyond atoms polarisabilities and accounting for the free lattice space between metal sites when designing new SE materials. Our results suggest the existence of a trade-off between choosing highly polarisable atoms and losing critical free space in the lattice for ionic migration. Indeed, in both our results for ionic migrations across the bulk and surfaces, Na_3OBr is the system that displays the highest migration barrier, even though this system possesses two highly polarisable atoms (i.e., Na and Br). These results could potentially be caused by the lack of free space in its lattice.

Overall, our simulations show that Na_3OCl is the system that provides the most energetically favourable ionic diffusion across its bulk and at the surface, followed by Li_3OCl and Li_3OBr. Considering the importance of an effective ionic migration across a SE for SSBs, this result suggests that Na_3OCl could be a promising SE candidate.

Our results focused on Li_3OCl and Li_3OBr also suggest that mixed halide SEs (e.g., $Li_3OCl_{0.5}Br_{0.5}$) could be an interesting direction for further studies focused on Li-based anti-perovskite SEs, especially if the maintenance the Br-containing layers at the surface is possible.

5.3.3 Density of states

As previously stablished in Chapter 1 and 2, an ideal SE candidate should display high electrochemical stability, negligible electronic conduction, and no dendrite formation over cycling. Such properties are impacted by the material electronic structure and the study of DOS plots can provide pertinent insights regarding such electronic properties in SE candidates.

DOS plots calculated using hybrid DFT HSE06 functionals for all analysed pristine bulk systems and their (100) metal-halide terminated surfaces can be seen in Figure 5.8 and 5.9, respectively. Analogue DOS plots created using Perdew–Burke–Ernzerhof (PBE) functionals can be seen in Figure B3.1 and Figure B3.2 in the Appendix B3. The calculated bandgaps from the hybrid functionals-generated DOS can be seen in Figure 5.10. Our calculated bandgaps for the bulk materials (Li_3OCl (6.7 eV), Li_3OBr (6.1 eV), Na_3OCl (3.7 eV) and Na_3OBr (3.5 eV)) are in good agreement with those previously reported in the literature[209–211]as are the bandgaps of 5.6 and 5.5 eV for the metal-halide terminated (100) surfaces of Li3OCl and Li3OBr, respectively[96,212].

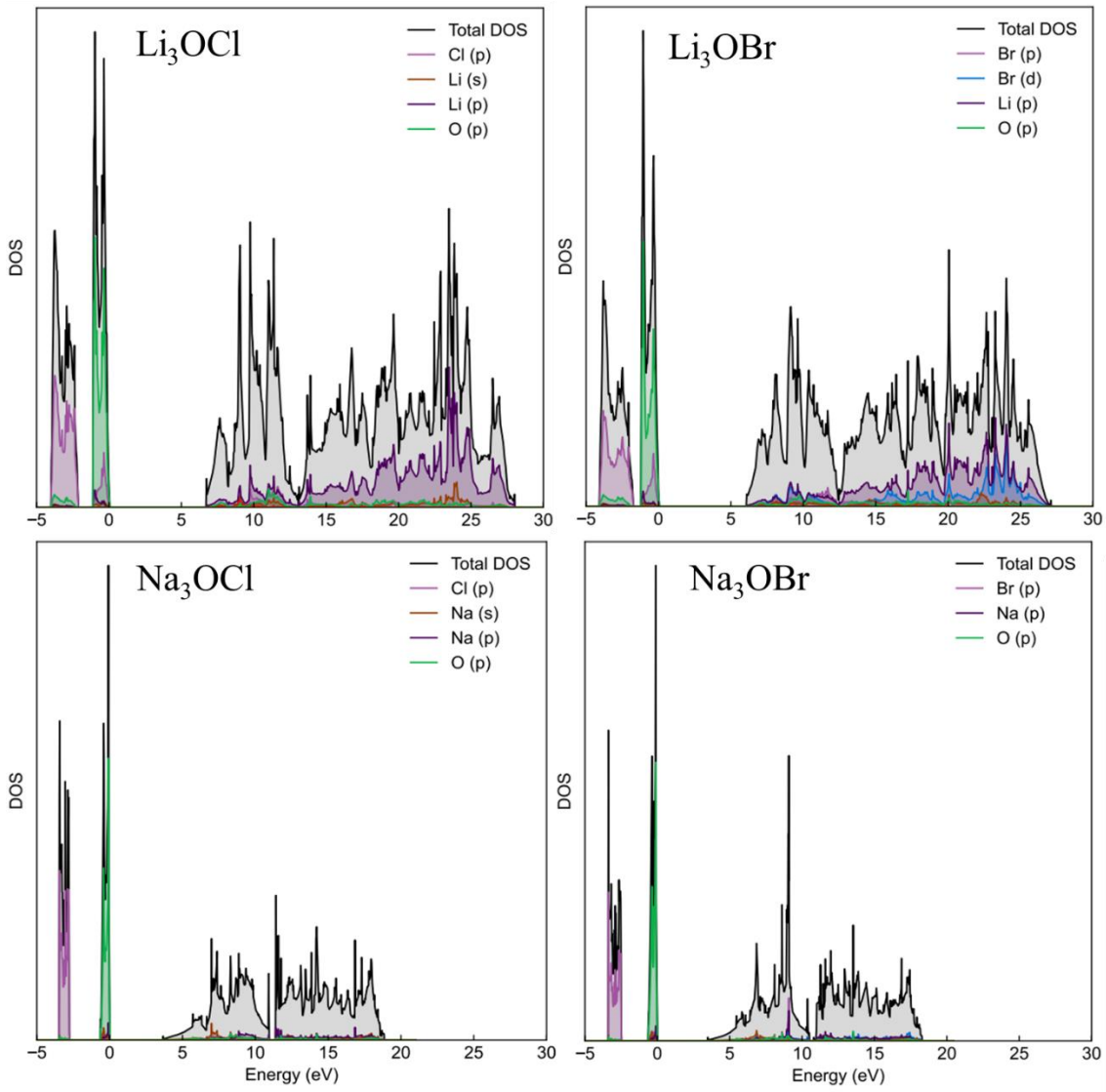

Figure 5.8. DOS plots calculated using hybrid DFT HSE06 functionals for all analysed pristine M_3OX (M = Li or Na; X = Cl or Br) bulk systems.

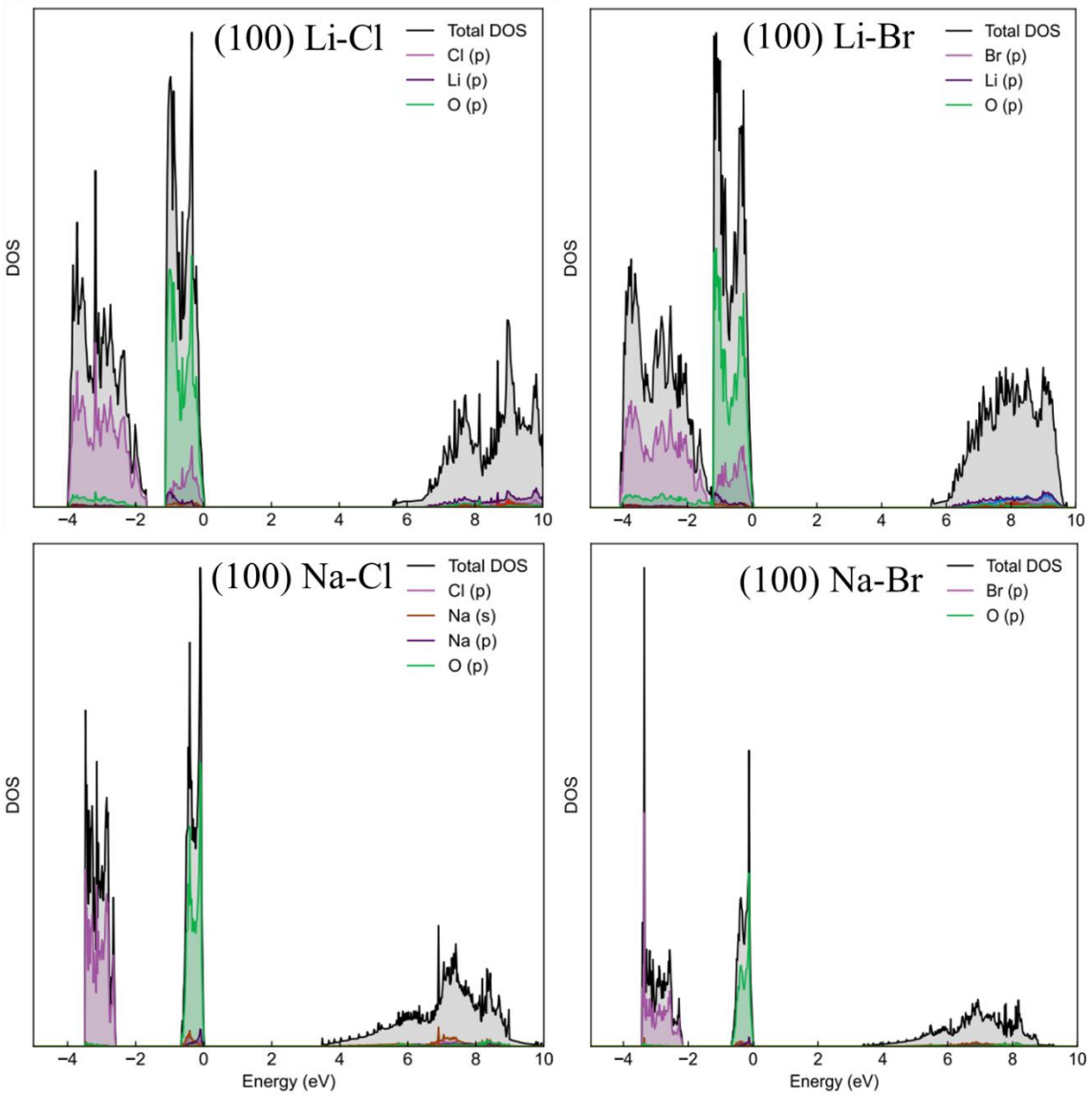

Figure 5.9. DOS plots calculated using hybrid DFT HSE06 functionals for all analysed (100) metal-halide terminated surfaces in M_3OX (M = Li or Na; X = Cl or Br) systems.

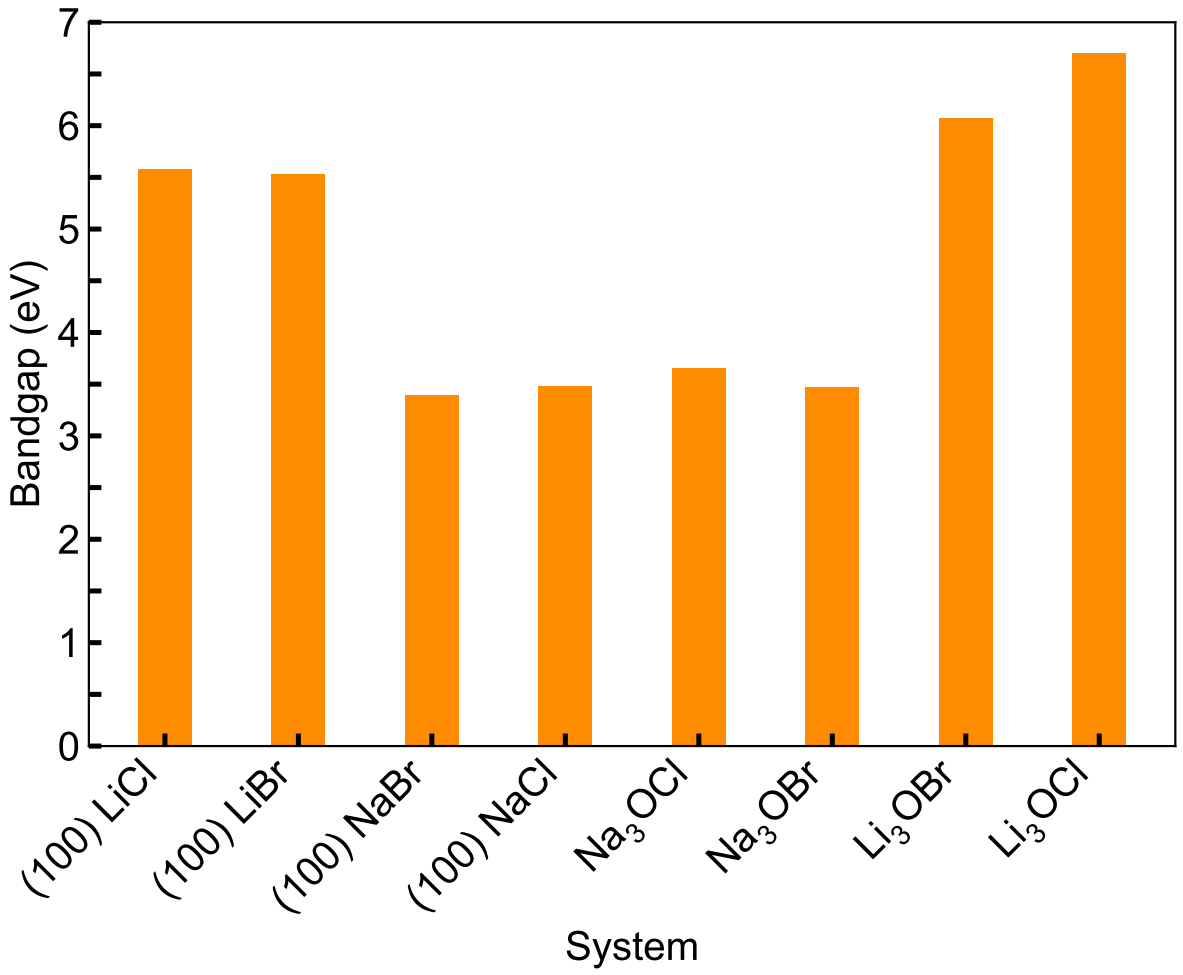

Figure 5.10. Calculated bandgaps from the hybrid functionals-generated DOS for all analysed (100) metal-halide terminated surfaces in M_3OX (M = Li or Na; X = Cl or Br) and their respective bulk systems.

Our results reveal that upon substitution of Li by Na, the bandgap decreases for all systems. Additionally, it is possible to notice from our results that the effect of halide substitution on the bandgap is not as significant as the effect caused by metal substitution in equivalent systems. However, our calculations show that the substitution of Cl by Br causes the bandgap to decrease.

A large bandgap (>5 eV) could potentially bring a series of advantages to a SE candidate. A SE is not considered to break down if it has a large bandgap and, additionally, a large bandgap shows that the material is a poor electronic conductor, a requirement for promising SE candidates. Moreover, a large bandgap improves the material electrochemical stability and could prevent the formation of dendrites and, consequently, reduce the risk of short-circuits and reduced shelf-life.

Our results show that Li_3OCl and Li_3OBr are the bulk systems that display the most promising results in terms of their bandgaps, while the Li_3OCl and Li_3OBr surfaces are deemed to possess the most promising results among the surfaces considered. Such results suggest that mixed halide SEs (e.g., $Li_3OCl_{0.5}Br_{0.5}$) could be an interesting choice for future studies focused on Li-based anti-perovskite SEs, especially if the maintenance the Br-containing layers at the surface is possible, reinforcing the conclusions draw for the results shown in the previous section. Additionally, our results reveal that the substitution of Li by Na could led to a narrowing of the materials bandgap which could, consequently, lead to lower electrochemical stabilities in those Na-based systems.

5.4 Conclusions

In this Chapter, we analysed the stability of six nonstoichiometric symmetric low-index surfaces of M_3OX (M= Li, Na; X = Cl, Br) anti-perovskites and explored the pertinent defect chemistry, electronic properties, and ionic migration barriers across the bulk and at the surfaces of each one of the analysed systems via DFT calculations.

The results presented here show that (100) surfaces with metal-halide terminations are the most thermodynamically stable surface type for all analysed systems, a preference that agrees with previous literature reports for Li_3OCl and Li_3OBr.

Our results also reveal that the most preferable vacancy type and site are the same for all investigated systems, showing that the Li/Na vacancy at the first layer of the supercell is the most energetically favourable defect type for all systems. The most preferable vacancy site being at the first layer of the supercell was expected as there are less electrostatic constraints at the top layer compared to its sublayers. Additionally, our simulations predict that the choice of the cation has a greater impact on the defect formation at the surfaces of the investigated anti-perovskite systems compared to the choice of halide, with the formation of any defect type at any sites being most energetically favourable in systems containing Na instead of Li, regardless of their halide content.

Moreover, our migration energy barriers results illustrate the importance of accounting for the free lattice space between metal sites when designing new SE materials. Our results suggest the existence of a trade-off between choosing highly polarisable atoms and losing critical free space in the lattice for ionic migration. From all the investigated systems, our migration energy simulations show that Na_3OCl is the system that provides the most energetically favourable ionic diffusion across its bulk and at the surface, followed by Li_3OCl and Li_3OBr. Considering the importance of an effective ionic migration across a SE has for SSBs, this result suggests that Na_3OCl could be a promising SE candidate. The analysis of our DOS plots results, however, show a significant reduction in the bandgap of the analysed anti-perovskite systems and surfaces upon substitution of Li by Na, which could potentially lead to lower electrochemical stabilities in the analysed Na-based systems and surfaces. Such results suggest that future efforts should be applied in terms of discovering mechanisms that could improve the stability of such Na-based systems. An example of a possible future direction is investigating the impact of different coatings on the stability of such Na-based anti-perovskite SEs.

Furthermore, our energy migration results focused on Li_3OCl and Li_3OBr suggest that mixed halide SEs (e.g., $Li_3OCl_{0.5}Br_{0.5}$) could be an interesting direction for further studies focused on Li-based anti-perovskite SEs, especially if the Br-containing layers can be

maintained at the surface. The analysis of our DOS results reinforces this suggestion by revealing that Li_3OCl and Li_3OBr are the bulk systems that display the most promising results in terms of their bandgaps, while the Li_3OCl and Li_3OBr surfaces are deemed to possess the most promising results among the surfaces considered.

In this context, this study provides important information in terms of electrochemical stability, defect chemistry and ionic migration mechanisms at the bulk and at the surfaces of the chosen anti-perovskite systems and, consequently, contributes greatly to the understanding of solid electrolytes and their interfaces.

Chapter 6 Conclusions and Future Work

6.1 Conclusions

Solid electrolytes (SEs) are the heart of solid-state batteries (SSBs), a next-generation technology that has the potential of revolutionising the energy storage field in the next decade by delivering lighter, safer and more durable batteries. Given the central role SEs play in the performance of SSBs, the success of future SSB implementations relies heavily on the discovery, design and development of new SEs that can deliver the performance needed to allow the large-scale production and consumption of SSBs. In this context, research focused on investigating SE material families is vital for finding candidates endowed with lower costs, suitable mechanical properties and high ionic conductivity, stability, synthesisability, scalability, and electrode compatibility.

Anti-perovskites stand out as promising SE candidates as a result of their high ionic conductivity, stability against lithium metal anodes, low cost and structural versatility, an ensemble of advantages rarely seen concomitantly in other SE candidates. Despite the considerable literature existent focused on anti-perovskite materials, the features, potential and many of the elementary processes and underlying mechanisms that explain their behaviour, especially of those with non-traditional chemistries and/or structures, are still not fully understood.

Computational modelling is a fundamental tool to tackle the critical challenges associated with the discovery and design of SEs, providing key insights that cannot be found

or are harder to obtain experimentally. Computational atomistic simulations based on density functional theory (DFT), machine learning (ML), ab initio molecular dynamics (AIMD), molecular dynamics (MD), and high-throughput approaches have been critical in identifying promising anti-perovskite SE candidates and in understanding and tailoring a wide variety of important phenomena and properties, including ionic and electronic conductivity, diffusion mechanisms, stability, defects and doping and interfacial resistance and compatibility.

A timely discussion on the remaining computational challenges facing these materials has been provided here in Chapter 2, along with a perspective on their possible future advances and applications. The use of ML force fields for interfacial explorations has been focused on is widely expected to enable the analysis of much more complex and larger simulation cells and time scales while retaining DFT levels of accuracy, which will be key for allowing for the design of stable conducting interfaces in which practical SSBs can be built on.

This Thesis uses a range of computational modelling techniques to investigate the relevant defect chemistry, properties and ionic transport mechanisms in a variety of Li- and Na-based anti-perovskite materials, providing fundamental information regarding their potential for future SE applications.

In Chapter 4, defect and classical MD calculations were used to explore the pertinent defect chemistry and ionic diffusion mechanisms in a range of Li_xOX_y (X = Cl or Br; x = 3–6; y = 1–4) anti-perovskites with zero- to three-dimensional structures. The simulations reveal that the targeted systems generally possess Li–halide Schottky defect pairs as dominant native defects, revealing the pertinence of a vacancy-based ionic transport mechanism in these systems. The results show that defect formation for all systems becomes energetically more favourable as the dimensionality of the system is lowered and that defect formation is generally energetically preferable in the Li_xOCl_{x-2} series compared to the equivalent structures in the Li_xOBr_{x-2} set.

The MD calculation results in Chapter 4 also predict the low-temperature melting of the 1-dimensional-networked (DN) and 0DN systems at temperatures as low as 300 K, highlighting the clear instability of these systems but potential for superionic Li-ion transport if they can be stabilised. The MD simulations also reveal the strong connection between Li-ion dynamics and dimensionality in these anti-perovskite materials, where increased lithium-ion diffusion and decreased activation energy can be seen as dimensionality is reduced. Additionally, enhanced Li-ion diffusion is found for the low-dimensional-networked Br-based materials (4.81×10^{-9} and 6.08×10^{-9} cm^2 s^{-1} for Li_5OBr_3 and Li_6OBr_4 at 300 K, respectively) compared to their Cl-based counterparts (9.85×10^{-10} and 2.06×10^{-9} $cm^{2\ s-1}$ for Li_5OCl_3 and Li_6OCl_4 at 300 K, respectively), showing the impact of lattice polarisability in these soft and unstable materials.

The study of anti-perovskites was expanded to cover not only Li-ion based materials but also Na-based systems in Chapter 5. DFT calculations were used to investigate the bulk and the surfaces of a range of M_3OX (M = Li or Na; X = Cl or Br) anti-perovskites, providing important information regarding their defect chemistry, electronic properties and ionic migration mechanisms.

The results presented in Chapter 5 show that (100) surfaces with metal-halide terminations are the most thermodynamically stable surface type for all analysed systems. The calculations also reveal that the most preferable vacancy type and site are the same for all investigated systems, showing that the Li/Na vacancy at the first layer of the supercell is the most energetically favourable defect type for all systems. The simulations also show that the formation of any defect type at any sites is more energetically favourable in systems containing Na instead of Li, regardless of their halide content, suggesting that the choice of the cation has a greater impact on defect formation at the surfaces of the investigated anti-perovskite systems compared to the choice of halide.

The migration energy barriers results discussed in Chapter 5 illustrate the importance of accounting for the free lattice space between metal sites when designing new SE materials,

with the results suggesting the existence of a trade-off between choosing highly polarisable atoms and losing critical free space in the lattice for ionic migration. The results presented show that although the ionic migration barrier simulations predict that Na_3OCl is the most promising SE candidate among the analysed systems, the analysis of the electronic properties reveals that the Na-based systems could potentially present lower electrochemical stabilities and higher propensity for dendrites formation. Furthermore, the results focused on Li_3OCl and Li_3OBr suggest that mixed halide SEs (e.g., $Li_3OCl_{0.5}Br_{0.5}$) could be an interesting direction for further studies focused on Li-based anti-perovskite SEs, especially if the maintenance of the Br-containing layers at the surface is possible.

Additionally, the work presented in this Thesis illustrates how computational modelling can be used to obtain important information in terms of electrochemical stability, structural impacts, defect chemistry, ionic migration mechanisms and dendrites propensity at the bulk and at the surfaces of anti-perovskite systems. Therefore, this work contributes greatly to the SSB field, especially regarding future interfacial studies that choose to use anti-perovskite structures as their SE.

Moreover, the results herein presented can potentially guide and assist future experimental synthesis directions, resulting in more successful synthesis attempts with improved time and resource consumption. Considering the critical importance of SEs in the development of SSBs and the unique potential of anti-perovskite SEs, the results presented in this Thesis contribute greatly to the battery community and to further advances in the fields SSBs and energy storage.

6.2 Future Work

This Thesis explores the relevant properties, defect chemistry, electrochemical stabilities, dendrite propensity and ionic transport mechanisms in a range of Li- and Na-based

anti-perovskite materials. The work presented here not only provides valuable insights regarding the potential of these SE candidates for future applications but also suggests a plethora of interesting possibilities for future research directions.

Further studies could build on the work presented in Chapter 4 by expanding it to include the surfaces of the targeted low-DN anti-perovskite systems, as well as their Na-, K-, Ca- and Mg-based analogues. As discussed in Chapter 2, anti-perovskites based on such chemistries offer an intriguing research path due to their wide availability. It would be interesting to investigate whether the trends revealed by the work presented in Chapter 4 would also be seen at such surfaces and systems. Additionally, a further study could assess the similarity between the results presented in Chapter 4 and DFT- and ML force field-based results that investigated the same systems, offering a comparison between classical, DFT and ML-based methods.

A natural progression of the work presented in Chapter 5 would be to conduct an analysis of electronic properties displayed by defective systems and surfaces and confirm whether the electrochemical stability and dendrite propensity found for pristine Na-based systems would still be present in their defective analogues. Further computational and experimental investigations could also be employed to investigate whether the presence of coatings could be beneficial to improve the electrochemical stability and lower the dendrite propensity displayed by these Na-based materials.

Considering the hindering effect interfacial issues have on the performance of SSBs, an interesting progression of the work presented in Chapter 5 could be the exploration of the analysed surfaces in interfacial electrolyte-anode systems (e.g., metallic Li/Na anodes and Li/Na-based anti-perovskite SEs), especially if such studies utilised ML force fields for interfacial explorations. As discussed in Chapter 2, the use of ML force fields for interfacial explorations is widely expected to enable the analysis of much more complex and larger simulation cells and time scales while retaining DFT-levels of accuracy, which will be key for

allowing for the design of stable conducting interfaces in which practical SSBs can be built on.

Despite the considerable body of work existent focused on anti-perovskite materials and the work presented in this Thesis, there are still many unanswered questions regarding the behaviour and potential of anti-perovskite systems for SE applications. Nevertheless, the recent progress in the anti-perovskite field and the results herein contained clearly demonstrate the excellent potential anti-perovskite materials have in contributing to the revolution in energy storage that SSBs are expected to lead.

References

1 Department for Transport, Transport and environment statistics, Official Statistics Transport and environment statistics: Autumn 2021, 2021, Available at https://www.gov.uk/government/statistics/transport-and-environment-statistics-autumn-2021/transport-and-environment-statistics-autumn-2021 (accessed 13 July 2024).

2 A. Browne, Pathway for zero emission vehicle transition by 2035 becomes law, *UK Dep. Transp. Off. Zero Emiss. Veh.*, 2024, 3–8.

3 H. T.-L. Y. M. Ydersbond, N. B. Kristensen, Nordic Sustainable Aviation, *Nord. Counc. Minist.*, 2020, **4**, 1–23.

4 M. Frederiksens, Statsminister Mette Frederiksens Nytårstale 2023, 2023, 1–9.

5 F. M. of T. and Communications, Government decided on measures to reduce greenhouse gas emissions from aviation – focus on renewable aviation fuels and carbon pricing, 2024, 3–5.

6 E. C. Evarts, Lithium batteries: To the limits of lithium, *Nature*, 2015, **526**, S93–S95.

7 J. A. Dawson, T. Famprikis and K. E. Johnston, Anti-perovskites for solid-state batteries: recent developments, current challenges and future prospects, *J. Mater. Chem. A*, 2021, **9**, 18746–18772.

8 T. Famprikis, P. Canepa, J. A. Dawson, M. S. Islam and C. Masquelier, Fundamentals

of inorganic solid-state electrolytes for batteries, *Nat. Mater.*, 2019, **18**, 1278–1291.

9 A. Masias, J. Marcicki and W. A. Paxton, Opportunities and Challenges of Lithium Ion Batteries in Automotive Applications, *ACS Energy Lett.*, 2021, **6**, 621–630.

10 N. Nitta, F. Wu, J. T. Lee and G. Yushin, Li-ion battery materials: Present and future, *Mater. Today*, 2015, **18**, 252–264.

11 H. Pan, Y. S. Hu and L. Chen, Room-temperature stationary sodium-ion batteries for large-scale electric energy storage, *Energy Environ. Sci.*, 2013, **6**, 2338–2360.

12 B. Dunn, H. Kamath and J. M. Tarascon, Electrical energy storage for the grid: A battery of choices, *Science*, 2011, **334**, 928–935.

13 M. A. J. M. Tarascon, Issues and challenges facing rechargeable lithium batteries, *Nature*, 2001, **414**, 359–367.

14 M. V. Reddy, A. Mauger, C. M. Julien, A. Paolella and K. Zaghib, Brief History of Early Lithium-Battery Development, *Materials*, 2020, **13**, 1–9.

15 C. Gustafsson, G. von Heijne, S. S. Linse and the N. C. for Chemistry, The Nobel Prize in Chemistry 2019: They developed the world's most powerful battery, *R. Swedish Acad. Sci.*, 2019, **8,** 1-7.

16 M. S. Whittingham, Electrical Energy Storage and Intercalation Chemistry, *Science*, 1976, **192**, 1126–1127.

17 K. Mizushima, P. C. Jones, P. J. Wiseman and J. B. Goodenough, Li_xCoO_2 ($0<x<-1$): A new cathode material for batteries of high energy density, *Mater. Res. Bull.*, 1980, **15**, 783–789.

18 A. Yoshino, The birth of the lithium-ion battery, *Angew. Chemie - Int. Ed.*, 2012, **51**, 5798–5800.

19 P. Huang, Q. Wang, K. Li, P. Ping and J. Sun, The combustion behavior of large scale lithium titanate battery, *Sci. Reports*, 2015, **5**, 1–12.

20 K. M. Abraham, How Comparable Are Sodium-Ion Batteries to Lithium-Ion Counterparts?, *ACS Energy Lett.*, 2020, **5**, 3544–3547.

21 A. S. Nagelberg and W. L. Worrell, A thermodynamic study of sodium-intercalated TaS_2 and TiS_2, *J. Solid State Chem.*, 1979, **29**, 345–354.

22 M. S. Whittingham, Chemistry of intercalation compounds: Metal guests in chalcogenide hosts, *Prog. Solid State Chem.*, 1978, **12**, 41–99.

23 C. Delmas, J. J. Braconnier, C. Fouassier and P. Hagenmuller, Electrochemical intercalation of sodium in Na_xCoO_2 bronzes, *Solid State Ionics*, 1981, **3**–**4**, 165–169.

24 L. W. Shacklette, T. R. Jow and L. Townsend, Rechargeable Electrodes from Sodium Cobalt Bronzes, *J. Electrochem. Soc.*, 1988, **135**, 2669–2674.

25 J. M. Tarascon and G. W. Hull, Sodium intercalation into the layer oxides $Na_xMo_2O_4$, *Solid State Ionics*, 1986, **22**, 85–96.

26 T. R. Jow, L. W. Shacklette, M. Maxfield and D. Vernick, Role of conductive polymers in alkali-metal secondary electrodes, *J. Electrochem. Soc.*, 1987, **134**, 1730-1733.

27 K. West, B. Zachau-Christiansen, T. Jacobsen and S. Skaarup, Sodium insertion in vanadium oxides, *Solid State Ionics*, 1988, **28**–**30**, 1128–1131.

28 B. L. Ellis, K. T. Lee and L. F. Nazar, Positive electrode materials for Li-Ion and Li-batteries, *Chem. Mater.*, 2010, **22**, 691–714.

29 M. Sawicki and L. L. Shaw, Advances and challenges of sodium ion batteries as post lithium ion batteries, *RSC Adv.*, 2015, **5**, 53129–53154.

30 Y. Zhao, Y. Kang, J. Wozny, J. Lu, H. Du, C. Li, T. Li, F. Kang, N. Tavajohi and B. Li, Recycling of sodium-ion batteries, *Nat. Rev. Mater.*, 2023, **8**, 623–634.

31 F. C. for A. Batteries, Executive Summary National Blueprint for Lithium Batteries 2021-2030, *FCAB*, 2021, 1–38.

32 H. U. Sverdrup, Modelling global extraction, supply, price and depletion of the extractable geological resources with the LITHIUM model, *Resour. Conserv. Recycl.*, 2016, **114**, 112–129.

33 P. Slowik, N. Lutsey and C.-W. Hsu, How technology, recycling, and policy can mitigate supply risks to the long-term transition to zero-emission vehicles, The International Council on Clean Transportation, 2020, 1–54.

34 H. Kim, H. Kim, Z. Ding, M. H. Lee, K. Lim, G. Yoon and K. Kang, Recent Progress in Electrode Materials for Sodium-Ion Batteries, *Adv. Energy Mater.*, 2016, **6**, 1–38.

35 H. Vikström, S. Davidsson and M. Höök, Lithium availability and future production outlooks, *Appl. Energy*, 2013, **110**, 252–266.

36 P. W. Gruber, P. A. Medina, G. A. Keoleian, S. E. Kesler, M. P. Everson and T. J. Wallington, Global Lithium Availability, *J. Ind. Ecol.*, 2011, **15**, 760–775.

37 E. Fan, L. Li, Z. Wang, J. Lin, Y. Huang, Y. Yao, R. Chen and F. Wu, Sustainable Recycling Technology for Li-Ion Batteries and Beyond: Challenges and Future Prospects, *Chem. Rev.*, 2020, **120**, 7020–7063.

38 Z. J. Baum, R. E. Bird, X. Yu and J. Ma, Lithium-Ion Battery Recycling─Overview of Techniques and Trends, *ACS Energy Lett.*, 2022, **7**, 712–719.

39 Faraday Insights and The Faraday Institution, Solid-State Batteries: The Technology of the 2030s but the Research Challenge of the 2020s, *Faraday Inst.*, 2020, **1**, 1–8.

40 N. Winton, Solid-State Batteries Promise Electric Car Popularity Boost, But Technical

Mountains Await, Forbes, 2021, Available at https://www.forbes.com/sites/neilwinton/2021/11/28/solid-state-batteries-promise-electric-car-popularity-boost-but-technical-mountains-await/?sh=59e74b34632f, (accessed 12 August 2024).

41 M. Pasta, D. Armstrong, Z. L. Brown, J. Bu, M. R. Castell, P. Chen, A. Cocks, S. A. Corr, E. J. Cussen, E. Darnbrough, V. Deshpande, C. Doerrer, M. S. Dyer, H. El-Shinawi, N. Fleck, P. Grant, G. L. Gregory, C. Grovenor, L. J. Hardwick, J. T. S. Irvine, H. J. Lee, G. Li, E. Liberti, I. McClelland, C. Monroe, P. D. Nellist, P. R. Shearing, E. Shoko, W. Song, D. S. Jolly, C. I. Thomas, S. J. Turrell, M. Vestli, C. K. Williams, Y. Zhou and P. G. Bruce, 2020 roadmap on solid-state batteries, *J. Phys. Energy*, 2020, **2**, 032008.

42 P. Verma, The race to a build solid-state battery for electric cars, Washington Post, 2022, Available at https://www.washingtonpost.com/technology/2022/05/18/solid-state-batteries-electric-vehicles-race/ (accessed 13 August 2024).

43 M. Marisch, Industry heavyweights look to solid-state battery cells, resources, and recycling – pv magazine International, 2022, Available at https://www.pv-magazine.com/2022/01/27/industry-heavyweights-look-to-solid-state-battery-cells-resources-and-recycling/ (accessed 13 August 2024).

44 M. Robinson, Nissan gives first look at prototype production plant for solid-state batteries, Auto Express, 2022, Available at https://www.autoexpress.co.uk/nissan/357742/nissan-gives-first-look-prototype-production-plant-solid-state-batteries, (accessed 13 August 2024).

45 L. Wilkinson, Honda to be electric only by 2040 with solid state battery tech coming late 2020s, Auto Express, 2021, Available at https://www.autoexpress.co.uk/honda/354834/honda-be-electric-only-2040-solid-state-battery-tech-coming-late-2020s (accessed 13 August 2024).

46 C. Li, Z. Yu Wang, Z. Jiang He, Y. Jiao Li, J. Mao, K. Hua Dai, C. Yan and J. Chao Zheng, An advance review of solid-state battery: Challenges, progress and prospects, *Sustain. Mater. Technol.*, 2021, **29**, e00297.

47 J. A. Lewis, J. Tippens, F. J. Q. Cortes and M. T. McDowell, Chemo-Mechanical Challenges in Solid-State Batteries, *Trends Chem.*, 2019, **1**, 845–857.

48 J. Janek and W. G. Zeier, A solid future for battery development, *Nat. Energy*, 2016, **1**.

49 Q. Zhao, S. Stalin, C. Z. Zhao and L. A. Archer, Designing solid-state electrolytes for safe, energy-dense batteries, *Nat. Rev. Mater.*, 2020, **5**, 229–252.

50 K. Kerman, A. Luntz, V. Viswanathan, Y.-M. Chiang and Z. Chen, Review—Practical Challenges Hindering the Development of Solid State Li Ion Batteries, *J. Electrochem. Soc.*, 2017, **164**, A1731–A1744.

51 S. Xia, X. Wu, Z. Zhang, Y. Cui and W. Liu, Practical Challenges and Future Perspectives of All-Solid-State Lithium-Metal Batteries, *Chem*, 2019, **5**, 753–785.

52 D. H. S. Tan, P. Xu, H. Yang, M. Cheol Kim, H. Nguyen, E. A. Wu, J. M. Doux, A. Banerjee, Y. S. Meng and Z. Chen, Sustainable design of fully recyclable all solid-state batteries, *MRS Energy Sustain.*, 2020, **7**, E23.

53 Y. Su, L. Ye, W. Fitzhugh, Y. Wang, E. Gil-González, I. Kim and X. Li, A more stable lithium anode by mechanical constriction for solid state batteries, *Energy Environ. Sci.*, 2020, **13**, 908–916.

54 Y. Kato, S. Hori and R. Kanno, $Li_{10}GeP_2S_{12}$-Type Superionic Conductors: Synthesis, Structure, and Ionic Transportation, *Adv. Energy Mater.*, 2020, **10**, 2002153.

55 S. Wenzel, S. Randau, T. Leichtweiß, D. A. Weber, J. Sann, W. G. Zeier and J. Janek, Direct Observation of the Interfacial Instability of the Fast Ionic Conductor

$Li_{10}GeP_2S_{12}$ at the Lithium Metal Anode, *Chem. Mater.*, 2016, **28**, 2400–2407.

56 X. Li, J. Liang, J. Luo, M. Norouzi Banis, C. Wang, W. Li, S. Deng, C. Yu, F. Zhao, Y. Hu, T. K. Sham, L. Zhang, S. Zhao, S. Lu, H. Huang, R. Li, K. R. Adair and X. Sun, Air-stable Li_3InCl_6 electrolyte with high voltage compatibility for all-solid-state batteries, *Energy Environ. Sci.*, 2019, **12**, 2665–2671.

57 Y. Kim and S. Choi, Investigation of the effect of F-doping on the solid-electrolyte property of Li_3InCl_6, *J. Power Sources*, 2023, **567**, 232962.

58 P. Canepa, J. A. Dawson, G. Sai Gautam, J. M. Statham, S. C. Parker and M. S. Islam, Particle Morphology and Lithium Segregation to Surfaces of the $Li_7La_3Zr_2O_{12}$ Solid Electrolyte, *Chem. Mater.*, 2018, **30**, 3019–3027.

59 C. Wang, K. Fu, S. P. Kammampata, D. W. McOwen, A. J. Samson, L. Zhang, G. T. Hitz, A. M. Nolan, E. D. Wachsman, Y. Mo, V. Thangadurai and L. Hu, Garnet-Type Solid-State Electrolytes: Materials, Interfaces, and Batteries, *Chem. Rev.*, 2020, **120**, 4257–4300.

60 Z. Lu, J. Liu and F. Ciucci, Superionic conduction in low-dimensional-networked anti-perovskites, *Energy Storage Mater.*, 2020, **28**, 146–152.

61 A. C. C. Dutra and J. A. Dawson, Computational Design of Antiperovskite Solid Electrolytes, *J. Phys. Chem. C*, 2023, **127**, 18256–18270.

62 Y. Zhao and L. L. Daemen, Superionic conductivity in lithium-rich anti-perovskites, *J. Am. Chem. Soc.*, 2012, **134**, 15042–15047.

63 X. Lü, J. W. Howard, A. Chen, J. Zhu, S. Li, G. Wu, P. Dowden, H. Xu, Y. Zhao and Q. Jia, Antiperovskite Li_3OCl superionic conductor films for solid-state li-ion batteries, *Adv. Sci.*, 2016, **3**, 1500359.

64 H. Fang and P. Jena, Li-rich antiperovskite superionic conductors based on cluster ions,

Proc. Natl. Acad. Sci. U. S. A., 2017, **114**, 11046–11051.

65 J. A. S. Serejo, J. S. Pereira, R. Mouta and L. G. C. Rego, Sluggish anion transport provides good kinetic stability to the anhydrous anti-perovskite solid electrolyte Li_3OCl, *Phys. Chem. Chem. Phys.*, 2021, **23**, 6964–6973.

66 J. A. Dawson, P. Canepa, T. Famprikis, C. Masquelier and M. S. Islam, Atomic-Scale Influence of Grain Boundaries on Li-Ion Conduction in Solid Electrolytes for All-Solid-State Batteries, *J. Am. Chem. Soc.*, 2018, **140**, 362–368.

67 Y. Li, W. Zhou, S. Xin, S. Li, J. Zhu, L. Xujie, Z. Cui, Q. Jia, J. Zhou, Y. Zhao and J. B. Goodenough, Fluorine-Doped Antiperovskite Electrolyte for All-Solid-State Lithium-Ion Batteries, *Angew. Chemie - Int. Ed.*, 2016, **55**, 9965–9968.

68 S. Gao, T. Broux, S. Fujii, C. Tassel, K. Yamamoto, Y. Xiao, I. Oikawa, H. Takamura, H. Ubukata, Y. Watanabe, K. Fujii, M. Yashima, A. Kuwabara, Y. Uchimoto and H. Kageyama, Hydride-based antiperovskites with soft anionic sublattices as fast alkali ionic conductors, *Nat. Commun.*, 2021, **12**, 1–10.

69 K. Kim and D. J. Siegel, Correlating lattice distortions, ion migration barriers, and stability in solid electrolytes, *J. Mater. Chem. A*, 2019, **7**, 3216–3227.

70 Z. Deng, B. Radhakrishnan and S. P. Ong, Rational composition optimization of the lithium-rich $Li_3OCl_{1-x}Br_x$ anti-perovskite superionic conductors, *Chem. Mater.*, 2015, **27**, 3749–3755.

71 J. A. Dawson, H. Chen and M. Saiful Islam, Composition Screening of Lithium- and Sodium-Rich Anti-Perovskites for Fast-Conducting Solid Electrolytes, *J. Phys. Chem. C*, 2018, **122**, 23978–23984.

72 Y. Yu, Z. Wang and G. Shao, Theoretical tuning of Ruddlesden–Popper type anti-

perovskite phases as superb ion conductors and cathodes for solid sodium ion batteries, *J. Mater. Chem. A*, 2019, **7**, 10483–10493.

73 R. Jalem, Y. Tateyama, K. Takada and M. Nakayama, First-Principles DFT Study on Inverse Ruddlesden–Popper Tetragonal Compounds as Solid Electrolytes for All-Solid-State Li^+-Ion Batteries, *Chem. Mater.*, 2021, 33, **15**, 5859–5871.

74 H. Fang, S. Wang, J. Liu, Q. Sun and P. Jena, Superhalogen-based lithium superionic conductors, *J. Mater. Chem. A*, 2017, **5**, 13373–13381.

75 H. Fang and P. Jena, Sodium Superionic Conductors Based on Clusters, *ACS Appl. Mater. Interfaces*, 2019, **11**, 963–972.

76 Z. Xu, Y. Liu, X. Sun, X. Xie, X. Guan, C. Chen, P. Lu and X. Ma, Theoretical design of Na-rich anti-perovskite as solid electrolyte: The effect of cluster anion in stability and ionic conductivity, *J. Solid State Chem.*, 2022, **316**, 123643.

77 H. K. Singh, Z. Zhang, I. Opahle, D. Ohmer, Y. Yao and H. Zhang, High-Throughput Screening of Magnetic Antiperovskites, *Chem. Mater.*, 2018, **30**, 6983–6991.

78 J. I. Gómez – Peralta and X. Bokhimi, Discovering new perovskites with artificial intelligence, *J. Solid State Chem.*, 2020, **285**, 121253.

79 G. H. Gu, J. Jang, J. Noh, A. Walsh and Y. Jung, Perovskite synthesizability using graph neural networks, *npj Comput. Mater. 2022 81*, 2022, **8**, 1–8.

80 J. Wang and V. Saligrama, Local Supervised Learning through Space Partitioning, *Adv. Neural Inf. Process. Syst.*, 2012, **25**, 1-9.

81 H. Oiwa and R. Fujimaki, Partition-wise Linear Models, *Adv. Neural Inf. Process. Syst.*, 2014, **27**, 1-9.

82 C. J. Bartel, C. Sutton, B. R. Goldsmith, R. Ouyang, C. B. Musgrave, L. M. Ghiringhelli and M. Scheffler, New tolerance factor to predict the stability of perovskite oxides and halides, *Sci. Adv.*, 2019, 2, **5**, eaav0693.

83 S. Lu, Q. Zhou, L. Ma, Y. Guo and J. Wang, Rapid Discovery of Ferroelectric Photovoltaic Perovskites and Material Descriptors via Machine Learning, *Small Methods*, 2019, **3**, 1900360.

84 G. Pilania, P. V. Balachandran, C. Kim and T. Lookman, Finding new perovskite halides via machine learning, *Front. Mater.*, 2016, **3**, 195497.

85 H. Liu, J. Cheng, H. Dong, J. Feng, B. Pang, Z. Tian, S. Ma, F. Xia, C. Zhang and L. Dong, Screening stable and metastable ABO_3 perovskites using machine learning and the materials project, *Comput. Mater. Sci.*, 2020, **177**, 109614.

86 B. H. Sjølin, P. B. Jørgensen, A. Fedrigucci, T. Vegge, A. Bhowmik and I. E. Castelli, Accelerated Workflow for Antiperovskite-based Solid State Electrolytes, *Batter. Supercaps*, 2023, **6**, e202300041.

87 N. R. Mathiesen, H. Jónsson, T. Vegge and J. M. García Lastra, R-NEB: Accelerated Nudged Elastic Band Calculations by Use of Reflection Symmetry, *J. Chem. Theory Comput.*, 2019, **15**, 3215–3222.

88 J. H. Chang, P. B. Jørgensen, S. Loftager, A. Bhowmik, J. M. G. Lastra and T. Vegge, On-the-fly assessment of diffusion barriers of disordered transition metal oxyfluorides using local descriptors, *Electrochim. Acta*, 2021, **388**, 138551.

89 K. Kim, Y. Li, P. C. Tsai, F. Wang, S. B. Son, Y. M. Chiang and D. J. Siegel, Exploring the Synthesis of Alkali Metal Anti-perovskites, *Chem. Mater.*, 2022, **34**, 947–958.

90 G. Kieslich, S. Sun and A. K. Cheetham, Solid-state principles applied to organic–inorganic perovskites: new tricks for an old dog, *Chem. Sci.*, 2014, **5**, 4712–4715.

91 A. G. Squires, J. M. Dean and B. J. Morgan, Aliovalent doping response and impact on ionic conductivity in the antiperovskite solid electrolyte Li_3OCl, ChemRxiv, 2021.

92 B. A. Goldmann, M. J. Clarke, J. A. Dawson and M. S. Islam, Atomic-scale investigation of cation doping and defect clustering in the anti-perovskite Na_3OCl sodium-ion conductor, *J. Mater. Chem. A*, 2022, **10**, 2249–2255.

93 M. J. Clarke, J. A. Dawson, T. J. Mays and M. S. Islam, Atomistic insights into the effects of doping and vacancy clustering on li-ion conduction in the Li_3OCl antiperovskite solid electrolyte, *ACS Appl. Energy Mater.*, 2021, **4**, 5094–5100.

94 T. H. Wan, Z. Lu and F. Ciucci, A first principle study of the phase stability, ion transport and substitution strategy for highly ionic conductive sodium antipervoskite as solid electrolyte for sodium ion batteries, *J. Power Sources*, 2018, **390**, 61–70.

95 A. Emly, E. Kioupakis and A. Van Der Ven, Phase stability and transport mechanisms in antiperovskite Li_3OCl and Li_3OBr superionic conductors, *Chem. Mater.*, 2013, **25**, 4663–4670.

96 S. Stegmaier, J. Voss, K. Reuter and A. C. Luntz, Li+ Defects in a Solid-State Li Ion Battery: Theoretical Insights with a Li_3OCl Electrolyte, *Chem. Mater.*, 2017, **29**, 4330–4340.

97 M. H. Chen, A. Emly and A. Van Der Ven, Anharmonicity and phase stability of antiperovskite Li_3OCl, *Phys. Rev. B - Condens. Matter Mater. Phys.*, 2015, **91**, 214306.

98 R. Mouta, E. M. Diniz and C. W. A. Paschoal, Li+ interstitials as the charge carriers in superionic lithium-rich anti-perovskites, *J. Mater. Chem. A*, 2016, **4**, 1586–1590.

99 S. Zhao, C. Chen, H. Li and W. Zhang, Theoretical insights into the diffusion mechanism of alkali ions in Ruddlesden-Popper antiperovskites, *New J. Chem.*, 2021, **45**, 4219–4226.

100 J. G. Smith and D. J. Siegel, Low-temperature paddlewheel effect in glassy solid electrolytes, *Nat. Commun.*, 2020, **11**, 1–11.

101 X. He, Y. Zhu and Y. Mo, Origin of fast ion diffusion in super-ionic conductors, *Nat. Commun.*, 2017, **8**, 1–7.

102 R. Jalem, Y. Yamamoto, H. Shiiba, M. Nakayama, H. Munakata, T. Kasuga and K. Kanamura, Concerted migration mechanism in the Li-ion dynamics of garnet-type $Li_7La_3Zr_2O_{12}$, *Chem. Mater.*, 2013, **25**, 425–430.

103 A. M. Nolan, Y. Zhu, X. He, Q. Bai and Y. Mo, Computation-Accelerated Design of Materials and Interfaces for All-Solid-State Lithium-Ion Batteries, *Joule*, 2018, **2**, 2016–2046.

104 A. D. Poletayev, J. A. Dawson, M. S. Islam and A. M. Lindenberg, Defect-driven anomalous transport in fast-ion conducting solid electrolytes, *Nat. Mater.*, 2022, **21**, 1066–1073.

105 R. Mouta, M. Á. B. Melo, E. M. Diniz and C. W. A. Paschoal, Concentration of charge carriers, migration, and stability in Li_3OCl solid electrolytes, *Chem. Mater.*, 2014, **26**, 7137–7144.

106 Z. Lu, C. Chen, Z. M. Baiyee, X. Chen, C. Niu and F. Ciucci, Defect chemistry and lithium transport in Li_3OCl anti-perovskite superionic conductors, *Phys. Chem. Chem. Phys.*, 2015, **17**, 32547–32555.

107 J. A. Dawson, T. S. Attari, H. Chen, S. P. Emge, K. E. Johnston and M. S. Islam, Elucidating Lithium-ion and proton dynamics in anti-perovskite solid electrolytes, *Energy Environ. Sci.*, 2018, **11**, 2993–3002.

108 P. C. Tsai, S. Mair, J. Smith, D. M. Halat, P. H. Chien, K. Kim, D. Zhang, Y. Li, L. Yin, J. Liu, S. H. Lapidus, J. A. Reimer, N. P. Balsara, D. J. Siegel and Y. M. Chiang, Double Paddle-Wheel Enhanced Sodium Ion Conduction in an Antiperovskite Solid Electrolyte, *Adv. Energy Mater.*, 2023, **13**, 2203284.

109 E. Ahiavi, J. A. Dawson, U. Kudu, M. Courty, M. S. Islam, O. Clemens, C. Masquelier and T. Famprikis, Mechanochemical synthesis and ion transport properties of Na_3OX (X = Cl, Br, I and BH_4) antiperovskite solid electrolytes, *J. Power Sources*, 2020, **471**, 228489.

110 R. Kanno and M. Murayama, Lithium Ionic Conductor Thio-LISICON: The Li_2S-GeS_2-P_2S_5 System, *J. Electrochem. Soc.*, 2001, **148**, A742.

111 M. A. Kraft, S. P. Culver, M. Calderon, F. Bo, T. Krauskopf, A. Senyshyn, C. Dietrich, A. Zevalkink, J. Janek and W. G. Zeier, Influence of Lattice Polarizability on the Ionic Conductivity in the Lithium Superionic Argyrodites Li_6PS_5X (X = Cl, Br, I), *J. Am. Chem. Soc.* 2017, 139, **31**, 10909–10918.

112 R. Jiang, C. Song, J. Yang, J. Zhao, F. Fang, Y. Song, D. Sun and F. Wang, Boosting the Na-Ion Conductivity in the Cluster-Ion Based Anti-Perovskite $Na_2BH_4NH_2$, *Adv. Funct. Mater.*, 2023, **33**, 2301635.

113 F. N. Forrester, J. A. Quirk, T. Famprikis and J. A. Dawson, Disentangling Cation and Anion Dynamics in Li_3PS_4 Solid Electrolytes, *Chem. Mater.*, 2022, **34**, 10561–10571.

114 A. Y. Song, Y. Xiao, K. Turcheniuk, P. Upadhya, A. Ramanujapuram, J. Benson, A. Magasinski, M. Olguin, L. Meda, O. Borodin and G. Yushin, Protons Enhance Conductivities in Lithium Halide Hydroxide/Lithium Oxyhalide Solid Electrolytes by Forming Rotating Hydroxy Groups, *Adv. Energy Mater.*, 2018, **8**, 1700971.

115 J. Howard, Z. D. Hood and N. A. W. Holzwarth, Fundamental aspects of the structural and electrolyte properties of Li_2OHCl from simulations and experiment, *Phys. Rev. Mater.*, 2017, **1**, 075406.

116 A. Y. Song, K. Turcheniuk, J. Leisen, Y. Xiao, L. Meda, O. Borodin and G. Yushin, Understanding Li-Ion Dynamics in Lithium Hydroxychloride (Li_2OHCl) Solid State Electrolyte via Addressing the Role of Protons, *Adv. Energy Mater.*, 2020, **10**, 1903480.

117 F. Wang, H. A. Evans, K. Kim, L. Yin, Y. Li, P. C. Tsai, J. Liu, S. H. Lapidus, C. M. Brown, D. J. Siegel and Y. M. Chiang, Dynamics of Hydroxyl Anions Promotes Lithium Ion Conduction in Antiperovskite Li_2OHCl, *Chem. Mater.*, 2020, **32**, 8481–8491.

118 K. Kim and D. J. Siegel, Machine learning reveals factors that control ion mobility in anti-perovskite solid electrolytes, *J. Mater. Chem. A*, 2022, **10**, 15169–15182.

119 Z. Zhang, Y. Shao, B. Lotsch, Y. S. Hu, H. Li, J. Janek, L. F. Nazar, C. W. Nan, J. Maier, M. Armand and L. Chen, New horizons for inorganic solid state ion conductors, *Energy Environ. Sci.*, 2018, **11**, 1945–1976.

120 H. Tsukasaki, S. Mori, H. Morimoto, A. Hayashi and M. Tatsumisago, Direct observation of a non-crystalline state of Li_2S–P_2S_5 solid electrolytes, *Sci. Reports*, 2017, **7**, 1–7.

121 C. Ma, K. Chen, C. Liang, C. W. Nan, R. Ishikawa, K. More and M. Chi, Atomic-scale origin of the large grain-boundary resistance in perovskite Li-ion-conducting solid electrolytes, *Energy Environ. Sci.*, 2014, **7**, 1638–1642.

122 A. R. Symington, M. Molinari, J. A. Dawson, J. M. Statham, J. Purton, P. Canepa and S. C. Parker, Elucidating the nature of grain boundary resistance in Lithium Lanthanum titanate, *J. Mater. Chem. A*, 2021, **9**, 6487–6498.

123 E. Milan and M. Pasta, The role of grain boundaries in solid-state Li-metal batteries, *Mater. Futur.*, 2023, 1, **2**, 013501.

124 B. Chen, C. Xu and J. Zhou, Insights into Grain Boundary in Lithium-Rich Anti-Perovskite as Solid Electrolytes, *J. Electrochem. Soc.*, 2018, **165**, A3946–A3951.

125 K. Shen, Y. Wang, J. Zhang, Y. Zong, G. Li, C. Zhao and H. Chen, Revealing the effect of grain boundary segregation on Li-ion transport in polycrystalline anti-perovskite Li_3ClO: A phase field study, *Phys. Chem. Chem. Phys.*, 2020, **22**, 3030–3036.

126 H. J. Lee, B. Darminto, S. Narayanan, M. Diaz-Lopez, A. W. Xiao, Y. Chart, J. H. Lee, J. A. Dawson and M. Pasta, Li-ion conductivity in $Li_2OHCl_{1-x}Br_x$ solid electrolytes: grains, grain boundaries and interfaces, *J. Mater. Chem. A*, 2022, **10**, 11574–11586.

127 J. A. Quirk and J. A. Dawson, Design Principles for Grain Boundaries in Solid-State Lithium-Ion Conductors, 2022, **13**, 2301114.

128 K. Kim and D. J. Siegel, Predicting Wettability and the Electrochemical Window of Lithium-Metal/Solid Electrolyte Interfaces, *ACS Appl. Mater. Interfaces*, 2019, **11**, 39940–39950.

129 S.-H. Choe, W.-H. Hong, K.-C. Kim and C.-J. Yu, Insight into the structural and electrochemical properties of the interface between a Na_6SOI_2 solid electrolyte and a metallic Na anode , *Phys. Chem. Chem. Phys.*, 2023, **12**, 8544–8555.

130 M. Wu, B. Xu, W. Luo, B. Sun, J. Shi and C. Ouyang, First-principles study on the structural, electronic, and Li-ion mobility properties of anti-perovskite superionic conductor Li_3OCl (1 0 0) surface, *Appl. Surf. Sci.*, 2020, **510**, 145394.

131 W. D. Richards, L. J. Miara, Y. Wang, J. C. Kim and G. Ceder, Interface Stability in Solid-State Batteries, *Chem. Mater.*, 2016, **28**, 266–273.

132 Y. Xiao, Y. Wang, S. H. Bo, J. C. Kim, L. J. Miara and G. Ceder, Understanding interface stability in solid-state batteries, *Nat. Rev. Mater.*, 2020, **5**, 105–126.

133 V. Lacivita, Y. Wang, S. H. Bo and G. Ceder, Ab initio investigation of the stability of electrolyte/electrode interfaces in all-solid-state Na batteries, *J. Mater. Chem. A*, 2019, **7**, 8144–8155.

134 J. Zheng, H. Fang, L. Fan, Y. Ren, P. Jena and Y. Wu, Antiperovskite K_3OI for K-Ion Solid State Electrolyte, *J. Phys. Chem. Lett.*, 2021, **12**, 7120–7126.

135 K. Kim and D. J. Siegel, Multivalent Ion Transport in Anti-Perovskite Solid Electrolytes, *Chem. Mater.*, 2021, **33**, 2187–2197.

136 V. L. Deringer, Modelling and understanding battery materials with machine-learning-driven atomistic simulations, *J. Phys. Energy*, 2020, **2**, 041003.

137 A. Bhowmik, M. Berecibar, M. Casas-Cabanas, G. Csanyi, R. Dominko, K. Hermansson, M. R. Palacin, H. S. Stein and T. Vegge, Implications of the BATTERY 2030+ AI-Assisted Toolkit on Future Low-TRL Battery Discoveries and Chemistries, *Adv. Energy Mater.*, 2022, **12**, 2102698.

138 Y. Shao, L. Knijff, F. M. Dietrich, K. Hermansson and C. Zhang, Modelling Bulk Electrolytes and Electrolyte Interfaces with Atomistic Machine Learning, *Batter. Supercaps*, 2021, **4**, 585–595.

139 A. R. . Leach, *Molecular modelling : principles and applications*, Prentice Hall, New Jersey, USA, 1996.

140 R. R. A. C. Catlow, *Computer Modelling in Inorganic Crystallography*, Academic Press, Cambridge, USA, 1997.

141 P. Cheetham, Anthony K.; Day, *Solid-State Chemistry Techniques*, Oxford Science Publications, Oxford, UK, 1987.

142 D. Frenkel and B. Smit, *Understanding molecular simulation : from algorithms to applications*, Academic Press, Cambridge, USA, 1996.

143 J. A. Sholl, D. S.; Steckel, *Density Functional Theory: A Practical Introduction*, Wiley, New Jersey, USA, 2009.

144 M. C. Koch, W.; Holthausen, *A Chemist's Guide to Density Functional Theory*, Wiley, New Jersey, USA, 2001.

145 J. D. Gale and A. L. Rohl, The General Utility Lattice Program (GULP), *Molecular simulation*, 2011, **29**, 291–341.

146 S. Plimpton, Plimpton and Steve, Fast Parallel Algorithms for Short-Range Molecular Dynamics, *JCoPh*, 1995, **117**, 1–19.

147 G. Kresse and J. Furthmüller, Efficient iterative schemes for *ab initio* total-energy calculations using a plane-wave basis set, *Phys. Rev. B*, 1996, **54**, 11169.

148 G. Kresse and D. Joubert, From ultrasoft pseudopotentials to the projector augmented-wave method, *Phys. Rev. B*, 1999, **59**, 1758.

149 M. Born, Volumen und Hydratationswärme der Ionen, *Zeitschrift für Phys.*, 1920, **1**, 45–48.

150 R. A. Buckingham, The classical equation of state of gaseous helium, neon and argon, *Proc. R. Soc. London. Ser. A. Math. Phys. Sci.*, 1938, **168**, 264–283.

151 P. M. Morse, Diatomic Molecules According to the Wave Mechanics. II. Vibrational Levels, *Phys. Rev.*, 1929, **34**, 57.

152 B. G. Dick and A. W. Overhauser, Theory of the Dielectric Constants of Alkali Halide Crystals, *Phys. Rev.*, 1958, **112**, 90.

153 N. F. Mott and M. J. Littleton, Conduction in polar crystals. I. Electrolytic conduction in solid salts, *Trans. Faraday Soc.*, 1938, **34**, 485–499.

154 M. S. Islam and C. A. J. Fisher, Lithium and sodium battery cathode materials: Computational insights into voltage, diffusion and nanostructural properties, *Chem. Soc. Rev.*, 2014, **43**, 185–204.

155 L. Verlet, Computer 'Experiments' on Classical Fluids. I. Thermodynamical Properties of Lennard-Jones Molecules, *Phys. Rev.*, 1967, **159**, 98.

156 H. C. Andersen, Molecular dynamics simulations at constant pressure and/or temperature, *J. Chem. Phys.*, 1980, **72**, 2384–2393.

157 H. J. C. Berendsen, J. P. M. Postma, W. F. Van Gunsteren, A. Dinola and J. R. Haak, Molecular dynamics with coupling to an external bath, *J. Chem. Phys.*, 1984, **81**, 3684–3690.

158 D. J. Evans, B. L. Holian, D. J. Evans and B. L. Holian, The Nose–Hoover thermostat, *J. Chem. Phys.*, 1998, **83**, 4069.

159 T. J. Pennycook, M. J. Beck, K. Varga, M. Varela, S. J. Pennycook and S. T. Pantelides, Origin of colossal ionic conductivity in oxide multilayers: Interface induced sublattice disorder, *Phys. Rev. Lett.*, 2010, **104**, 115901.

160 J. G. Swallow, W. H. Woodford, Y. Chen, Q. Lu, J. J. Kim, D. Chen, Y. M. Chiang, W. C. Carter, B. Yildiz, H. L. Tuller and K. J. Van Vliet, Chemomechanics of ionically conductive ceramics for electrical energy conversion and storage, *J. Electroceramics*, 2014, **32**, 3–27.

161 W. Kohn and L. J. Sham, Self-consistent equations including exchange and correlation effects, *Phys. Rev.*, 1965, **140**, A1133.

162 J. P. Perdew and A. Zunger, Self-interaction correction to density-functional approximations for many-electron systems, *Phys. Rev. B*, 1981, **23**, 5048.

163 J. P. Perdew, K. Burke and M. Ernzerhof, Generalized Gradient Approximation Made Simple, *Phys. Rev. Lett.*, 1996, **77**, 3865.

164 S. H. Vosko, L. Wilk and M. Nusair, Accurate spin-dependent electron liquid correlation energies for local spin density calculations: a critical analysis, *Can. J. Phys.*, 1980, **58**, 1200–1211.

165 P. J. Stephens, F. J. Devlin, C. F. Chabalowski and M. J. Frisch, Ab Initio calculation of vibrational absorption and circular dichroism spectra using density functional force fields, *J. Phys. Chem.*, 1994, **98**, 11623–11627.

166 C. Adamo and V. Barone, Toward reliable density functional methods without adjustable parameters: The PBE0 model, *J. Chem. Phys.*, 1999, **110**, 6158–6170.

167 J. Heyd, G. E. Scuseria and M. Ernzerhof, Hybrid functionals based on a screened Coulomb potential, *J. Chem. Phys.*, 2003, **118**, 8207–8215.

168 F. Bloch, Über die Quantenmechanik der Elektronen in Kristallgittern, *Zeitschrift für Phys.*, 1929, **52**, 555–600.

169 M. C. Payne, M. P. Teter, D. C. Allan, T. A. Arias and J. D. Joannopoulos, Iterative minimization techniques for *ab initio* total-energy calculations: molecular dynamics and conjugate gradients, *Rev. Mod. Phys.*, 1992, **64**, 1045.

170 H. J. Monkhorst and J. D. Pack, Special points for Brillouin-zone integrations, *Phys. Rev. B*, 1976, **13**, 5188.

171 P. E. Blöchl, Projector augmented-wave method, *Phys. Rev. B*, 1994, **50**, 17953.

172 W. Sun and G. Ceder, Efficient creation and convergence of surface slabs, *Surf. Sci.*, 2013, **617**, 53–59.

173 G. Henkelman and H. Jónsson, A dimer method for finding saddle points on high dimensional potential surfaces using only first derivatives, *J. Chem. Phys.*, 1999, **111**, 7010–7022.

174 G. T. Barkema and N. Mousseau, Event-Based Relaxation of Continuous Disordered Systems, *Phys. Rev. Lett.*, 1996, **77**, 4358.

175 N. Mousseau and G. T. Barkema, Traveling through potential energy landscapes of disordered materials: The activation-relaxation technique, *Phys. Rev. E*, 1998, **57**, 2419.

176 W. E, W. Ren and E. Vanden-Eijnden, String method for the study of rare events, *Phys. Rev. B - Condens. Matter Mater. Phys.*, 2002, **66**, 523011–523014.

177 B. Peters, A. Heyden, A. T. Bell and A. Chakraborty, A growing string method for determining transition states: Comparison to the nudged elastic band and string methods, *J. Chem. Phys.*, 2004, **120**, 7877–7886.

178 H. Jónsson, G. Mills and K. W. Jacobsen, *Classical and Quantum Dynamics in Condensed Phase Simulations*, World Scientific, Singapore, 1998, Chapter 6 - Nudged elastic band method for finding minimum energy paths of transitions, 385–404.

179 G. Henkelman, B. P. Uberuaga, H. Jónsson, G. Henkelman, B. P. Uberuaga and H. Jónsson, A climbing image nudged elastic band method for finding saddle points and minimum energy paths, *JChPh*, 2000, **113**, 9901–9904.

180 S. Smidstrup, A. Pedersen, K. Stokbro and H. Jónsson, Improved initial guess for minimum energy path calculations, *J. Chem. Phys.*, 2014, **140**, 214106.

181 D. Sheppard, R. Terrell and G. Henkelman, Optimization methods for finding minimum energy paths, *J. Chem. Phys.*, 2008, **128**, 134106.

182 X. Lü, G. Wu, J. W. Howard, A. Chen, Y. Zhao, L. L. Daemen and Q. Jia, Li-rich anti-perovskite Li_3OCl films with enhanced ionic conductivity, *Chem. Commun.*, 2014, **50**, 11520–11522.

183 S. Li, J. Zhu, Y. Wang, J. W. Howard, X. Lü, Y. Li, R. S. Kumar, L. Wang, L. L. Daemen and Y. Zhao, Reaction mechanism studies towards effective fabrication of lithium-rich anti-perovskites Li_3OX (X=Cl, Br), *Solid State Ionics*, 2015, **284**, 14–19.

184 I. Hanghofer, G. J. Redhammer, S. Rohde, I. Hanzu, A. Senyshyn, H. M. R. Wilkening and D. Rettenwander, Untangling the Structure and Dynamics of Lithium-Rich Anti-Perovskites Envisaged as Solid Electrolytes for Batteries, *Chem. Mater.*, 2018, **30**, 8134–8144.

185 A. Koedtruad, M. A. Patino, N. Ichikawa, D. Kan and Y. Shimakawa, Crystal structures and ionic conductivity in Li_2OHX (X = Cl, Br) antiperovskites, *J. Solid State Chem.*, 2020, **286**, 121263.

186 A. S. Bhalla, R. Guo and R. Roy, The perovskite structure - A review of its role in ceramic science and technology, *Mater. Res. Innov.*, 2000, **4**, 3–26.

187 J. A. Dias, S. H. Santagneli and Y. Messaddeq, Methods for Lithium Ion NASICON Preparation: From Solid-State Synthesis to Highly Conductive Glass-Ceramics, *J. Phys. Chem. C*, 2020, **124**, 26518–26539.

188 Y. Wang, Q. Wang, Z. Liu, Z. Zhou, S. Li, J. Zhu, R. Zou, Y. Wang, J. Lin and Y. Zhao, Structural manipulation approaches towards enhanced sodium ionic conductivity in Na-rich antiperovskites, *J. Power Sources*, 2015, **293**, 735–740.

189 J. Zhu, Y. Wang, S. Li, J. W. Howard, J. Neuefeind, Y. Ren, H. Wang, C. Liang, W. Yang, R. Zou, C. Jin and Y. Zhao, Sodium Ion Transport Mechanisms in Antiperovskite Electrolytes Na_3OBr and Na_4OI_2: An in Situ Neutron Diffraction Study, *Inorg. Chem.*, 2016, **55**, 5993–5998.

190 H. Nguyen, S. Hy, E. Wu, Z. Deng, M. Samiee, T. Yersak, J. Luo, S. Ping Ong and Y. Shirley Meng, Experimental and Computational Evaluation of a Sodium-Rich Anti-Perovskite for Solid State Electrolytes, *J. Electrochem. Soc.*, 2016, **163**, 2165–2171.

191 Z. Wang, H. Xu, M. Xuan and G. Shao, From anti-perovskite to double anti-perovskite: Tuning lattice chemistry to achieve super-fast Li+ transport in cubic solid lithium halogen-chalcogenides, *J. Mater. Chem. A*, 2017, **6**, 73–83.

192 Y. Zhang, Y. Zhao and C. Chen, Ab initio study of the stabilities of and mechanism of superionic transport in lithium-rich antiperovskites, *Phys. Rev. B - Condens. Matter Mater. Phys.*, 2013, **87**, 134303.

193 M. I. Saidaminov, O. F. Mohammed and O. M. Bakr, Low-dimensional-networked metal halide perovskites: The next big thing, *ACS Energy Lett.*, 2017, **2**, 889–896.

194 J. Zhu, S. Li, Y. Zhang, J. W. Howard, X. Lü, Y. Li, Y. Wang, R. S. Kumar, L. Wang and Y. Zhao, Enhanced ionic conductivity with $Li_7O_2Br_3$ phase in Li_3OBr anti-perovskite solid electrolyte, *Appl. Phys. Lett.*, 2016, **109**, 101904.

195 S. Wakazaki, Q. Liu, R. Jalem, T. Nishikubo, Y. Sakai, N. Matsui, G. Zhao, K. Suzuki, K. Shigematsu, T. Yamamoto, R. Kanno, H. Das, Y. Tateyama and M. Azuma, High-Pressure Synthesis and Lithium-Ion Conduction of Li_4OBr_2 Derivatives with a Layered Inverse-Perovskite Structure, *Chem. Mater.*, 2021, **33**, 9194–9201.

196 H. Sabrowsky, K. Paszkowski, D. Reddig and P. Vogt, Na_3OCl und Na_3OBr, die ersten Alkalimetallchalkogenidhalogenide Na_3OCl and Na_3OBr, the First Alkali Metal Chalcogenide Halides, *Z. Naturforsch*, 1988, **43**, 238–239.

197 S. M. Wood, C. Eames, E. Kendrick and M. S. Islam, Sodium Ion Diffusion and Voltage Trends in Phosphates $Na_4M_3(PO_4)_2P_2O_7$ (M = Fe, Mn, Co, Ni) for Possible High-Rate Cathodes, *J. Phys. Chem. C*, 2015, **119**, 15935–15941.

198 J. C. Treacher, S. M. Wood, M. S. Islam and E. Kendrick, Na_2CoSiO_4 as a cathode

material for sodium-ion batteries: structure, electrochemistry and diffusion pathways, *Phys. Chem. Chem. Phys.*, 2016, **18**, 32744–32752.

199 Y. Deng, C. Eames, B. Fleutot, R. David, J. N. Chotard, E. Suard, C. Masquelier and M. S. Islam, Enhancing the Lithium Ion Conductivity in Lithium Superionic Conductor (LISICON) Solid Electrolytes through a Mixed Polyanion Effect, *ACS Appl. Mater. Interfaces*, 2017, **9**, 7050–7058.

200 A. Jain, S. P. Ong, G. Hautier, W. Chen, W. D. Richards, S. Dacek, S. Cholia, D. Gunter, D. Skinner, G. Ceder and K. A. Persson, Commentary: The Materials Project: A materials genome approach to accelerating materials innovation, *APL Mater.*, 2013, **1**, 011002.

201 K. Kaup, A. Assoud, J. Liu and L. F. Nazar, Fast Li-Ion Conductivity in Superadamantanoid Lithium Thioborate Halides, *Angew. Chemie - Int. Ed.*, 2021, **60**, 6975–6980.

202 I. Hanghofer, B. Gadermaier, H. Martin and R. Wilkening, Fast Rotational Dynamics in Argyrodite-Type Li_6PS_5X (X: Cl, Br, I) as Seen by ^{31}P Nuclear Magnetic Relaxation On Cation−Anion Coupled Transport in Thiophosphates, *Chem. Mater*, 2019, **31**, 4591–4597.

203 J. S. Kim, G. Yoon, S. Kim, S. Sugata, N. Yashiro, S. Suzuki, M. J. Lee, R. Kim, M. Badding, Z. Song, J. M. Chang and D. Im, Surface engineering of inorganic solid-state electrolytes via interlayers strategy for developing long-cycling quasi-all-solid-state lithium batteries, *Nat. Commun. 2023 141*, 2023, **14**, 1–11.

204 Q. Wang, Y. Zhou, X. Wang, H. Guo, S. Gong, Z. Yao, F. Wu, J. Wang, S. Ganapathy, X. Bai, B. Li, C. Zhao, J. Janek and M. Wagemaker, Designing lithium halide solid electrolytes, *Nat. Commun. 2024 151*, 2024, **15**, 1–10.

205 X. Luo, Y. Li and X. Zhao, Theoretical Design of Defects as a Driving Force for Ion

Transport in Li_3OBr Solid Electrolyte, *Energy Environ. Mater.*, 2023, e12627.

206 A. M. Ganose, A. J. Jackson and D. O. Scanlon, sumo: Command-line tools for plotting and analysis of periodic *ab initio* calculations, *J. Open Source Softw.*, 2018, **3**, 717.

207 M. Chen, L. Liu, Z. Yin, S. F. Liu and Z. Xu, Defect Physics in Na_3OI Antiperovskite Solid Electrolytes, *J. Phys. Chem. C*, 2024, **128**, 9311–9316.

208 L. L. Wong, H. Chen and S. Adams, Design of fast ion conducting cathode materials for grid-scale sodium-ion batteries, *Phys. Chem. Chem. Phys.*, 2017, **19**, 7506–7523.

209 M. Wu, B. Xu, X. Lei, K. Huang and C. Ouyang, Bulk properties and transport mechanisms of a solid state antiperovskite Li-ion conductor Li_3OCl: Insights from first principles calculations, *J. Mater. Chem. A*, 2018, **6**, 1150–1160.

210 F. Hussain, P. Li, Z. Li and J. Yang, Ion Conductivity Enhancement in Anti-Spinel Li_3OBr with Intrinsic Vacancies, *Adv. Theory Simulations*, 2019, **2**, 1800138.

211 T. L. Pham, A. Samad, H. J. Kim and Y. H. Shin, Computational predictions of stable phase for antiperovskite Na_3OCl via tilting of Na_6O octahedra, *J. Appl. Phys.*, 2018, **124**, 164106.

212 M. S. Wu, B. Xu, W. W. Luo, B. Z. Sun and C. Y. Ouyang, Interfacial properties and Li-ion dynamics between Li_3OCl solid electrolyte and Li metal anode for all solid state Li metal batteries from first principles study, *Electrochim. Acta*, 2020, **334**, 135622.

213 O. Reckeweg, B. Blaschkowski and T. Schleid, Li_5OCl_3 and Li_3OCl: Two Remarkably Different Lithium Oxide Chlorides, *Zeitschrift fur Anorg. und Allg. Chemie*, 2012, **638**, 2081–2086.

Appendices

Appendix A

A.1 Lattice Parameters and Input CIF structures

Table A1.1. Comparison of calculated and available experimental lattice parameters (LPs) for Li_xOX_{x-2} (X = Cl or Br; x = 3–6) anti-perovskites.

System	Calculated LPs (Å)	Experimental LPs (Å)	Difference (%)
Li_3OCl	$a = b = c = 3.919$ $\alpha = \beta = \gamma = 90^o$	$a = b = c = 3.907$[213]	0.31
Li_3OBr	$a = b = c = 4.000$ $\alpha = \beta = \gamma = 90^o$	$a = b = c = 4.035$[194]	0.87
Li_4OCl_2	$a = b = 3.902$ $c = 12.631$ $\alpha = \beta = \gamma = 90^o$	Not available	-

Li_4OBr_2	$a = b = 4.045$ $c = 13.762$ $\alpha = \beta = \gamma = 90^o$	$a = b = 3.943$[195] $c = 13.656$[195]	$a = 2.57$ $c = 0.77$
Li_5OCl_3	$a = 7.738$ $b = 5.930$ $c = 11.691$ $\alpha = \beta = \gamma = 90^o$	Not available	-
Li_5OBr_3	$a = 8.287$ $b = 6.373$ $c = 12.540$ $\alpha = \beta = \gamma = 90^o$	Not available	-

Li_6OCl_4	a = 7.203 b = 6.765 c = 7.204 $\alpha = \gamma = 90^o$ $\beta = 95^o$	Not available	-
Li_6OBr_4	a = 7.777 b = 7.305 c = 7.777 $\alpha = \gamma = 90^o$ $\beta = 94^o$	Not available	-

Li_3OCl CIF

data_VESTA_phase_1

_chemical_name_common 'Li3 Cl1 O1'

_cell_length_a 3.908337

_cell_length_b 3.908337

_cell_length_c 3.908337

_cell_angle_alpha 90.000000

_cell_angle_beta 90.000000

_cell_angle_gamma 90.000000

_cell_volume 59.700236

_space_group_name_H-M_alt 'P 1'

_space_group_IT_number 1

loop_

_space_group_symop_operation_xyz

'x, y, z'

loop_

_atom_site_label

_atom_site_occupancy

_atom_site_fract_x

_atom_site_fract_y

_atom_site_fract_z

_atom_site_adp_type

_atom_site_U_iso_or_equiv

_atom_site_type_symbol

Li0 1.0 0.000000 0.500000 0.500000 Uiso ? Li

Li1 1.0 0.500000 0.000000 0.500000 Uiso ? Li

Li2 1.0 0.500000 0.500000 0.000000 Uiso ? Li

Cl3 1.0 0.000000 0.000000 0.000000 Uiso ? Cl

O4 1.0 0.500000 0.500000 0.500000 Uiso ? O

Li_3OBr CIF

data_VESTA_phase_1

_chemical_name_common 'New structure'

_cell_length_a 4.000000

_cell_length_b 4.000000

_cell_length_c 4.000000

```
_cell_angle_alpha                  90.000000
_cell_angle_beta                   90.000000
_cell_angle_gamma                  90.000000
_cell_volume                       64.000000
_space_group_name_H-M_alt          'P 1'
_space_group_IT_number             1

loop_
_space_group_symop_operation_xyz
  'x, y, z'

loop_
  _atom_site_label
  _atom_site_occupancy
  _atom_site_fract_x
  _atom_site_fract_y
  _atom_site_fract_z
  _atom_site_adp_type
  _atom_site_U_iso_or_equiv
  _atom_site_type_symbol
  Br1        1.0     0.000000     0.000000     0.000000    Uiso  ? Br
```

O1	1.0	0.500000	0.500000	0.500000	Uiso	? O
Li1	1.0	0.500000	0.500000	0.000000	Uiso	? Li
Li2	1.0	0.500000	0.000000	0.500000	Uiso	? Li
Li3	1.0	0.000000	0.500000	0.500000	Uiso	? Li

Li_4OCl_2 CIF

data_cif

_audit_creation_method 'generated by GULP'

_symmetry_space_group_name_H-M 'P 1'

_symmetry_Int_Tables_number 1

_symmetry_cell_setting triclinic

_cell_length_a 3.9043

_cell_length_b 3.9043

_cell_length_c 12.5990

_cell_angle_alpha 90.0000

_cell_angle_beta 90.0000

_cell_angle_gamma 90.0000

loop_

_atom_site_label

_atom_site_fract_x

_atom_site_fract_y

_atom_site_fract_z

_atom_site_occupancy

Li	0.00000	0.50000	0.00000	1.0000
Li	0.50000	0.00000	0.00000	1.0000
Li	0.50000	1.00000	0.50000	1.0000
Li	0.00000	0.50000	0.50000	1.0000
Li	1.00000	0.00000	0.15304	1.0000
Li	0.00000	0.00000	0.84696	1.0000
Li	0.50000	0.50000	0.65304	1.0000
Li	0.50000	0.50000	0.34696	1.0000
Cl	0.00000	1.00000	0.34637	1.0000
Cl	0.00000	1.00000	0.65363	1.0000
Cl	0.50000	0.50000	0.84637	1.0000
Cl	0.50000	0.50000	0.15363	1.0000
O	1.00000	0.00000	0.00000	1.0000
O	0.50000	0.50000	0.50000	1.0000

Li_4OBr_2 CIF

data_VESTA_phase_1

_chemical_name_common 'New structure'

_cell_length_a 3.904336

_cell_length_b 3.904336

_cell_length_c 11.599001

_cell_angle_alpha 90.000000

_cell_angle_beta 90.000000

_cell_angle_gamma 90.000000

_cell_volume 176.813308

_space_group_name_H-M_alt 'P 1'

_space_group_IT_number 1

loop_

_space_group_symop_operation_xyz

'x, y, z'

loop_

_atom_site_label

_atom_site_occupancy

_atom_site_fract_x

_atom_site_fract_y

_atom_site_fract_z

_atom_site_adp_type

_atom_site_U_iso_or_equiv

_atom_site_type_symbol

Li1	1.0	0.000000	0.500000	0.000000	Uiso	?	Li
Li2	1.0	0.500000	0.000000	0.000000	Uiso	?	Li
Li3	1.0	0.500000	1.000000	0.500000	Uiso	?	Li
Li4	1.0	0.000000	0.500000	0.500000	Uiso	?	Li
Li5	1.0	1.000000	0.000000	0.153038	Uiso	?	Li
Li6	1.0	0.000000	0.000000	0.846962	Uiso	?	Li
Li7	1.0	0.500000	0.500000	0.653038	Uiso	?	Li
Li8	1.0	0.500000	0.500000	0.346962	Uiso	?	Li
Br1	1.0	0.000000	1.000000	0.346373	Uiso	?	Br
Br2	1.0	0.000000	1.000000	0.653627	Uiso	?	Br
Br3	1.0	0.500000	0.500000	0.846373	Uiso	?	Br
Br4	1.0	0.500000	0.500000	0.153627	Uiso	?	Br
O1	1.0	1.000000	0.000000	0.000000	Uiso	?	O
O2	1.0	0.500000	0.500000	0.500000	Uiso	?	O
Br5	1.0	0.000000	1.000000	0.346550	Uiso	?	Br

Br6	1.0	0.000000	0.000000	0.653450	Uiso	? Br
Br7	1.0	0.500000	0.500000	0.846550	Uiso	? Br
Br8	1.0	0.500000	0.500000	0.153450	Uiso	? Br
O3	1.0	1.000000	0.000000	0.000000	Uiso	? O
O4	1.0	0.500000	0.500000	0.500000	Uiso	? O

Li_5OCl_3 CIF

data_cif

_audit_creation_method 'generated by GULP'

_symmetry_space_group_name_H-M 'P 1'

_symmetry_Int_Tables_number 1

_symmetry_cell_setting triclinic

_cell_length_a 7.7384

_cell_length_b 5.9300

_cell_length_c 11.6909

_cell_angle_alpha 90.0013

_cell_angle_beta 89.9993

_cell_angle_gamma 90.0011

loop_

_atom_site_label

_atom_site_fract_x

_atom_site_fract_y

_atom_site_fract_z

_atom_site_occupancy

Li	0.63333	0.52653	0.62577	1.0000
Li	0.36204	0.57358	0.36697	1.0000
Li	0.86203	0.02651	0.36699	1.0000
Li	0.13333	0.07357	0.62577	1.0000
Li	0.36204	0.57359	0.12577	1.0000
Li	0.63332	0.52657	0.86696	1.0000
Li	0.13332	0.07358	0.86697	1.0000
Li	0.86204	0.02654	0.12578	1.0000
Li	0.63334	0.07356	0.86697	1.0000
Li	0.36192	0.02659	0.12579	1.0000
Li	0.86191	0.57354	0.12578	1.0000
Li	0.13334	0.52658	0.86696	1.0000
Li	0.36191	0.02659	0.36696	1.0000

Li	0.63335	0.07352	0.62579	1.0000
Li	0.13335	0.52658	0.62578	1.0000
Li	0.86191	0.57351	0.36696	1.0000
Li	0.37856	0.30004	0.74637	1.0000
Li	0.61676	0.80020	0.24638	1.0000
Li	0.11676	0.79991	0.24638	1.0000
Li	0.87855	0.30008	0.74637	1.0000
Cl	0.33582	0.80008	0.74638	1.0000
Cl	0.65951	0.30003	0.24637	1.0000
Cl	0.15951	0.30008	0.24637	1.0000
Cl	0.83582	0.80006	0.74638	1.0000
Cl	0.37884	0.30006	0.97079	1.0000
Cl	0.61647	0.80005	0.02196	1.0000
Cl	0.11647	0.80008	0.02196	1.0000
Cl	0.87884	0.30007	0.97079	1.0000
Cl	0.61647	0.80005	0.47080	1.0000
Cl	0.37884	0.30006	0.52195	1.0000
Cl	0.87885	0.30006	0.52195	1.0000
Cl	0.11647	0.80007	0.47079	1.0000
O	0.62569	0.30005	0.74637	1.0000
O	0.36962	0.80008	0.24638	1.0000

O	0.86962	0.80004	0.24638	1.0000
O	0.12569	0.30007	0.74637	1.0000

Li_5OBr_3 CIF

data_VESTA_phase_1

_chemical_name_common 'New structure'

_cell_length_a 8.500000

_cell_length_b 6.300000

_cell_length_c 13.000000

_cell_angle_alpha 90.000000

_cell_angle_beta 90.000000

_cell_angle_gamma 90.000000

_cell_volume 696.150021

_space_group_name_H-M_alt 'P 1'

_space_group_IT_number 1

loop_

_space_group_symop_operation_xyz

'x, y, z'

loop_

_atom_site_label

_atom_site_occupancy

_atom_site_fract_x

_atom_site_fract_y

_atom_site_fract_z

_atom_site_adp_type

_atom_site_U_iso_or_equiv

_atom_site_type_symbol

Li1 1.0 0.633330 0.526530 0.625770 Uiso ? Li

Li2 1.0 0.863210 0.609350 0.348160 Uiso ? Li

Li3 1.0 0.363210 0.026560 0.348160 Uiso ? Li

Li4 1.0 0.133330 0.109360 0.625760 Uiso ? Li

Li5 1.0 0.863210 0.609350 0.125770 Uiso ? Li

Li6 1.0 0.633330 0.526550 0.848160 Uiso ? Li

Li7 1.0 0.133330 0.109360 0.848160 Uiso ? Li

Li8 1.0 0.363210 0.026560 0.125760 Uiso ? Li

Li9 1.0 0.633360 0.109320 0.848160 Uiso ? Li

Li10 1.0 0.863210 0.026560 0.125770 Uiso ? Li

Li11 1.0 0.363210 0.609340 0.125760 Uiso ? Li

Li12 1.0 0.133360 0.526580 0.848150 Uiso ? Li

Li13	1.0	0.863210	0.026560	0.348160	Uiso	? Li
Li14	1.0	0.633340	0.109310	0.625770	Uiso	? Li
Li15	1.0	0.133360	0.526580	0.625770	Uiso	? Li
Li16	1.0	0.363210	0.609340	0.348160	Uiso	? Li
Li17	1.0	0.383820	0.317900	0.736960	Uiso	? Li
Li18	1.0	0.112740	0.817950	0.236960	Uiso	? Li
Li19	1.0	0.612720	0.817950	0.236960	Uiso	? Li
Li20	1.0	0.883810	0.318000	0.736960	Uiso	? Li
Br1	1.0	0.291370	0.817980	0.736960	Uiso	? Br
Br2	1.0	0.205170	0.317950	0.236960	Uiso	? Br
Br3	1.0	0.705180	0.317950	0.236960	Uiso	? Br
Br4	1.0	0.791370	0.817920	0.736960	Uiso	? Br
Br5	1.0	0.379280	0.317960	0.942690	Uiso	? Br
Br6	1.0	0.117280	0.817950	0.031230	Uiso	? Br
Br7	1.0	0.617280	0.817950	0.031230	Uiso	? Br
Br8	1.0	0.879280	0.317950	0.942690	Uiso	? Br
Br9	1.0	0.117280	0.817950	0.442690	Uiso	? Br
Br10	1.0	0.379280	0.317940	0.531230	Uiso	? Br
Br11	1.0	0.879280	0.317950	0.531230	Uiso	? Br
Br12	1.0	0.617280	0.817950	0.442690	Uiso	? Br
O1	1.0	0.620340	0.317930	0.736960	Uiso	? O

O2	1.0	0.876210	0.817950	0.236960	Uiso	?	O
O3	1.0	0.376200	0.817950	0.236960	Uiso	?	O
O4	1.0	0.120360	0.317970	0.736960	Uiso	?	O
Br13	1.0	0.291370	0.817980	0.736960	Uiso	?	Br
Br14	1.0	0.205170	0.317950	0.236960	Uiso	?	Br
Br15	1.0	0.705180	0.317950	0.236960	Uiso	?	Br
Br16	1.0	0.791370	0.817920	0.736960	Uiso	?	Br
Br17	1.0	0.379280	0.317960	0.942690	Uiso	?	Br
Br18	1.0	0.117280	0.817950	0.031230	Uiso	?	Br
Br19	1.0	0.617280	0.817950	0.031230	Uiso	?	Br
Br20	1.0	0.879280	0.317950	0.942690	Uiso	?	Br
Br21	1.0	0.117280	0.817950	0.442690	Uiso	?	Br
Br22	1.0	0.379280	0.317940	0.531230	Uiso	?	Br
Br23	1.0	0.879280	0.317950	0.531230	Uiso	?	Br
Br24	1.0	0.617280	0.817950	0.442690	Uiso	?	Br
O5	1.0	0.620340	0.317930	0.736960	Uiso	?	O
O6	1.0	0.876210	0.817950	0.236960	Uiso	?	O
O7	1.0	0.376200	0.817950	0.236960	Uiso	?	O
O8	1.0	0.120360	0.317970	0.736960	Uiso	?	O

Li_6OCl_4 CIF

data_cif

_audit_creation_method 'generated by GULP'

_symmetry_space_group_name_H-M 'P 1'

_symmetry_Int_Tables_number 1

_symmetry_cell_setting triclinic

_cell_length_a 7.1969

_cell_length_b 6.7647

_cell_length_c 7.2117

_cell_angle_alpha 90.0135

_cell_angle_beta 95.4091

_cell_angle_gamma 89.9876

loop_

_atom_site_label

_atom_site_fract_x

_atom_site_fract_y

_atom_site_fract_z

_atom_site_occupancy

Cl	0.83052	0.24256	0.33877	1.0000
Cl	0.07518	0.74173	0.58339	1.0000
Cl	0.65751	0.74257	0.16663	1.0000
Cl	0.41334	0.24175	0.92257	1.0000
Cl	0.84469	0.39024	0.80678	1.0000
Cl	0.18998	0.59319	0.15281	1.0000
Cl	0.64402	0.89034	0.69877	1.0000
Cl	0.29815	0.09325	0.35333	1.0000
Li	0.99042	0.91930	0.26672	1.0000
Li	0.97148	0.04064	0.73786	1.0000
Li	0.49788	0.41944	0.23898	1.0000
Li	0.51727	0.54052	0.76812	1.0000
Li	0.26018	0.94145	0.02721	1.0000
Li	0.73027	0.06574	0.00569	1.0000
Li	0.22842	0.44137	0.47892	1.0000
Li	0.75805	0.56585	0.50000	1.0000
Li	0.05944	0.26296	0.06553	1.0000
Li	0.93037	0.72051	0.93939	1.0000
Li	0.42871	0.76297	0.44061	1.0000
Li	0.55837	0.22051	0.56611	1.0000

O	0.00104	0.99172	0.99635	1.0000
O	0.48748	0.49178	0.50954	1.0000

Li_6OBr_4 CIF

data_VESTA_phase_1

_chemical_name_common 'New structure'

_cell_length_a 7.776548

_cell_length_b 7.305370

_cell_length_c 7.776600

_cell_angle_alpha 90.000000

_cell_angle_beta 94.241402

_cell_angle_gamma 90.000000

_cell_volume 440.583043

_space_group_name_H-M_alt 'P 1'

_space_group_IT_number 1

loop_

_space_group_symop_operation_xyz

'x, y, z'

loop_

_atom_site_label

_atom_site_occupancy

_atom_site_fract_x

_atom_site_fract_y

_atom_site_fract_z

_atom_site_adp_type

_atom_site_U_iso_or_equiv

_atom_site_type_symbol

Br1	1.0	0.830520	0.242564	0.338774	Uiso	? Br
Br2	1.0	0.181879	0.742550	0.690134	Uiso	? Br
Br3	1.0	0.681879	0.742564	0.190134	Uiso	? Br
Br4	1.0	0.330520	0.242550	0.838774	Uiso	? Br
Br5	1.0	0.822528	0.375991	0.830790	Uiso	? Br
Br6	1.0	0.189874	0.609122	0.198121	Uiso	? Br
Br7	1.0	0.689874	0.875992	0.698120	Uiso	? Br
Br8	1.0	0.322528	0.109122	0.330790	Uiso	? Br
Li1	1.0	0.004155	0.931049	0.254962	Uiso	? Li
Li2	1.0	0.008244	0.054063	0.773953	Uiso	? Li
Li3	1.0	0.508244	0.431051	0.273953	Uiso	? Li

Li4	1.0	0.504155	0.554065	0.754962	Uiso	?	Li
Li5	1.0	0.246697	0.931002	0.012467	Uiso	?	Li
Li6	1.0	0.765703	0.054108	0.016453	Uiso	?	Li
Li7	1.0	0.265703	0.431006	0.516453	Uiso	?	Li
Li8	1.0	0.746697	0.554112	0.516453	Uiso	?	Li
Li9	1.0	0.071128	0.258908	0.079351	Uiso	?	Li
Li10	1.0	0.941271	0.726206	0.949569	Uiso	?	Li
Li11	1.0	0.441271	0.758908	0.449569	Uiso	?	Li
Li12	1.0	0.571128	0.226206	0.579351	Uiso	?	Li
O1	1.0	0.006200	0.992555	0.014458	Uiso	?	O
O2	1.0	0.506200	0.492559	0.514458	Uiso	?	O
Br9	1.0	0.828744	0.242560	0.336999	Uiso	?	Br
Br10	1.0	0.183656	0.742552	0.691908	Uiso	?	Br
Br11	1.0	0.683656	0.742561	0.191908	Uiso	?	Br
Br12	1.0	0.328744	0.242554	0.836999	Uiso	?	Br
Br13	1.0	0.821463	0.373942	0.829728	Uiso	?	Br
Br14	1.0	0.190938	0.611171	0.199182	Uiso	?	Br
Br15	1.0	0.690938	0.873943	0.699183	Uiso	?	Br
Br16	1.0	0.321463	0.111172	0.329728	Uiso	?	Br
O3	1.0	0.006200	0.992555	0.014458	Uiso	?	O
O4	1.0	0.506200	0.492559	0.514458	Uiso	?	O

A.2 Example LAMMPS file

```
############################################################
#------------Variables and cell-------------------------#
############################################################

    clear
    units          metal       #eV,atomic charge,angstroms,ps,kelvin,bars,g/mol
    dimension 3
    boundary p p p
    atom_style full
    #processors * * * grid numa
    read_data Li4OCl2.lammps
    group lithium type 1
    #replicate 2 2 2
    variable T1 equal 500
    variable Timer equal step*dt

############################################################
#---------- Pair styles and electrostatics--------------#
############################################################
```

```
pair_style buck/coul/long 12.0
pair_coeff * *  0.0 1.0 0.0
pair_coeff 1 1  360.5269 0.1609 0
pair_coeff 1 2  292.3 0.3472 0
pair_coeff 1 3  421.0366 0.33364 0
pair_coeff 2 2  22764.3 0.149 13.185
pair_coeff 2 3  8287 0.259 62.2
pair_coeff 3 3  1227.2 0.3214 14.53

#pair_style buck/coul/long 10.0
#pair_coeff * *  0.0 1.0 0.0
#pair_coeff 1 4  2088.79 0.346 23.25
#pair_coeff 2 4  1453.8 0.35 0
#pair_coeff 3 4  632.1018 0.2906 0
#pair_coeff 4 4  22764.3 0.149 27.869

kspace_style pppm 1e-05

############################################################
# ---------- Run Minimisation ----------#
############################################################
```

```
reset_timestep 0
timestep 0.5
thermo 10
thermo_style custom step enthalpy fmax lx ly lz vol press
min_style cg
minimize 1e-25 1e-25 5000 10000
#########################################################
# ---------- Relax Cell ----------#
#########################################################

reset_timestep 0
timestep 0.5
fix 1 all box/relax aniso 1.0 vmax 0.003
thermo 1
thermo_style custom step enthalpy fmax lx ly lz vol press
min_style cg
minimize 1e-25 1e-25 5000 10000
unfix 1

#########################################################
```

```
# ------------ Run NPT T1-----------------------------#
############################################################

    reset_timestep 0
    timestep 0.002
    velocity all create ${T1} 4928459 rot yes dist gaussian
    fix             2 all npt temp ${T1} ${T1} 0.01 aniso 1.0 1.0 0.1
    thermo_style custom step v_Timer cpu temp etotal fmax lx ly lz vol press
    thermo 1000
    run 2000
    unfix 2

    reset_timestep 0
    timestep 0.002
    compute         mymsd lithium msd com yes
    variable        msdx equal "c_mymsd[1]"
    variable        msdy equal "c_mymsd[2]"
    variable        msdz equal "c_mymsd[3]"
    variable        msdtot equal "c_mymsd[4]"
    fix             msdT1 lithium ave/time 1 1 10000 v_msdx v_msdy v_msdz v_msdtot file
    msd${T1}
```

```
fix             3 all nvt temp ${T1} ${T1} 0.01
thermo_style custom step v_Timer cpu temp etotal fmax lx ly lz vol press
thermo 5000
#dump dynamics all xyz 100 dynamics.xyz
#dump 4 all atom 100 traj.dat
run             5000000
unfix 3
unfix msdT1
```

A.3 Supporting Tables

Table A3.1. Calculated formation energies for Schottky, Frenkel, and antisite defects in Li_xOX_{x-2} (X = Cl or Br; x = 3–6) anti-perovskites.

	Formation energy (eV) per defect type						
System	O Frenkel	Full Schottky	Li_2O partial Schottky	Halide Frenkel	Antisite	Li Frenkel	Alkali-halide partial Schottky
Li_3OCl	7.08	5.93	4.57	4.41	3.69	2.72	1.96
Li_4OCl_2	5.26	6.57	4.07	2.81	2.96	1.89	1.56
Li_5OCl_3	4.63	6.25	3.26	1.83	1.83	1.27	1.16
Li_6OCl_4	1.70	3.64	1.85	0.46	1.28	0.56	0.63
Li_3OBr	9.21	7.40	5.69	9.57	5.69	3.59	2.64
Li_4OBr_2	6.27	7.90	4.90	6.08	4.17	2.29	2.07
Li_5OBr_3	3.65	6.79	3.55	2.41	2.52	1.60	1.40
Li_6OBr_4	2.94	6.23	3.07	1.79	2.43	0.89	0.81

A.4 Supporting Plots

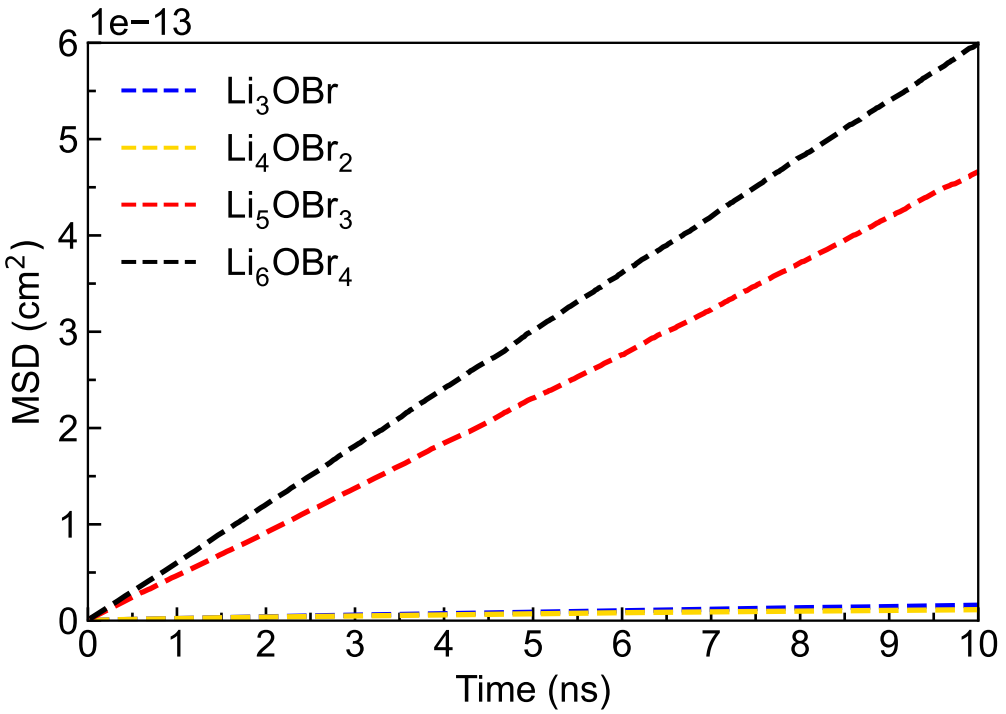

Figure A4.1 MSD plots for Li_xOBr_{x-2} (x = 3–6) anti-perovskites at 700 K with an alkali-halide partial Schottky defect concentration of ~2%.

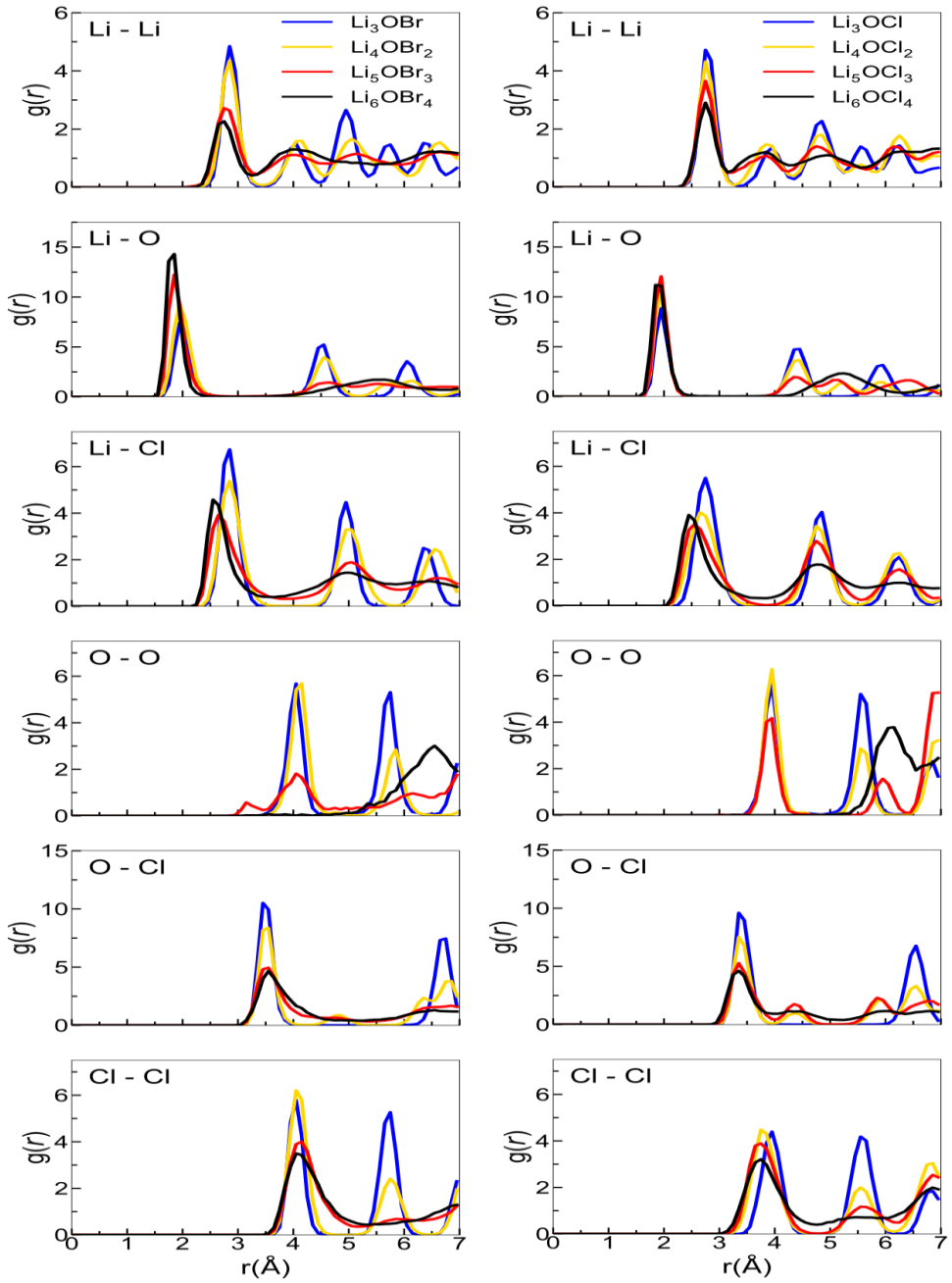

Figure A4.2. Radial distribution functions for Li_xOX_{x-2} (X = Cl or Br; x = 3–6) anti-perovskites at 300 K.

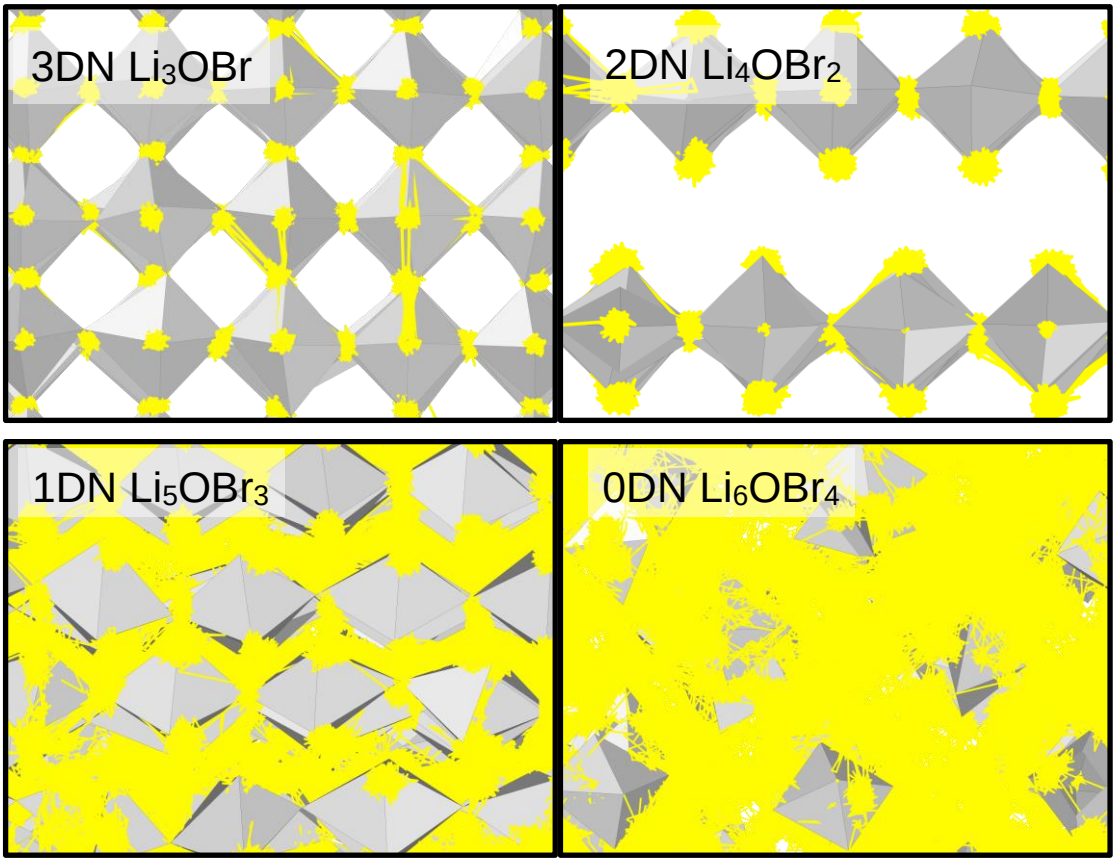

Figure A4.3. Diffusion density plots of Li ions (yellow) overlaid on OLi_6 (grey) octahedra in Li_xOBr_{x-2} (x = 3–6) anti-perovskites at 300 K. Br ions have been omitted for clarity.

Appendix B

B.1 Supporting Tables

Table B1.1. Specific MP *k*-point mesh used for optimising (100) MX, (100) MO, (110) M, (110) MOX, (111) MX and (111) O (M = Na, X = Cl or Br) surface types derived from Na_3OCl and Na_3OBr and (100) MX, (100) MO, (110) M, (110) MOX, (111) MX and (111) O (M = Li, X = Cl) surface types derived from Li_3OCl.

Surface	k-point *mesh*
(100) MX	4 x 4 x 1
(100) MO	4 x 4 x 1
(110) M	3 x 4 x 1
(110) MOX	3 x 4 x 1
(111) MX	3 x 3 x 1
(111) O	3 x 3 x 1

Table B1.2. Specific MP *k*-point mesh used for optimising (100) MX, (100) MO, (110) M, (110) MOX, (111) MX and (111) O (M = Li; X = Br) surface types derived from Li_3OBr.

Surface	k-point *mesh*
(100) MX	5 x 5 x 1
(100) MO	5 x 5 x 1
(110) M	4 x 5 x 1
(110) MOX	4 x 5 x 1
(111) MX	4 x 4 x 1
(111) O	4x 4 x 1

B.2 Supporting Figures

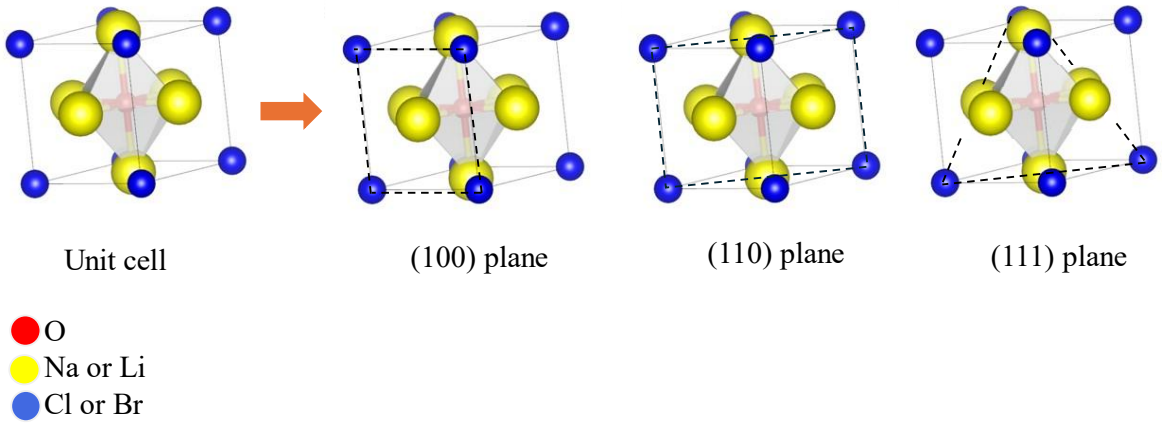

Figure B2.1. Crystal structure of Li_3OCl showing the three Miller indices cuts used.

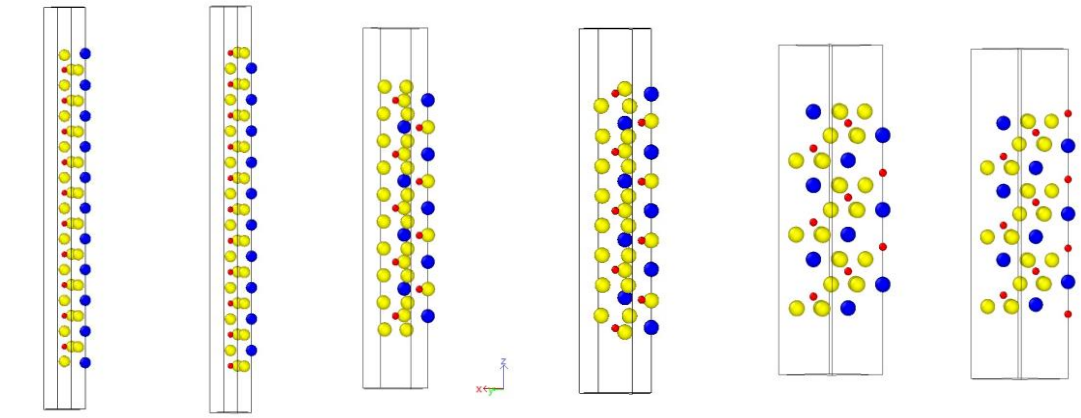

Figure B2.2. Slab models used for (100) LiBr, (100) LiO, (110) Li, (110) LiOBr, (111) LiBr and (111) O surface types.

B.3 Supporting Plots

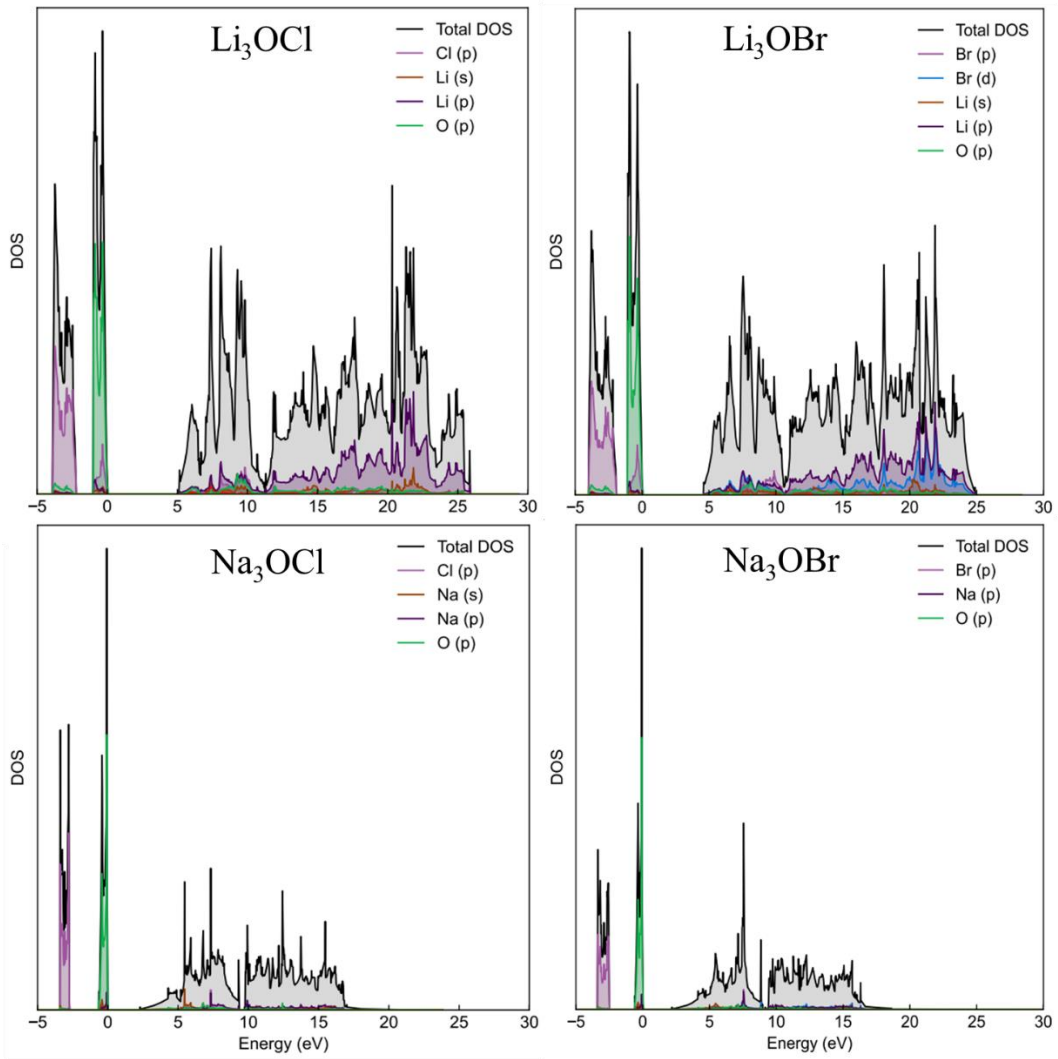

Figure B3.1. DOS plots calculated using PBE for all analysed pristine M_3OX (M = Li or Na; X = Cl or Br) bulk systems.

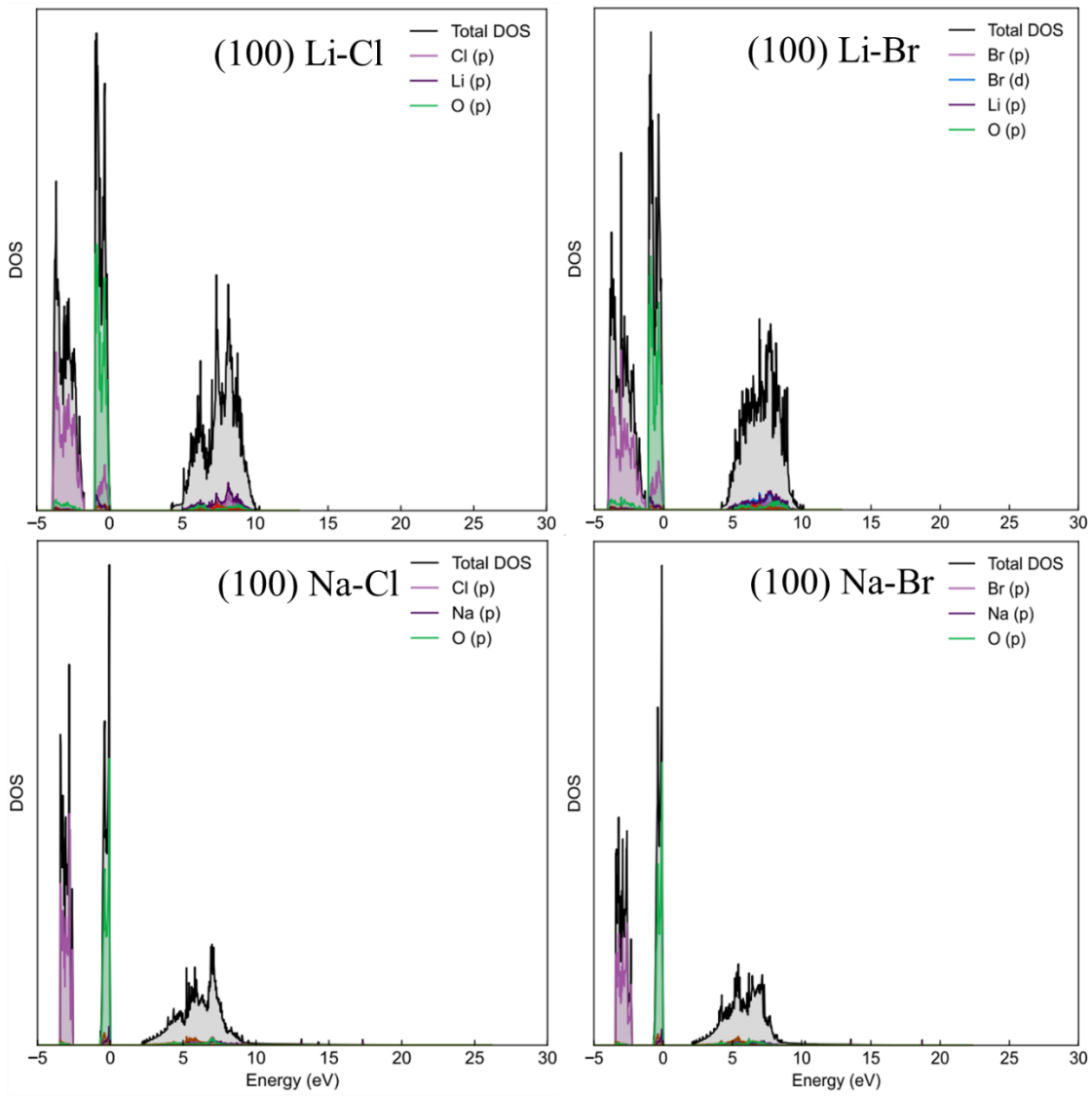

Figure B3.2. DOS plots calculated using PBE for (100) MX, (100) MO, (110) M, (110) MOX, (111) MX and (111) O (M = Li or Na; X = Cl or Br) surfaces.